

**EXPERIMENTAL AND NUMERICAL STUDIES
OF WHIRLING FIRES**

by

James Anthony Marsden
BEng, CEng, FIFireE, MEI

A Thesis

Submitted to the Faculty of Design and Technology
in partial fulfilment of the requirements
for the Degree of Doctor of Philosophy

UNIVERSITY OF CENTRAL LANCASHIRE

Preston England

2005

DECLARATION

The writing of this thesis and the research discussed was carried out solely by James Marsden under the supervision of Dr A.Yu. Snegirev (Director of Studies), Prof. G.M. Makhviladze and Dr J. Francis (Supervisors). Where other sources are quoted full references are given.

ABSTRACT

Motivation of this study stems from the need to understand the physical mechanisms of whirling fires that occur in an open space and within enclosures. Buoyant whirling flames may be potentially more destructive than ordinary fires due to greater burning rate, higher concentration of heat release in a small region of the plume core, increased radiative output and unexpected smoke movement. The effects of rotation upon the structure and behaviour of buoyant flames have not yet been thoroughly studied and understood. Investigation of this phenomenon is therefore required to allow techniques to be developed that will counter the threat of such outbreaks. Also, the mechanisms controlling the development and stability of whirling flames are of fundamental interest for refined modelling of coherent and self-organised flame behaviour. This work, is an experimental, theoretical and numerical study of whirling fires. Experimental results, a modified CFD model and simulations of whirling flames are presented within this Thesis.

The work aims to overcome the limitations of the previous research of whirling fires which is insufficient from both an experimental and theoretical point of view. *Firstly*, experimental studies of intermediate (room-size) scale whirling fires have not yet been comprehensively reported, despite a great deal of attention devoted to both large scale mass fires and smaller laboratory flames. Experimental studies undertaken using a facility at the Greater Manchester Fire and Rescue Service Training Centre fill this gap, thus demonstrating that whirling flames may develop within a compartment. The periodic precession, formation and destruction of the whirling flame and the increase of the time-averaged burning rate (compared to non-whirling flames in the open space) have been observed. Three fuels with significantly different burning rates (diesel, heptane and ethanol) were investigated

in this work. *Secondly*, previously published results of theoretical analysis of rotating flames were oversimplified and based on strict limitations of the integral model or the inviscid flow assumption. Also there have only been few attempts to undertake CFD modelling of whirling flames. In published studies, radiative heat transfer was not modelled and the burning rate was not coupled with the incident heat flux at the fuel surface. To overcome these limitations, the CFD fire model *Fire3D*, developed in the Centre for Research in Fire and Explosion Studies, has been adapted to allow numerical simulations of rotating buoyant turbulent diffusion flames. The turbulence model was modified to take into account stabilisation of turbulent fluctuations due to the centrifugal acceleration within the rotating flow. Theoretical analysis of the vorticity equation revealed the physical mechanisms responsible for vorticity concentration and amplification in the rising plume affected by externally imposed circulation. This explains the significant flame elongation (when compared to non-rotating cases) observed in the experiments. Computational results have also been compared to video-recordings of the experimental flames produced; flame elongation was replicated and similar stages of oscillating flame evolution, including formation and destruction of the vortex core, have been identified.

Implications of the phenomena studied in relation to fire engineering are also provided. This study contributes to a performance based framework for an engineering approach, which is reliant upon detailed quantitative analysis and modelling. Such an approach is encouraged by modern fire safety legislation including the guides to fire safety engineering BS9999-2¹ and BS7974².

¹ British Standard 9999-2 Draft Code of Practice for fire safety in the design, construction and use of buildings. BSI, 2004. UK.

² British Standard BS7974 Application of fire safety engineering principles to the design of buildings. BSI, 2001–2003. UK.

PUBLICATIONS AND PRESENTATIONS

Journal papers

The following relevant works have been presented and published during this period of registration.

1. Snegirev A.Yu., Marsden J.A., Francis J., Makhviladze G.M. (2004) Numerical studies and experimental observations of whirling flames. *International Journal of Heat and Mass Transfer*, 17, 12–13, 2523–2359.
2. Snegirev A.Yu., Marsden J.A., Makhviladze G.M. (2004) Transient Behaviour and Stability of Whirling Flames in Enclosure. *Proceedings of the Combustion Institute*, 30 (to appear).

Conference papers and presentations

1. Marsden J.A. (2000) Rotating Fire Plumes. *Research Seminar No 60 of the Centre for Research in Fire and Explosion Studies*, 15 June 2000, UCLan, Preston, UK.
2. Marsden J.A., Francis J. (2000) The Creation of Swirling Fire Plumes in Full Scale Compartment Tests. Initial Results, *Research Event 2000 – RE2K*, 6-7 December 2000, The Fire Service College, Moreton-in-Marsh, UK.
3. Marsden J.A., Snegirev A. (2001) Fire Whirls within Compartments. *Research Event 2001 – RE01*, 21-22 November 2001, The Fire Service College, Moreton-in-Marsh, UK.
4. Marsden J.A. (2002) Experimental and Numerical Studies of Whirling Fires in Enclosure. *Research Seminar No 70 of the Centre for Research in Fire and Explosion Studies*, 19 April 2002, UCLan, UK.
5. Marsden J.A. (2002) Experimental and Numerical Studies of Whirling Fires in Enclosure. *2002 Graduate Lecture of Institution of Fire Engineers*, 2 May 2002 Manchester Metropolitan University, UK.

6. Snegirev A.Yu., Marsden J.A., Francis J., Makhviladze G.M. (2003) Numerical studies and experimental observations of whirling flames. *4th International Seminar on Fire and Explosion Hazards*, 8-12 September 2003, Ulster, UK, pp. 675-690.
7. Snegirev A.Yu., Marsden J.A., Makhviladze G.M. (2003) Whirling Flames. *Meeting of Consortium on Computational Combustion for Engineering Applications COCCFEA*, 19 September 2003, UMIST, Manchester, UK.
8. Marsden J.A. (2003) Experimental and Numerical Studies of Whirling Flames. *University of Central Lancashire Graduate School*, 3 December 2003, UCLan, Preston, UK.
9. Marsden J.A. (2004) Whirling Fires within Enclosures. *Institution of Fire Engineers International Conference*, 3-6 October 2004, Kuala Lumpur, Malaysia.

ACKNOWLEDGEMENTS

There are many people who have contributed to my development in order for me to write this Thesis, to whom I am deeply grateful; however a few special words are in order.

First of all I would like to extend my thanks to the lecturers of the Department of Built Environment at the University of Central Lancashire, Preston, who have guided me in the field of fire engineering and given me the motivation to pursue a doctorate.

The assistance of my employer, Greater Manchester Fire and Rescue Service is also acknowledged in respect to funding and use of the facilities at the Brigade Training Centre. Special thanks are extended to my County Fire Officer Barry Dixon for his support and insight in allowing the completion of this work. Thanks are also extended to Andrew Brookes and Stephen Johnson for their support in the experimental work.

I would also like to thank my supervisors for donating their valuable time in giving their expertise and assistance with this research; and in particular I would acknowledge the support of Prof Georgy Makhviladze, Dr Jonathan Francis and Principal Technician Paul Metcalfe.

The role of my principal supervisor Dr Alexander Snegirev goes without saying; his confidence and encouragement have helped me at all stages of this research and his advice and friendship have helped me to develop. It should be said that his contribution to this work is more than these few words can express.

Finally a few words of thanks are extended to my partner Mary, whose love and support have been a constant motivation during this period; also to my family including my late father James Marsden whose life was tragically cut short.

TABLE OF CONTENTS

Declaration	i
Abstract	ii
Publications and presentations	iv
Journal papers.....	iv
Conference papers and presentations.....	iv
Acknowledgements	vi
Table of contents.....	vii
List of figures	x
List of tables.....	xiv
Nomenclature.....	xv

Chapter 1. Introduction	1
1.1. Background of the project	1
1.2. Outline of the Thesis Chapters	7
Chapter 2. Literature review	9
2.1. Introduction	9
2.2. Liquid fuel pool fires in still air	13
2.3. The effects of cross-wind	17
2.4. The effect of external circulation	19
2.4.1. Large scale fire whirls	19
2.4.2. Small scale rotating flames	20
2.4.2.1. Enforced (jet) swirling flows	20
2.4.2.2. Buoyant whirling flows	23
2.4.3. Medium scale fire whirls	25
2.4.4. Theoretical studies and modelling of fire whirls	25
2.5. Conclusions	29

Chapter 3. Experimental studies of whirling flames	30
3.1. Introduction	30
3.2. The experimental equipment	31
3.2.1. Description of the enclosure	31
3.2.2. Fuel system	32
3.2.3. Description of the fuels	34
3.2.4. Temperature measurement	36
3.2.5. Heat flux measurement	36
3.2.6. Data acquisition	38
3.2.7. Visualisation techniques	38
3.2.8. Experimental arrangements for open flames	38
3.3. Experimental observations of flames in the open space	39
3.4. Experimental observations of whirling fires in the enclosure	42
3.4.1. Flame formation and the behaviour of smoke layer	42
3.4.2. Periodicity of flame rotation	43
3.4.3. Fuel mass burning rates and flame length	45
3.4.4. Temperature and heat flux measurements	48
3.5. Conclusions	51
Chapter 4. Basic theoretical concepts of rotating flows	53
4.1. Introduction	53
4.2. Characteristics of rotating flows	53
4.3. Classification of simple rotating flows	54
4.4. The vorticity equation & sources of vorticity	57
4.5. Vorticity concentration in axisymmetric flow	60
4.6. Dimensionless criteria governing buoyant rotating flows	63
4.7. Conclusions	66
Chapter 5. Mathematical model and CFD code	68
5.1. Introduction	68
5.2. Governing equations	68
5.3. Turbulence modelling & the effect of flow rotation	70
5.4. Modelling of combustion and soot formation	75
5.5. Modelling of thermal radiation	79

Table of contents

5.5.1. Radiative properties of combustion products	81
5.5.2. Turbulence-radiation interaction	82
5.5.3. Statistical modelling of thermal radiation transfer	83
5.6. Boundary and initial conditions	87
5.7. Numerical implementation	91
5.8. Conclusions	92
Chapter 6. Numerical simulations of whirling flames	94
6.1. Simulations of open whirling flames	94
6.2. Simulations of whirling flames in enclosure	104
6.2.1. Simulations with constant prescribed burning rate	104
6.2.2. Simulations with burning rate coupled with incident heat flux	109
6.2.3. The effect of doorway location	111
6.3. Validation of the model by experimental results	112
6.4. Conclusions	114
Chapter 7. Conclusions and future work	
7.1. Results and conclusions	116
7.2. Future work	121
References	123

LIST OF FIGURES

1.1	Examples of a whirling fire: a) The longer and possibly rotating flame exhausting through the roof vent; b) Whirling buoyant flame in enclosure (the Training Centre, Greater Manchester County Fire and Rescue Service).	2
2.1	Flame types covered in the literature review.	12
2.2	Entry swirl generator: swirl induced by the use of swirl vanes [Kurose et al, 2004].	21
2.3	The structure of jet flows with a different degree of swirl [Gupta et al 1984]: a) $S < 0.6$; b) $S > 0.6$.	22
2.4	The effect of the imposed circulation on flame length: a) free-standing non-disturbed flame; b) whirling flame inside rotating screen cylinder [Emmons and Ying, 1966].	23
2.5	Enclosure geometry for a small scale whirling flame [Satoh and Yang, 1996].	24
3.1	The experimental enclosure: a) front view; b) top view.	31
3.2	Schematic and dimensions of the enclosure.	32
3.3	Fuel system.	33
3.4	Insulated fuel pan.	34

List of figures

3.5	Heat flux sensors (HFS-3, Omega Electronics) installed within the enclosure.	37
3.6	Heat flux sensor positions (HF1, HF2) within the enclosure.	37
3.7	Experimental apparatus for flame in the open space.	38
3.8	Non-rotating flames in the open space, weak effect of cross wind. Fuel: a) ethanol; b) diesel; c) heptane.	39
3.9	Non-rotating flames in the open space, strong effect of cross wind. Fuel: a) ethanol; b) diesel; c) heptane.	40
3.10	Formation of the smoke layer within the enclosure: a) smoke layer in the absence of rotation; b) the absence of the smoke layer during flame rotation.	42
3.11	Experimentally observed temporal evolution of whirling flame (fuel is diesel). Conventional time is set to zero for the first frame. Fully developed whirling flames occur at time moments of 4, 14, 24 and 34 s.	44
3.12	Whirling flames within the enclosure and the estimated flame lengths. Fuel: a) ethanol; b) diesel; c) heptane.	48
3.13	Temperature evolution in time for an ethanol flame (thermocouple at the elevation of 0.57 m above the floor level: a) free-standing flame in the open space; b) whirling flame in the enclosure.	49
3.14	Temperature evolution in time for a heptane flame (thermocouple at the elevation of 0.57 m above the floor level: a) free-standing flame in the open space; b) whirling flame in the enclosure.	49
3.15	Dependence of radiative heat flux on time recorded by heat flux sensor HF1: a) ethanol flame; b) heptane flame.	50

4.1	Radial profiles of angular velocity; $v_{\theta}(r)$: a) forced (solid body) vortex, b) free (potential) vortex; c) combined (Rankine) vortex.	55
4.2	Fig. 4.2. Streamlines of the flow (4.16), (4.19): a) $\omega_{z\max} = 0$; b) $\omega_{z\max} > 0$.	61
6.1	Steady state mean temperature fields and mean-flow streamlines in a 516 kW flame: a) $\Gamma_0 = 0 \text{ m}^2/\text{s}$; b) $\Gamma_0 = 1.45 \text{ m}^2/\text{s}$; c) $\Gamma_0 = 4.35 \text{ m}^2/\text{s}$.	96
6.2	The effect of turbulence modelling on the predicted flame centreline temperature.	97
6.3	Radial profiles of angular velocity.	98
6.4	Axial profiles of mean temperature and velocity.	100
6.5	Radial profiles of mean temperature and velocity.	101
6.6	Swirl number of rotating flows versus external circulation.	102
6.7	Radiative heat fluxes at a distance of 1.2 m from the flame axis: a) $\dot{Q} = 258 \text{ kW}$; b) $\dot{Q} = 516 \text{ kW}$.	103
6.8	The predicted straight rotating flame exhausting through the ceiling vent: a) mean temperature and velocity fields; b) mean-flow streamlines and 773 K temperature surface (approximates visual flame).	104
6.9	Comparison of observed and predicted flow. From left to right: frames taken from video recordings; surface $T = 773 \text{ K}$ (approximates visual flame zone); surface $\omega_z = 15 \text{ s}^{-1}$ (location of rotating core). Stages of flame development: a) Flame is deflected towards the rear wall, no regular rotation occurs; b)	

- Flame is deflected towards the doorway, whirling zone starts to form; c) Flame lengthens and straightens, vortex core develops. 106
- 6.9 Cont'd:d) Flame is straight, it exhausts through the ceiling vent, stretched vortex core erect; e) Upper part of flame is displaced by rotating incoming airflow, the vortex core travels towards the rear wall; f) Similar to a). where streamlines run out from the points at doorway cross-section, at elevations 0.2 and 0.4 m above the floor. 107
- 6.10 Periodic formation and destruction of the vortex core for different burning rates: a) maximum z-vorticity as a function of time; b) maximum z-vorticity spectra. 108
- 6.11 Oscillating flow and combustion in enclosure. Simulations with burning rate coupled with incident heat flux: a) - maximum z-vorticity; b) - fuel mass burning rate; c) - temperature at the centre of the ceiling vent; d) - incoming flow rate through the doorway (lower curve) and outgoing flow rate through the ceiling vent (upper curve). 110
- 6.12 Predicted flame within the enclosure with the symmetrically located doorway: a) mean temperature and velocity fields; b) mean-flow streamlines and 773 K temperature surface (approximates visual flame). Fuel is heptane, mass burning rate is $40 \text{ g}/(\text{m}^2\cdot\text{s})$. 112
- 6.13 Measurements and predictions of heat flux received by the enclosure wall: a) vertical profiles of total (net radiative and convective) heat fluxes; b) heat flux sensors HFS-3; c) predicted distribution of total heat flux received by vertical plane coinciding with the enclosure wall (fuel is ethanol). 113

LIST OF TABLES

1.1	Classification of buoyant rotating flows and rotating flames.	5
2.1	Pool fire characteristics derived from the literature data.	16
3.1	Physical properties of the fuels used.	35
3.2	Characteristics of flames in the open space.	40
3.3	Comparison of burning rates in the open space.	41
3.4	Comparison of flame lengths in the open space.	41
3.5	Measurements results: open non-whirling and enclosed whirling flames.	46
3.6	Time-averaged temperatures at different locations (vertical symmetry axis of the fuel pan).	50
3.7	Time-averaged heat fluxes at the enclosure wall	51
5.1	Mass stoichiometric coefficients (three-reaction scheme).	77
5.2	Sensitivity of the grids used in relation to periodic formation and destruction of the vortex core for a constant prescribed burning rate.	92

NOMENCLATURE

A_{fuel}	Fuel surface area [m^2]
$C_\mu, C_\mu^{min}, C_\omega$	Model constants for turbulent viscosity [-]
C_μ^*	Rotation-modified model constant for turbulent viscosity [-]
C_p	Specific heat capacity [$J/(kg \cdot K)$]
C	Constant [-]
D	Pool/burner diameter [m]
E	Activation energy [$J/mole$]
Ek	Ekman number [-]
f_v	Soot volume fraction [-]
Fr	Froude number [-]
g	Gravity acceleration [m/s^2]
\bar{g}	Gravity vector [m/s^2]
G	Turbulence source term [-]
h	Enthalpy [J/kg]; heat transfer coefficient [$W/m^2 \cdot K$]
I	Radiation intensity [$W/(m^2 \cdot s)$]
k	Turbulence kinetic energy [m^2/s^2]; absorption coefficient [$1/m$]
L	Radiation path length [m]
L_f	Flame length [m]
\dot{m}_{fuel}	Fuel supply rate per unit fuel surface area [$kg/(m^2 \cdot s)$]
p	Dynamic pressure [Pa]
P	Total pressure [Pa]
Pr	Prandtl number [-]
q	Heat flux [W/m^2]
\dot{Q}	Total heat release rate in flame [W]
\dot{Q}^*	Dimensionless heat release rate [-]

Nomenclature

r_0	Vortex core radius [m]
r, θ, z	Polar cylindrical coordinates [m, rad, m]
R	Pool/burner radius [m]
\dot{r}	Production rate of the α -component of the mixture [1/s]
\dot{R}	Reaction rate [1/s]
R_c	Local radius of streamline curvature of mean flow [m]
Re	Reynolds number [-]
Ri	Richardson number [-]
Ro	Rossby number [-]
s_α^i	Mass stoichiometric coefficient for α -component in reaction i [-]
S	Swirl number [-]
Sc	Schmidt number [-]
t	Time [s]
T	Temperature [K]
Ta	Taylor number [-]
u, v, w	Cartesian velocity components [m/s]
v_r, v_θ, v_z	Radial, angular, and axial velocity components [m/s]
V	Velocity magnitude [m/s]; volume [m ³]
\vec{V}	Velocity vector [m/s]
W	Molecular weight [kg/mole]
x, y, z	Cartesian coordinates [m]
x_0, y_0	Cartesian coordinates of flow symmetry axis [m]
Y	Mass fraction

Greek and other symbols

Δ	Change in rate
∇	Gradient operator
Δh_f^0	Standard enthalpy of formation [J/kg]

Nomenclature

$\Delta H_C, \Delta H_C^*$	Net heat of combustion, net heat of incomplete combustion [J/kg]
ΔH_{vap}	Enthalpy of vaporisation [J/kg]
ϕ	Equivalence ratio [-]
α	Mixture component
Γ, Γ_0	Circulation, external circulation [m ² /s]
ε	Turbulence dissipation rate [m ² /s ³]; emissivity [-]
η	Near wall control volumes [-]
κ	Mean absorption coefficient [1/m]
λ	Radiation wavelength [m]
$\mu,$	Turbulent viscosity [Pa·s]
ν	Kinematic viscosity [m ² /s]
ρ, ρ_0	Density, reference density [kg/m ³]
τ	Shear stress [Pa]
σ	Stefan-Boltzmann constant, $5.67 \cdot 10^{-8}$ W/(m ² ·K ⁴)
$\hat{\sigma}$	Stress tensor [Pa]
χ_C, χ_{CO}	Soot and carbon monoxide generation efficiencies [-]
Ω	Angular frequency [rad/s]
$\bar{\omega}$	Vorticity vector [1/s]

Subscripts

<i>abs</i>	Absorption
<i>air</i>	Air
<i>b</i>	Black body
<i>B</i>	Buoyancy
<i>c</i>	Convective
<i>C</i>	Combustion
<i>f</i>	Flame
<i>fuel</i>	Fuel
<i>g</i>	Gas
<i>r</i>	Radiative
<i>r, θ, z</i>	Polar cylindrical coordinates

Nomenclature

<i>s, soot</i>	Soot
<i>SF</i>	Soot Formation
<i>surf</i>	Surface
<i>vol</i>	Volume
<i>t</i>	Turbulent
<i>vap</i>	Vaporisation
<i>SF</i>	Soot formation
<i>w</i>	Wall
<i>wind</i>	Crosswind
0	Initial conditions, ambient atmosphere, reference value

Superscripts

*	Characteristic value
<i>i</i>	Reaction <i>i</i>
'	Turbulent fluctuation

CHAPTER 1.

INTRODUCTION

1.1. Background of the project

The **subject** of this work is the formation and behaviour of fire whirls within enclosures. The existence of this phenomenon must be taken into account in the development of fire engineered solutions, since their success is based on quantitative and detailed analysis of *all* the specific aspects of the design and possible fire scenarios. (as required by the British Standard BS 7974¹).

Previous studies of the structure and dynamics of buoyant turbulent diffusion flames have been mainly focused on flames and plumes developing in a stagnant atmosphere (see a review in [Joulain, 1998]), and, more rarely, when exposed to cross-winds [Mudan and Croce, 1995; Beyler, 2002; Snegirev, 2004]. However, qualitatively different flame behaviour is possible when a whirling flame develops [Emmons and Ying, 1966; Gupta et al, 1984]. Buoyant whirling flames are usually much longer than those observed in ordinary free-standing wind-blown fires. They may be potentially more destructive due to a greater burning rate, increased radiative output and a higher concentration of heat release in a small region of the rotating core. The effect of rotation upon the structure and behaviour of buoyant flames is not similar to that of swirling jet flames, and it has not yet been thoroughly studied. A better understanding is therefore needed to allow efficient techniques to be

¹ The British Standard BS 7974. Application of fire safety engineering principles to the design of buildings. British Standards Institution. UK. 2001-2003.

developed that will counter the possible threat presented; and it can affect the application of fixed fire extinguishing systems. Also, the development and stability of whirling flames are of fundamental interest for refined modelling of coherent and self-organised flame behaviour.

An example of a possible whirling flame in an enclosure is presented in Fig. 1.1 a), where the rotating flame is generated inside the compartment. This flame is indeed much longer than that normally expected, and it can be seen exhausting through the roof. In this case a longer flame provides greater a radiant hazard to its surroundings. The current experimental and modelling studies of whirling flames, such as that shown in Fig. 1.1 b), attempt to give a quantitative and qualitative description of the phenomenon.

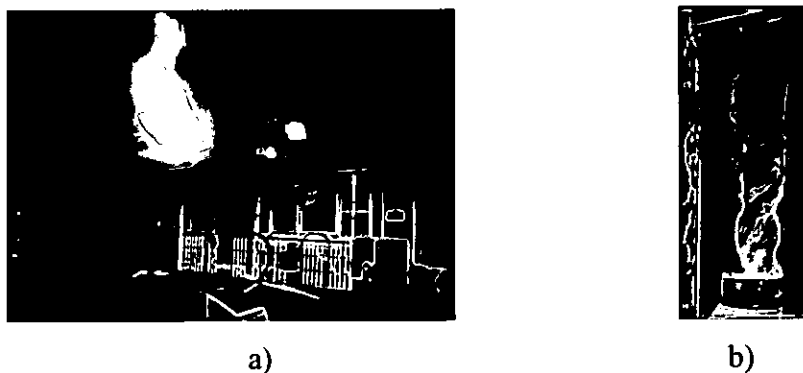


Fig.1.1. Examples of a whirling fire: a) The longer and possibly rotating flame exhausting through the roof vent; b) Whirling buoyant flame in enclosure (the training centre, Greater Manchester County Fire and Rescue Service).

Occurrences of a whirling fire within an enclosure are the direct result of an imposed circulating flow. The literature review provided in Chapter 2 demonstrates that these and other buoyant rotating flows and rotating flames can be classified in terms of three characteristics, these being:

- flow spatial scale;
- the ratio of flow momentum to buoyancy (buoyant of forced jet flows);

- the mechanism (buoyant or forced, external or internal circulating flow) that provides the circulation.

The corresponding classification of buoyant rotating flows and rotating flames is shown in Table 1.1.

Depending on their characteristic size, rotating flows can be regarded as *very large*, *large*, *medium*, and *small*. Very large buoyant rotating flows occur in the great oceans and the atmosphere, having a characteristic size in the order of hundreds of kilometres. Although this work is devoted to whirling flames, reference to very large environmental flows without combustion are also included since they are initiated by similar mechanisms of vorticity concentration and amplification. Large rotating flows occur in the atmosphere (e.g. tornados) and observations of such have been made in large mass fire situations. Studies of small scale rotating flows and flames are relatively commonplace, and technological development has made use of gathered knowledge.

The overview of rotating flows and flames shown in Table 1.1 reveals a gap between the studies and observations available of *large-scale* mass fires, *small-scale* laboratory buoyant flames and swirling flames in industrial burners. The references for medium scale were all written as a result of the registered programme of doctoral studies reported within this Thesis. Indeed, to the current knowledge of the author, no other systematic studies have been reported of *medium scale* (room-size) whirling fires. Experiments reported in this Thesis were therefore required to fill this gap, i.e. to examine the possibility of whirling flame development and its behaviour in compartment fires such as those occurring in industrial and domestic premises.

At the commencement of the current study, the physical mechanisms and necessary conditions for buoyant rotating flames to develop had not been clearly formulated. This called for a study revisiting basic theoretical concepts of rotating flows and for applying it to buoyant turbulent diffusion flames, such as those occurring in natural fires. Thus experimental studies have preceded modelling and computer simulations, with the former improving the latter to overcome the limitations of currently available computational fluid dynamics (CFD) models. Most importantly, through

this work (i) the effect of flow rotation on turbulence, (ii) radiative transfer, and (iii) coupling of fuel burning rate with heat flux received by the fuel surface was accounted for.

Table 1.1. Classification of buoyant rotating flows and rotating flames (*italic notation indicates the scope of this work*)

Flow type	Characteristic size, m	Core flow	Imposed circulation			Occurs in	Described in Ref.
Very large	$10^5 - 10^6$	Buoyant	Earth' rotation – Coriolis force	Forced	External	Oceans and the atmosphere - cyclones	[40, 97]
Large	$10^2 - 10^4$	Buoyant	Wind-shear effect	Forced	External	The atmosphere – tornadoes; refinery oil, forest, city fires	[130]
<i>Medium</i>	<i>1 – 10</i>	<i>Buoyant</i>	<i>Asymmetrically incoming airflow</i>	<i>Buoyant</i>	<i>External</i>	<i>Compartment fires</i>	<i>[81-88, 125-127, 129]</i>
Small	0.01 – 1	Buoyant	Asymmetrically incoming airflow	Buoyant	External	Laboratory flames	[17, 113-117, 39]
			Rotating mesh screen	Forced	External	Laboratory flames	[35, 8]
		Forced	Rotating mesh screen	Forced	External	Laboratory flames	[48]
			Swirl vanes or tangential entry	Forced	Internal	Combustion chambers and industrial furnaces, gasoline and diesel engines, gas turbines, utility boilers etc	[2, 22, 25, 28, 37, 38, 43, 46, 48, 71, 89, 93, 95, 110, 117, 120, 132, 136, 140, 142, 149, 151]

Accordingly, the aim and objectives of this work were formulated. The **overall aim** of this work is to study (experimentally, theoretically, and numerically) medium scale (room size) fire whirls within a compartment. The **specific objectives** of the work include:

1. To examine (theoretically) the physical mechanisms responsible for whirling flames to develop and the conditions necessary for flame rotation to occur.
2. To determine (experimentally) the major characteristics of whirling flames (burning rates, flame heights, heat fluxes and temperatures) and to compare their behaviour to that of non-rotating flames above the same fire source.
3. To study (experimentally and numerically) the transient behaviour and determine the periodicity of such flames using a range of different fuels.
4. To modify, adjust, apply and validate a CFD model that is capable of reproducing rotating flames both in an open space and within an enclosure. The burning rates, heat fluxes and temperatures predicted by the model to be validated by the experimental work undertaken in Chapter Three.
5. To undertake numerical simulations of whirling flames in an open space and in an enclosure replicating the behaviour observed in the experimental work and to interpret both experimental and computational results in terms of the existing theory of rotating flows.

In this work, experimental observations of medium (room-size) scale whirling fires are presented, demonstrating that whirling flames may develop within compartments. The periodic formation and destruction of the whirling core and the resulting increase in time-averaged burning rate are also addressed. Basic concepts of rotating flows are then summarised, illustrating the mechanism of development of buoyant whirling flames and the conditions required for flame rotation to occur. A CFD model is discussed and modified to represent the response of a buoyant turbulent diffusion flame upon the imposed circulation causing a decrease of turbulent mixing. The model is consequently applied to simulate buoyant whirling flames in an open space and in the enclosure representing that used in the experiments; and for a range of geometrical arrangements.

Finally, the results of this work, its novelty and contribution are summarised together with avenues of further research suggested.

1.2. Outline of the Thesis Chapters

Chapter One “Introduction”. This chapter contains a brief discussion of the background to the research and an overview of the research undertaken. An analysis of the current state of research is given in tabular form clearly identifying the “gap” that this piece of research attempts to fill.

Chapter Two “Literature Review”. The literature review consists of two sections: firstly the behaviour of pool fires are discussed; and secondly a synopsis is given of prior research undertaken in respect to whirling fires.

Chapter Three “Experimental Studies of Whirling Flames”. A detailed description is given of how medium scale whirls are produced within a test enclosure. This chapter covers the experimental apparatus and methodology employed in the formation and recording of such whirls. Two distinct regimes are considered, namely fires within enclosures and in the open space. The chapter concludes with a presentation and discussion of the results obtained from the experiments.

Chapter Four “Basic Theoretical Concepts of Rotating Flows and Flames”. A description of the physical mechanisms that cause vorticity concentration and amplification is presented. The chapter firstly presents basic considerations of rotating flows and concludes with a discussion of the dimensionless parameters that are associated with whirling fires.

Chapter Five “Mathematical Model and CFD Code”. A description is given of the mathematical model and CFD code used in the simulations. The chapter describes the modifications made to the turbulence model as part of this work.

Chapter Six “Numerical Simulations of Whirling Flames”. A discussion of the results of the numerical simulations is undertaken in respect to medium scale fire whirls. The chapter considers the formation of a fire whirl within an open space, above the same fuel source as that in the enclosure. Then the formation of the fire whirl within the enclosure is analysed. Comparisons are made with the experimental data gathered from the experiments.

Chapter Seven “Conclusions”. A summary is given of conclusions in respect to the experimental, theoretical and numerical studies, coupled with suggestions for future work within this area of research.

CHAPTER 2.

LITERATURE REVIEW

2.1. Introduction

The literature review is divided into two distinct parts. The first part outlines the behaviour of *non-rotating flames* in pool fires within a stagnant atmosphere and when exposed to cross-winds. The second part concentrates on the behaviour and existence of large and small scale *fire whirls* that are either the result of large mass fires or laboratory experiments.

Enforced rotation of the fuel and oxidiser is widely used in industrial applications such as in gas turbines and swirl burners. Rotation of the fuel/gas mixture results in a shorter flame length and therefore a more compact burner size. Research in this field is well reported in literature and only a brief overview is made in this review. However in the case of rotating flames induced by externally imposed circulation, the flame response is qualitatively different; in particular, flame elongation is observed and the fuel mass burning rate increases [Emmons and Ying, 1966; Satoh and Yang, 1996; and others]. The review of previous research will demonstrate that the behaviour of *medium* scale fire whirls within enclosures has not yet been studied, although large and small scale fire whirls as defined in Table 1.1 have been investigated.

Before commencing a literature review on non rotating flames and fire whirls, the nature of buoyant turbulent diffusion flames must be first understood. Depending on the ratio of momentum introduced by the fuel flow to that generated by buoyancy, two distinct types of turbulent diffusion flames, namely *buoyant* and *jet* flames, can

be identified. The dimensionless criteria that expresses the above ratio is the Froude number,

$$Fr = \frac{V_{fuel}^2}{gD}, \quad (2.1)$$

where V_{fuel} is the gas (vapour) fuel velocity emanating at the surface of the condensed fuel, or emitted axially from a gas burner outlet, and D is characteristic size (diameter) of the fuel surface or burner bore.

Along with the Froude number, Eq. (2.1), dimensionless heat release rate is given as,

$$\dot{Q}^* = \frac{\dot{Q}}{\rho_0 C_{p0} T_0 \sqrt{gD} D^2}, \quad (2.2)$$

and is used as an important criteria for determining flame type (see [Zukoski, 1995; Drysdale, 1999]). Using the relationship between fuel velocity and heat release rate,

$$\dot{Q} = \Delta H_C \dot{m}_{fuel} A_{fuel} = \Delta H_C \rho_{fuel} V_{fuel} \frac{\pi D^2}{4}, \quad (2.3)$$

it can be demonstrated that Fr and \dot{Q}^* are related to each other.

Apart from heat release rate, the flame characteristic that is of primary importance in fire safety engineering is the *flame length*. The empirical data available for the flame length are usually expressed as a function of \dot{Q}^* , and the correlations are different depending upon the flame type (i.e. buoyant or jet). For example, *jet flames* are limited such that $Fr \gg 1$ and $\dot{Q}^* > \dot{Q}_B^*$ (where \dot{Q}_B^* is a conventional threshold value, see [Heskestadt, 1986]) and the flame length does not depend on \dot{Q}^*). One of the flame length correlations available in the literature is given in [Beyler, 2002]:

$$L_f = 15 \frac{1}{C_{fuel}} \sqrt{\frac{W_{air}}{W_{fuel}}} D \quad (2.4)$$

where D is the jet nozzle diameter, C_{fuel} is volume fraction of fuel in a stoichiometric fuel-air mixture (e.g. 0.091 for methane, 0.074 for ethane, 0.038 for propane), and W_{air} , W_{fuel} are the molecular weights. The relationship (2.4) shows that $L_f \gg D$ for jet flames.

Alternatively, for *buoyant flames* the condition $Fr \ll 1$ holds, and the flame length scales with \dot{Q}^* . It has been established (for example, see [Heskestadt, 2002]), that if $\dot{Q}^* < 0.1$ (very large pool fire) then $L_f \propto \dot{Q}^{*2}$ and $L_f < D$; whereas if $1 \leq \dot{Q}^* \leq \dot{Q}_B^*$ (medium to large pool fires) $L_f \propto \dot{Q}^{*2/5}$ and $L_f > 3D$. The latter range covers the interval of sizes corresponding to compartment fires (the flames studied in this work fall into this range). In this case, the most popular empirical flame length correlation for buoyant turbulent diffusion flames in still air (normal atmospheric conditions, no crosswind) is that given by Heskestadt where:

$$L_f = 0.235 \dot{Q}^{*2/5} - 1.02D, \quad (2.5)$$

and \dot{Q}^* must be in kW [Heskestadt, 1986]. In Chapter 3 of this work this empirical relationship will be used to verify our observations of flames in the open space.

This work is concerned with the behaviour of pool fires corresponding to buoyant flames with $Fr \ll 1$ and $\dot{Q}^* \approx 1$. The flames can either occur in stagnant atmospheres or be exposed to external disturbances such as (crosswind or circulating flow). These scenarios may develop both in the open space and within enclosures and the appropriate classification is determined by Fig. 2.1.

As shown in Fig. 2.1, the case of whirling fires studied in this work presents a special case of buoyant turbulent diffusion flame that is exposed to external circulation.

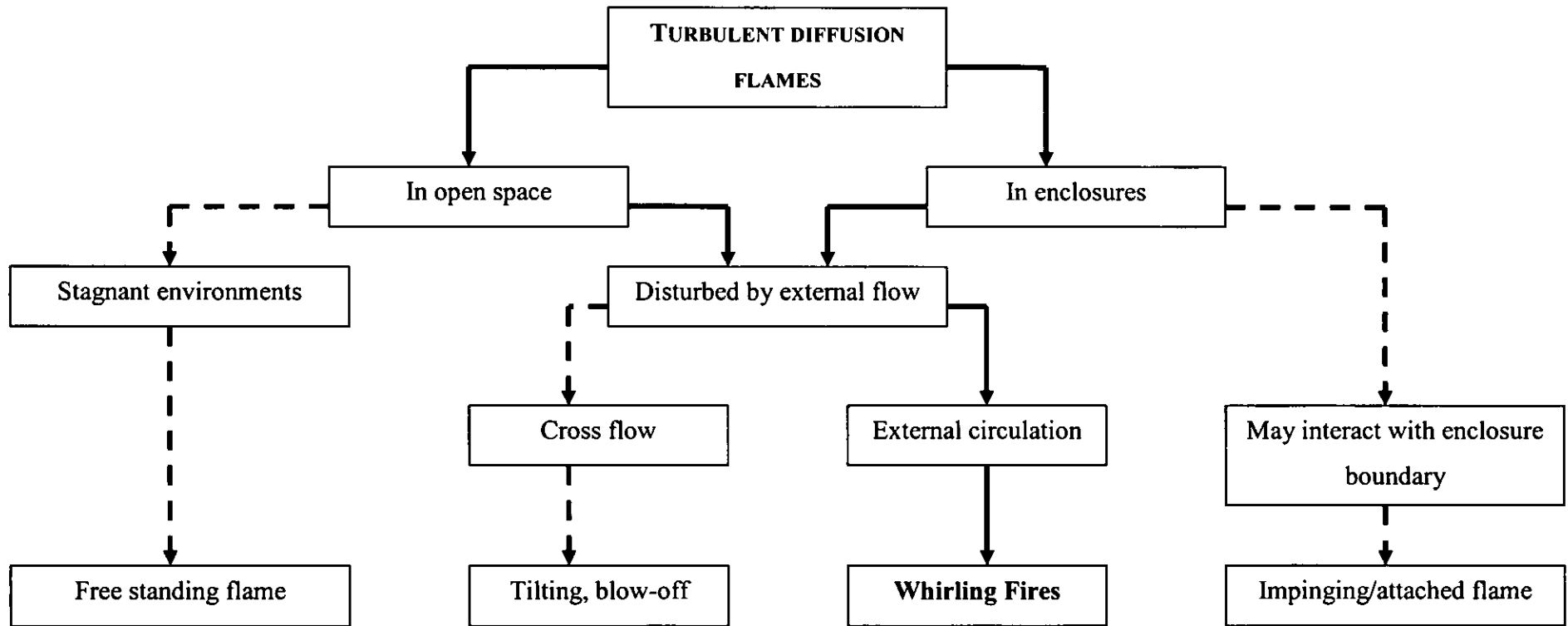


Fig 2.1. Flame types covered in the literature review (solid lines illustrate the relevance of this work)

2.2. Liquid fuel pool fires in still air

Here, pool fires are considered above combustibles that are in the liquid state under normal atmospheric conditions. The most carefully studied (although somewhat ideal) is the case of burning in a stagnant environment, with no organised external flow such as crosswinds or draughts. If ignited, such a fire is a self-sustained process of turbulent diffusion combustion that is fed by the evaporating fuel; sustained by heat flux from the gas flame to the fuel liquid surface.

Self-sustained buoyant turbulent diffusion flames above a liquid and solid fuels are a phenomenon encountered in a wide range of applications. Accidental fuel spill fires in residential and industrial compartments, in fuel stores, on ship decks, rail tankers and offshore platforms, in plane crashes and petrochemical industrial processes are some of the examples of hazards caused by burning pools. These events have stimulated significant long-standing research of liquid pool fires burning in open environments and enclosures ([Blinov and Khudiakov, 1961; Mudan and Croce, 1995; Babrauskas, 1996; Drysdale, 1999; Joulain, 1998; Gottuk and White, 2002; Beyler, 2002], among many others).

The burning of a liquid fuel is a complex process comprising fuel evaporation, vapour diffusion, turbulent mixing, combustion, thermal radiation, conjugate heat and mass transfer at the fuel surface and to surrounding structures. Since the pioneering work (e.g.[Blinov and Khudiakov, 1961]), qualitatively different burning regimes were identified that were dependant upon the pool diameter. Three regimes can be distinguished [Hottel, 1958].

- Small pool diameter, $D < 0.03$ m. The flames are laminar, optically thin, and fuel lean due to an excess of entrained oxygen and the burning rate decreases with an increase of diameter.

- Intermediate pool diameter, $0.03 < D < 1.0$ m. The flame behaviour is transitional between laminar and turbulent, optically thin and optically thick, fuel-lean and fuel-rich flames. The burning rate increases as the diameter of the fuel burner increases.
- Large pool diameter, $D > 1.0$ m. The flames are turbulent, optically thick and the fuel-rich core has a lack of oxygen and in this case the burning rate does not depend upon the pool diameter.

This work is mainly concerned with pool sizes, which fall in the range of the intermediate (according to the above classes) to large pools and in this case the development of a turbulent flame above the pool is governed by radiative feedback from the flame to the fuel surface. In this range it has been firmly established (see [De Ris, 1978], [Markstien, 1978], [Modak and Croce, 1995] among others) that radiant feedback controls the combustion rate of the fuel bed, and the higher the radiant feedback value to the fuel surface, the greater is the fuel vaporisation rate. The radiant emission from the flame is determined by flame temperature and composition. The main combustion products contributing to the radiant emission and absorption are soot, carbon dioxide and water vapour, although the role of unburned hydrocarbons (in the fuel rich core near the fuel surface) and of carbon monoxide may also be significant. For various hydrocarbon pool fires, the heat radiated by flame is within the range from 7 to 60% [Modak and Croce, 1995], and it correlates well with the soot yield. For example, the radiative fraction in open low-soot ethanol flame is about 7%, whilst in very sooty heptane flame it is about 40%.

Approximate models were developed to allow for radiative feedback in pool fires [Orloff, 1980; De Ris, 1979; Adiga et al, 1989; Souil et al, 1984, Modak and Croce, 1995; Beyler, 2002]. Usually a real flame is approximated by either a point source or “solid” radiating body of simplified (cylindrical or conic) shape. In more advanced CFD models a range of methods to simulate thermal radiation transfer are used. The available approaches are the discrete ordinates, the discrete transfer, the finite-volume, the multi-flux and moment, the spherical harmonics (usually P1

approximation), and the statistical (Monte Carlo) methods (for example, see [Modest, 1993; Cox, 1995]).

In experiments with pools of $D > 0.2$ m, the burning rate ($\text{kg}/(\text{m}^2\cdot\text{s})$) was found to increase with pool diameter until reaching a constant value in the case of large pools. The existing experimental data on mass burning rate, \dot{m}_{fuel} , can be approximately represented by the formulae

$$\dot{m}_{fuel} = \dot{m}_{fuel\infty} (1 - \exp(-k_f D)), \quad (2.6)$$

where $\dot{m}_{fuel\infty}$ is the mass burning rate of a very large pool, k_f is the effective flame absorption coefficient and D is the pool diameter. Databases covering a number of practically important fuels are available e.g. in [Mudan and Croce, 1995] and [Babrauskas, 1983; 1996]. Burning rate, heat release rate, and flame length estimates of pool fires originated by the three fuels used in this work are given in Table 2.1. Note, the three fuels chosen exhibit *significantly different* burning rates when burning in free-standing pool fires. They were chosen for this reason and for their range of soot production.

Steady mass burning rate of large pools were also found to correlate with fuel thermo-chemical properties. The relationship between mass burning rate and the ratio of the heat of combustion ΔH_c , and heat of vaporisation, ΔH_{vap} , are given by the empirical relationship

$$\dot{m}_{fuel\infty} = 0.001 \frac{\Delta H_c}{\Delta H_{vap}}, \text{ kg}/(\text{m}^2\cdot\text{s}), \quad (2.7)$$

which covers a wide range of hydrocarbon fuels [Mudan and Croce, 1995].

Table 2.1. Pool fire characteristics derived from the literature data

Fuel	\dot{m}_{fuel}^a , kg/(m ² ·s)	k_f^a , 1/m	ΔH_c^b , MJ/kg	Data for $D = 0.6$ m diameter pool		
				\dot{m}_{fuel}^c , kg/(m ² ·s)	\dot{Q} , kW	L_f^d , m
Ethanol	0.014-0.016	0	26.8	0.014-0.016	106-120	0.91-0.98
Diesel ^c	0.036-0.042	2.7-4.3	44.1	0.028-0.038	350-470	1.8-2.1
Heptane	0.092-0.120	0.8-1.4	44.4	0.034-0.060	430-750	2.0-2.7

^a See [Babrauskas, 1983]

^b See Table C1 in SFPE Handbook of Fire Protection Engineering, 3rd Ed., NFPA, 2002.

^c Eq. (2.6) for upper and lower mass loss rates quoted

^d Eq. (2.5) for upper and lower values of heat output

^e Data for kerosene, $C_{14}H_{30}$, are used hereafter.

Mass burning rates of liquid pools may significantly depend upon the heat loss rate from the fuel layer. In particular, in shallow spillages above the solid (or liquid) surface, the heat flux to the substrate may observably reduce the mass burning rate when compared to that in deeper pans. The recently reported spill fire burning rates [Gottuk and White, 2002] are remarkably (by a factor of about five) lower than those given in [Babrauskas, 1996]. Therefore, the heat loss rate should be taken into account in simulations of self-sustained pool fires. Special consideration may also be needed for heat exchange within the pan rig, as indicated in [Nakakuki, 1997; Nakakuki, 2002].

In the majority of cases there is a time period following ignition until the whole of the surface of the fuel bed is involved in the combustion process. Duration of this period is governed by the area of the fuel pan and the volatility of the fuel itself [Cline and Koenig, 1983]. During this period, the fuel mass loss rate from the fuel surface will steadily increase as more of the surface of the fuel is involved in flame. When the whole surface of the fuel is fully involved the mass loss rate will reach a steady value (provided that the heat losses to the fuel and surroundings are constant). If these heat losses are not constant then the mass loss rate will vary with time. It is therefore important for the accurate measurements of burning rates to ensure steady state conditions exist. Mass loss rate is affected by any changes within the fuel pan; such as a change in the level of the liquid. This change of level increases the area of the available freeboard and therefore affects the heat transfer to/from the surrounding medium [Hayasaka, 1996]. Any experimental work should preferably be conducted with a constant freeboard.

2.3. The effects of cross-wind

In previous studies of flames subjected to a cross-wind, augmentation of the burning rates was experimentally observed [Blinov and Khudiakov, 1961; Quintiere, 1989] and acceleration of flame spread was numerically predicted [Porterie, 2000]. If the velocity of a cross-wind exceeds a critical value, flame blow-off occurs and the combustion process ceases [Blinov and Khudiakov, 1961; Capener and Alger, 1972].

The velocity of cross-winds can have an effect upon flame radiation and this is considered in [Mudan and Croce, 2002; Beyler, 2002; Snegirev, 2004].

There is controversy in the effect of a crosswind upon the burning rates measured in different experimental conditions. For example, Capener and Alger [Capener and Alger, 1972] studied a 1 m diameter pool fire burning in a cross-wind of 6 m/s and found that the mass loss rate from the surface was half the value of that in still air. However, Lois and Swithenbank [Lois and Swithenbank, 1978] reported a doubling of the mass loss rate in a pool fire when subjected to a cross wind. A possible explanation for these differing conclusions is a *non-monotonic* dependence of the burning rate on the wind velocity. Indeed, a cross-wind brings extra oxidiser into the flame zone and simultaneously tilts the flame, causing a distribution of a greater fraction of radiated heat outside the fuel surface. As a result, the effect of cross-wind on burning rates may be qualitatively different, depending on whether the extra oxidiser entrained is used in the reaction zone to increase flame temperature and, consequently, the radiative output. The latter is determined by the size of the pool (and flame above it), i.e. whether or not the flame is well ventilated or the fuel-rich core develops. This is also supported by recent numerical studies of the dependence of mass burning rate on the cross-wind velocity [Snegirev, 2004].

In the case of a pool fire within a compartment, the effect of airflow coming through openings is similar to that of a cross-wind in an unconfined space. For example, Quintiere and co-workers [Quintiere et al, 1981] have demonstrated that the inflowing gases resulted in improved mixing of the fuel and oxidiser.

A number of empirical correlations is recommended for predicting the flame tilt angle θ (angle between the flame and the vertical) resulting from a crosswind. In particular, according to the American Gas Association (see [Beyler, 2002]),

$$\cos \theta = \min \left(1, \frac{1}{\sqrt{V_{wind}^*}} \right), \quad (2.8)$$

where $V_{wind}^* = V_{wind} / (g \dot{m}_{fuel} D / \rho_{fuel})^{1/3}$ is the non-dimensional wind velocity.

Details on the effects of cross-winds on flame length and flame shape of *jet flames* can be found in [Mudan and Croce, 1995] and [Beyler, 2002].

2.4. The effect of external circulation

External circulation is another type of the external disturbances that may be imposed upon a buoyant flame (see Fig. 2.1). Externally imposed circulation may result in flame rotation, which significantly changes the flame shape and behaviour. The physical mechanism causing circulating flows may be of a very different nature. For example, the Earth's rotation may provide such external circulation for very large scale whirling flows in oceans and the atmosphere, whilst wind-shear supplies the external circulation required for tornados and large mass fire storms. An asymmetrically incoming airflow may play a similar role in the formation of whirling fires within enclosures. Here, a review of experimental observations, approximate theoretical approaches, and CFD studies of rotating flames is given. The flows and flames are classified in terms of the following three characteristics: the ratio of flow momentum to buoyancy (buoyant or forced jet flows), the mechanism (buoyant or forced, external or internal circulating flow) that provides the circulation, and flow spatial scale. This classification of rotating flows and flames is illustrated by Table 1.1 of the Introduction.

Depending on their characteristic size (see Table 1.1), rotating flows can be regarded as very large, large, medium, and small.

2.4.1. Large scale fire whirls

Very large buoyant rotating flows occur in oceans and the atmosphere [Morton, 1970; Fernando and Smith, 2001]; and in this case background weak external vorticity introduced by the Earth's rotation is concentrated into a whirling core of

characteristic size of about 10^5 m. The work [Fernando and Smith, 2001] contains a review of buoyancy driven circulation patterns, including environmental plumes and thermals.

In *large* buoyant whirls, such as those produced in oil, forest or city fires, the external circulation imposed due to wind-shear effects is supposed to be the primary source of the vorticity, which is then concentrated and amplified in the rising buoyant flow. The height of the whirling core may range from a very small size up to a few hundred meters. Soma and Saito [Soma and Saito, 1991] provided categorisation and historical examples of large fire whirls. The fire whirls observed can be categorised as stationary and moving types. Stationary whirls are represented, for example, by the Hamburg mass fire, 1943. Moving types may appear as a whirl core separated from the fire area. Moving whirls may also be attached to the fire and carry flame. Such an example is a fire that occurred in downtown Tokyo, 1923, following an earthquake [Soma and Saito, 1991].

Due to the destructive nature of large scale fire whirls they are very difficult to study experimentally. High entry velocities (up to about 100 m/s) and sheer scale mean that the only effective way to experimentally study the physics of such whirls is at a smaller scale.

2.4.2. Small scale rotating flames

2.4.2.1. Enforced (jet) swirling flows

Small scale rotating flames (see Table 1.1) can be produced by a forced flow or by buoyancy¹. Important examples of forced rotation are *jet swirling flames*, which are intensively employed in industrial applications, in particular in combustion chambers and industrial furnaces, gasoline and diesel engines, gas turbines and utility boilers. The swirling is used as a means of controlling flame size, shape, stability, and

¹ In this work we will refer to *buoyant* rotating flames as *whirling* whereas *forced (jet)* rotating flames will be denoted as *swirling* ones.

combustion intensity. The swirling flows result from the enforced spiralling motion and swirl velocity component (azimuthal or angular velocity). This flow is imparted by swirl vanes or by tangential entry into the chamber [Gupta et al, 1984; Sloan et al, 1986; Kuroze et al, 2004] (Fig. 2.2).

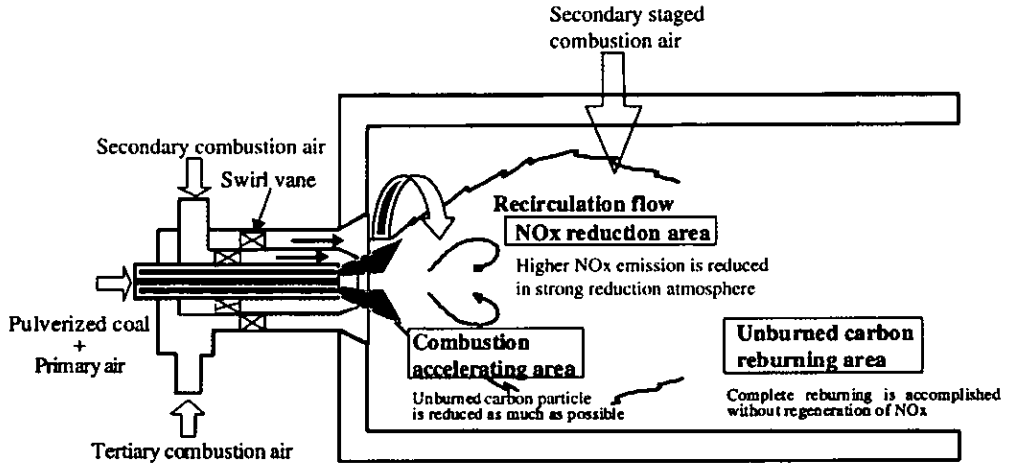


Fig. 2.2. Entry swirl generator by the use of swirl vanes [Kurose et al, 2004].

Due to its importance in industrial applications, jet swirling flows have been thoroughly studied [Falco, 1977; Gupta et al, 1984; Milosavljevic et al, 1990; Weber and Dugue, 1992; Zhang and Hill, 1996; Faltsi-Saravelou et al, 1997; Xia et al, 1998; Morcos and Abdel-Rahim, 1999; Chuang et al, 1999; Cha et al, 1999; Underwood et al., 2000; Cheng et al, 2001; Gradinger et al, 2001; Masri et al, 2004; Selle et al, 2004].

The structure of these flows was found to depend on the degree of swirl, which is characterised by the swirl number, S . The latter is the ratio of the axial fluxes of angular and axial momentum [Gupta et al, 1984], that can be approximately defined as

$$S = \frac{\int_0^{\infty} \rho v_z v_{\theta} r^2 dr}{\frac{D}{2} \int_0^{\infty} \rho v_z^2 r dr}, \quad (2.8)$$

where the contribution of turbulent fluctuations are neglected. At high degrees of swirl, the vortex core becomes unstable, it exhibits oscillatory behaviour and, if the swirl is further increased ($S > 0.6$ [Gupta et al, 1984]), vortex breakdown occurs. The recirculation zone develops, with the shape of an oscillating bubble. This time-dependent coherent structure is referred to as the precessing vortex core (see Fig. 2.3b). As a result, the lateral spreading of the flow is increased and the decay of the axial velocity is facilitated. Accordingly, turbulent mixing and the reaction rate are increased, resulting in flame shortening when compared to a non-swirling one.

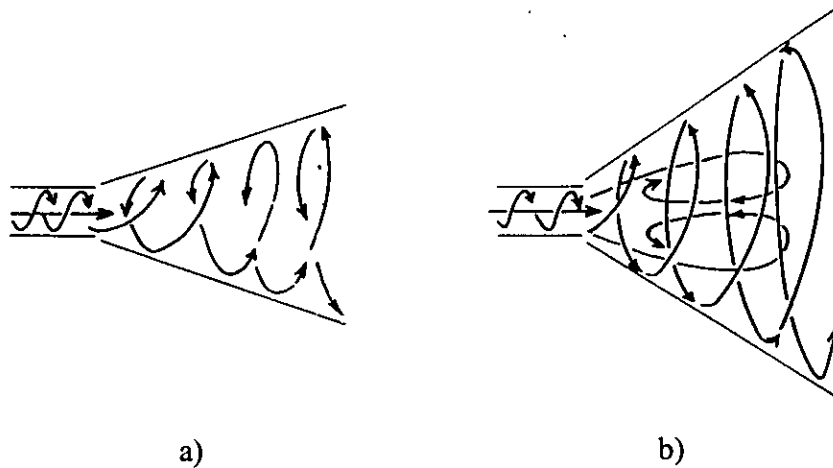


Fig. 2.3. The structure of jet flows with a different degree of swirl [Gupta et al 1984]: a) $S < 0.6$; b) $S > 0.6$.

Thus, in jet swirling flames, swirling is imposed *internally* due to the rotation of forced incoming flow of reactants. However a qualitatively different effect of rotation upon turbulent mixing and flame length has been observed in flows and flames submerged into a rotating flow environment, i.e. where the circulation is *externally* imposed. In this case (the example of forced flow is the flow in a rotating pipe [Imao et al., 1996]; buoyant whirling flames studied here also fall in this category), the intensity of turbulence has been shown to decrease due to rotation because of the stabilising effect of the centrifugal force.

2.4.2.2. Buoyant whirling flows

Studies of *buoyant flames* in rotating flow environments were initiated by the work of [Byram and Martin, 1962], where the rotation of buoyant flame above an alcohol pool was induced by tangential airflow incoming into the cylindrical chamber through vertical slits in its walls. Whirling flame development was observed and, in contrast to that observed in the case of jet swirling flames, flame elongation occurred. More consistent measurements and observations together with simplified modelling were carried out using the work of Emmons and Ying [Emmons and Ying, 1966]; in which a cylindrical penetrable rotating screen (3.0 m height, 2.2 m diameter) was used as a source of the external circulating flow which, was imposed on the buoyant flame situated above a 0.1 m diameter acetone pool. Flame elongation was again noted with imposed circulation (see Fig 2.4).

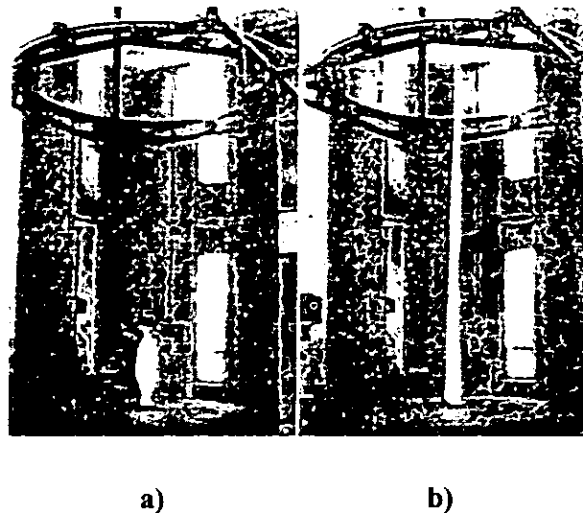


Fig. 2.4¹. The effect of the imposed circulation on flame length: a) free-standing non-disturbed flame; b) whirling flame inside rotating screen cylinder [Emmons and Ying, 1966].

The rotation of the screen produced circulation values up to about 4 m²/s. Significant (by a factor of 5) flame elongation was obtained when the vortex core developed.

¹ Illustration taken from aged publication, other examples of this method are not available.

Burning rates substantially increased when compared to non-whirling fires of the same size. This flame elongation was attributed to the decrease of turbulence intensity, air entrainment and its mixing with the fuel, resulting from the stabilising role of centrifugal forces. Similar conclusions were derived by [Chigier et al, 1970], [Beer et al, 1971] and [Beer and Chigier, 1972], who studied similar flames with a controlled fuel supply rate (burner fires) also surrounded by rotating screens.

The above experiments are of flames with *enforced* external circulation. External circulation may also be induced by asymmetrically incoming *buoyant* airflows, such as in the experimental enclosure with 4 vertical gaps between the walls (see Fig. 2.5), which was used by [Soma and Saito, 1991], [Satoh, 1996], [Satoh and Yang, 1996-1999]. In these experiments different types of fuel (heptane, kerosene, ethanol and wood) were burned in pools, the sizes being from 8 to 20 cm in diameter and at some particular gap widths, flame rotation was observed. Similar to the earlier experiments with enforced circulation, a decrease in turbulent fluctuations and increase in flame length and its luminosity was clearly indicated for buoyant circulation induced rotating flows when compared to non rotating flames. Although reference is made to an increase of mass burning rate, no quantitative results have been provided. In [Satoh and Yang, 1996], instability of the whirling flame was observed and if its height exceeded that of the walls, then the vortex core was destroyed.

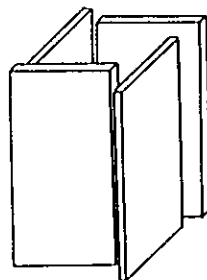


Fig. 2.5. Enclosure geometry for a small scale whirling flame [Satoh and Yang, 1996].

Small scale whirls have also been generated using gas burners [Soma and Saito, 1991].

Thus, the behaviour of *buoyant* whirling flames and plumes is remarkably different when compared to *forced* swirling jets. It has first been established in the experiments using a buoyant rotating flame above an acetone pool developed inside a rotating screen [Emmons and Ying, 1966] and later confirmed in subsequent works [Chigier et al, 1970; Beer et al, 1971; Beer and Chigier, 1972; Satoh, 1996; Satoh and Yang, 1996, 1997] that rotation decreases the turbulence in the rising core thus inhibiting turbulent mixing at the core boundary and the air entrainment through it. As a result, dissimilar to forced swirling flows in industrial burners, rotation of buoyant flows causes flame lengthening, with no recirculating zone inside the core.

2.4.3. Medium scale fire whirls

In his review, Pitts [Pitts, 1990] mentioned rare occurrences of whirling fires being several meters in height. However, consistent studies of *medium* scale (as defined in Table 1.1) buoyant whirling flames with characteristic size of the order of 1 - 10 m do not appear to have been reported prior to the work undertaken for this Thesis. Nevertheless, this range corresponds to room-size compartments where the external circulation of asymmetrically incoming buoyant airflow through the openings may potentially result in creation of fire whirls. Although reports on the occurrence of these phenomena are rare they are potentially destructive so are of importance to fire fighters. Lack of quantitative information about these types of flames and the need to clarify the conditions for this phenomenon to occur motivates this work.

2.4.4. Theoretical studies and modelling of fire whirls

Theoretical studies of buoyant whirling flows have mainly been undertaken for environmental flows *without combustion*. Morton [Morton, 1970] discussed the different mechanisms of vorticity production and amplification, emphasising the role

of ambient vorticity. Stretching of the vortex tubes¹ within a buoyant rising flow is identified as an important feature in the amplification of vorticity. The Rossby number, one of the governing criteria, was introduced and estimated for a range of whirling flows. A more recent review of buoyancy driven circulation patterns, including plumes and thermals, is given in [Fernando and Smith, 2001].

Available theoretical analysis of *buoyant rotating flames* is based on strict limitations of the integral model [Emmons and Ying, 1966] and the inviscid flow assumption [Battaglia et al, 2000]. There have been only few attempts to carry out CFD modelling of whirling flames [Sato and Yang, 1998; Sato and Yang, 1999; Battaglia et al, 2000], and the models used were oversimplified. For example, combustion and thermal radiation were not modelled in [Sato and Yang, 1998; Sato and Yang, 1999], where a constant volumetric heat source was assumed. In the works cited, neither the effect of flow rotation upon turbulent fluctuations and relating the fuel burning rate together with the heat flux at the fuel surface was considered. Computations [Battaglia et al, 2000] have not reproduced the substantial lengthening of rotating flames observed in experiments [Emmons and Ying, 1966]. Clearly, there is a lack of experience in turbulence modelling of buoyant reacting flows with strong effect of rotation.

The progress in modelling forced swirling flows and flames is much more pronounced. Here, the primary challenge was to develop turbulence models suitable to feature strong curvature of the streamlines in swirling flows. Limitations of conventional two-equation turbulence models have been recognised some time ago [Saffman, 1977; Srinivasan and Mongia, 1980; Abujelala and Lilley, 1984]. A number of approaches to improve these types of models were developed [Nikjooy et al, 1989; Sturgess and Syed, 1990; Weber et al., 1990; Morsi, 1995; Lai, 1996; Lei, 2000] including those based on:

- eddy-viscosity models [Sloan et al, 1986; Fu et al, 1988; Chang and Chen, 1993; Chen and Chang, 1995; Wall and Taulbee, 1996];

¹ These being lines that pass through some simple closed curve in space are said to form a vortex tube. See Acheson Elementary Fluid Dynamics page 162.

- Reynolds stress models [Jones and Pascau, 1989; Hogg and Leschziner, 1989; Zhou et al, 2003]
- large-eddy simulations [Conway et al, 2000; Wegner et al, 2004] and
- stochastic models [Repp et al, 2002].

Swirling flows have been modelled both with and without combustion. Experience gained in modelling jet swirling flows can be instructive when attempting to simulate buoyant whirling flames. Further discussion of this subject is given in Section 5.3 of this work.

In recent decades, there have been significant improvements in the ability to numerically simulate fires within compartments by means of CFD. This is gradually becoming a routine tool for fire safety engineers. The review by Novozhilov [Novozhilov, 2001] demonstrates a successful application of various approaches to turbulence modelling, including the use of Reynolds averaged Navier Stokes equations (RANS) and Large Eddy Simulations (LES). Also, powerful software packages have been developed, which can be broadly divided into fire-specific and general-purpose CFD codes. The most successful *fire specific* packages include:

- JASMINE¹ (Fire Research Station, UK), for example, see [Cox et al, 1986; Cox, Kumar, 1987; Kumar, Cox, 1989; Kumar et al, 1991; Kumar et al, 1997; Miles et al, 1997; Chitty and Kumar, 2004; Hua et al, 2004; Miles and Kumar, 2004]
- SOFIE² (Cranfield University, UK), for example, see [Lewis et al, 1997; Li et al, 1999; Sanderson et al, 1999; Lewis et al, 2000]
- SMARTFIRE³ (Greenwich University, UK), for example, see [Galea and Markatos, 1989; Kerrison et al, 1994; Jia et al, 1997; Ewer et al, 1999; Wang et al, 2001; Hurst-Clark et al, 2004; Jia et al, 2004; Zhang et al, 2004]

¹ www.bre.co.uk. FRS Division of BRE. Garston. Watford. UK.

² www.cranfield.ac.uk. Cranfield University. Cranfield. Bedfordshire. UK.

³ www.fseg.gre.ac.uk. University of Greenwich. Queen Mary Building. Greenwich. London. UK.

- Fire Dynamics Simulator, FDS¹ (NIST, USA), for example, see [McGrattan et al, 1998; Fleischmann and McGrattan, 1999; Xin et al, 2002; Mammoser and Battaglia, 2004].

The *general purpose* commercially available codes can also be used efficiently to undertake fire simulations and the most widely used are CFX², FLUENT³ and STAR CD⁴.

In this work it was decided to use an 'in house' developmental code *Fire3D*. This code differs from commercially available codes in that that it employs a Monte Carlo approach to heat flux modelling as opposed to the six flux method. Another consideration taken into account to use this particular code was that being developed 'in house' modifications to the parameters could be easily undertaken.

For research purposes, in-house software can provide more flexibility and opportunities for modifications needed to investigate a phenomenon of interest. In this work, the model and code *Fire3D* earlier developed by Dr Snegirev (Centre for Research in Fire and Explosion Studies, University of Central Lancashire, Preston, UK) was used. The model and code was created for and applied in unsteady RANS modelling of open and enclosed buoyant turbulent diffusion flames [Snegirev et al; 2001; 2003; 2004]. The model and code has certain advantages over the other fire-specific and general-purpose commercial computer codes used in the field; these advantages include statistical (Monte Carlo) modelling of radiative transfer, consideration of conjugate heat transfer at solid surfaces and prediction of the 3D transient temperature field inside the solid material, and of liquid/solid fuel combustion with burning rate determined by thermal feedback between flame and fuel surface. For successful completion of this work, however, a modification of the turbulence model previously used in *Fire 3D* was necessary. Such a modification is described in Section 5.3.

¹ www.nist.gov. National Institute of Standards and Technology.USA.

² www.waterloo.ansys.com. CFX Gemini House. Didcot. Oxford. UK.

³ www.fluent.com. Sheffield Business Park. Sheffield.UK.

⁴ www.Cd-adapco.com. 200 Shepherds Bush Road. London. UK.

2.5. Conclusions

Two major conclusions from previous studies of rotating flames can be identified. *Firstly*, there have only been a few experimental studies undertaken in respect to buoyant whirling flames. None of these studies addressed medium (room-size) fire whirls of a spatial scale between 1-10 meters. These types of flame are particularly important for the study of compartment fire dynamics. *Secondly*, the knowledge gained in extensive previous studies of jet swirling flames is not directly applicable to buoyant whirling flames and indeed, qualitatively different effects of rotation upon turbulent mixing and flame length have been observed. Therefore experimental, theoretical and numerical studies are required to provide a clear explanation and quantification of the formation and stability of buoyant whirling flames. Validations of the CFD model used to replicate these types of flames are also of importance if accurate and meaningful numerical simulations are to be undertaken. Further chapters of the Thesis will present work undertaken within the above avenues.

CHAPTER 3.

EXPERIMENTAL STUDIES OF WHIRLING FLAMES

3.1. Introduction

Previous research discussed in Chapter 2 demonstrated that flame rotation can develop in small-scale laboratory enclosures when an external circulating flow is imposed on the flame and rising plume. The circulation may be enforced by the use of a rotating screen [Emmons and Ying, 1966] or induced by buoyant air inflow through appropriately located openings, e.g. [Sato and Yang, 1996]. Large scale fire whirls [Pitts, 1990; Soma and Saito, 1991] have also been reported. However there is a clear gap in spatial scales (see Table 1.1) at which whirling flames have been reported, and the existence and dynamics of *medium* scale whirls within enclosures requires further investigation.

This Chapter outlines a method and experimental apparatus to produce medium-scale fire whirls within an enclosure. The apparatus is designed to study both rotating and non rotating flames in the enclosure, and also non rotating flames in the open space. The setup is also capable of maintaining the fuel surface at a constant level during the burning phase, thus ensuring steady state conditions (for heat exchange rate, air entrainment into the area near the fuel surface etc) are satisfied.

Within this work, three different types of liquid fuels namely heptane, diesel and ethanol were used. During the experiments, fuel mass loss rates (burning rates), plume temperatures, heat fluxes at enclosure walls and flame heights have been recorded. A series of video recordings and still photographs enabled analysis of the

transient behaviour of the flame and identification of distinct stages of its development. This part of the work has been supported by Greater Manchester Fire and Rescue Service¹ who provided and funded the experimental facilities.

3.2. The experimental equipment

The experimental equipment includes the enclosure, the fuel supply system, temperature and heat flux sensors, data acquisition and visualisation devices.

3.2.1. Description of the enclosure

The fire whirls were produced in a stand-alone former shipping container as shown in Fig 3.1.

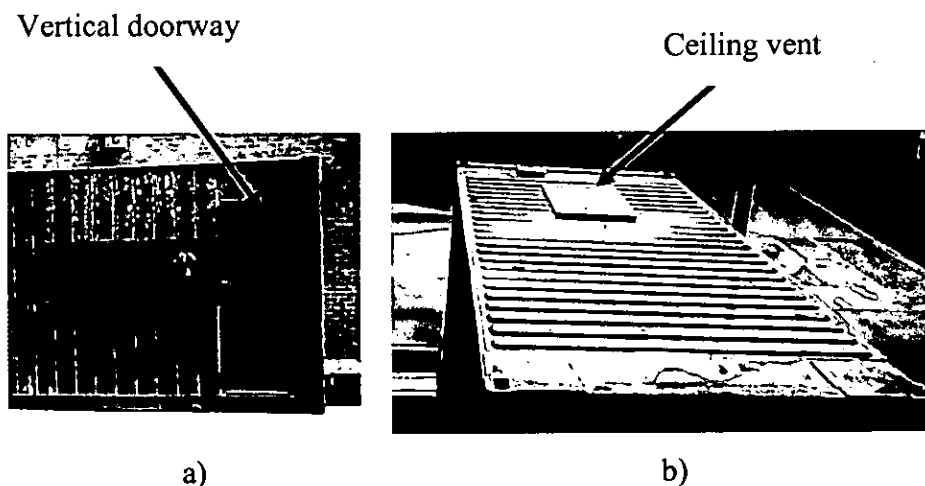


Fig 3.1. The experimental enclosure: a) front view: b) top view.

The container comprises of two compartments, but in Fig 3.1 a) only the right hand compartment (viewed from the side) is shown; this being the compartment in which the fire whirls were produced. To the left not shown in Fig 3 a) is a control room not used in this work. The compartment is constructed of 5 mm thick corrugated steel

¹ www.manchesterfire.gov.uk Greater Manchester Fire and Rescue Service, Training Centre, Cassidy Close, Manchester, UK.

with a hardwood floor. A schematic view and dimensions of the compartment are shown in Fig.3.2. The compartment measurements are 2.77 m (front wall), 2.4 m (side wall) and 2.29 m (high). There is a doorway at the front wall having dimensions of 0.8 m width and 1.95 m height with its jamb at a distance of 0.135 m from the side wall. A ceiling vent measuring 0.8 x 0.9 m (longer side is along the front wall) is located centrally in the enclosure ceiling.

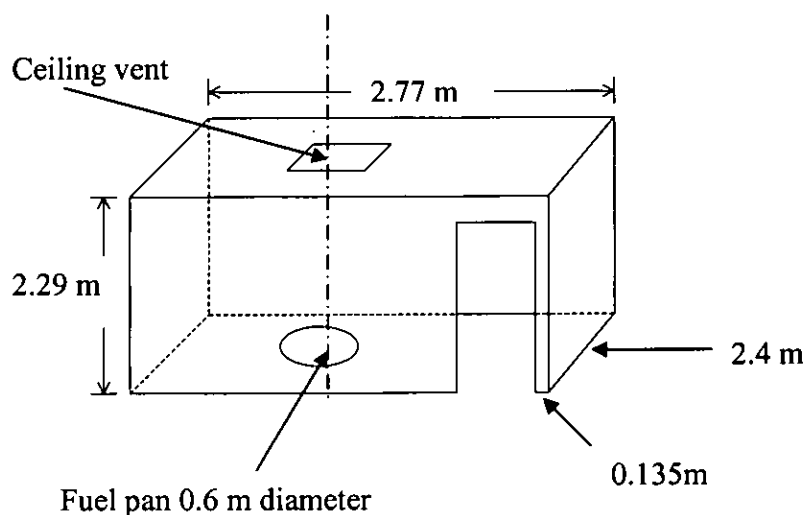


Fig. 3.2. Schematic and dimensions of the enclosure.

The diameter of the fuel pan is 0.6 m, and the pan lip height is 0.3 m above the base of the fuel pan (see Section 3.2.2 for more details). The pan is located centrally, i.e. directly underneath the vent opening.

3.2.2. Fuel system

The fuel system comprises fuel pan, fuel supply pipe, reference container, supply container and control valve, these parts being installed on an adjustable stand. The supply pipe leading from the base of the reference container passes through the wall of the enclosure and is connected directly to the base of the fuel pan. The fuel supply system is shown in Fig 3.3.

The fuel pan was filled with fuel to within a level of 50 to 100 mm of the burner lip and the reference container and supply pipe was filled to the same level from the pan. The system was then allowed to equalise levels in the pan and reference

container before the ignition of the fuel surface. A datum line was established within the reference container and the fuel within the pan was ignited using an industrial pilot burner. The level of the fuel within the reference container was maintained at a constant level by allowing a controlled amount of fuel to flow from the supply container via the control valve. When steady state conditions were established within the compartment, the flow of the fuel from the supply container was at a constant rate equalling the mass lost rate from the fuel surface. After this steady state phase was established, and a record made of the time taken for a set volume of fuel (3 litres) to be burnt, this being the time to lose an equivalent amount from the supply container. This procedure was repeated three times for each fuel and the consistent values obtained are presented within this work. Before measurements were undertaken time was allowed for the compartment temperature and mass loss rate to reach a steady state within the enclosure. When this was achieved then the measurements were taken. The same experimental procedure was undertaken for fires in an open space and within the enclosure.

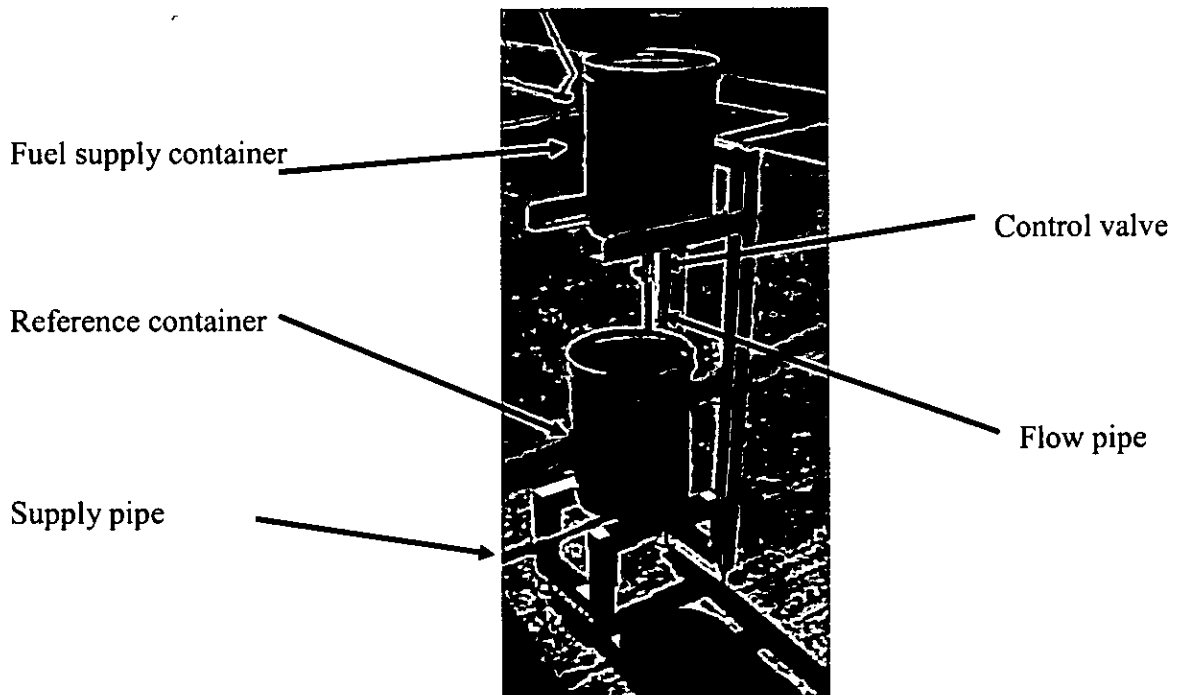


Fig 3.3. Fuel supply system.

The fuel pan (Fig. 3.4) has a diameter of 0.6 m and a height of 0.30 m, the construction is of 2.0 mm thick mild steel giving a maximum fuel capacity of 178

litres when full. The base of the fuel pan is raised from the floor by means of a metal skirt of 0.05 m in height thus allowing the fuel supply pipe to be attached centrally at the base of the pan. These arrangements were chosen for both safety reasons and also that the cooler inflowing fuel would not directly cool the fuel surface. The skirt fully covers the curtain area at the base of the pan, so preventing airflow under the burner. In order that heat transfer between the surrounding atmosphere and the fuel pan is minimised, the fuel pan is insulated with approximately 4 mm of fibreglass matting. To measure fuel temperature a type K thermocouple with a 0.25 mm tip is installed about 5 mm below the fuel surface.

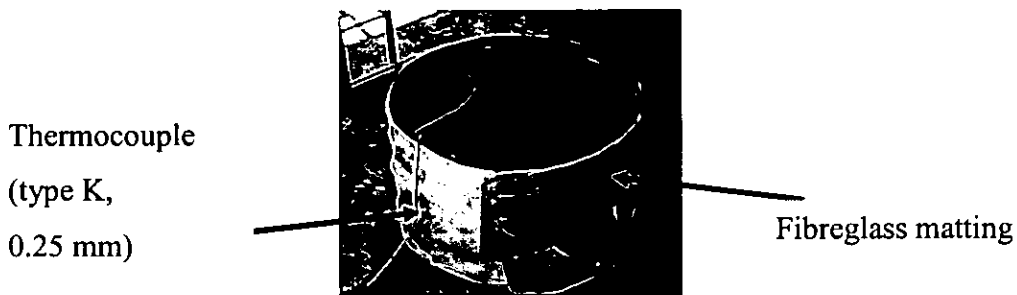


Fig 3.4. Insulated fuel pan.

The surface of the fuel is ignited using an industrial burner. The burner flame provided sufficiently quick (5 to 10 s) heating up the liquid and initiation of self-sustained burning. The ignition process was followed by flame development which was recorded by video camera. In all the experiments the fire was allowed a rise time such that the mass of fuel leaving the fuel surface is equal to the amount of fuel entering the reference container in the majority of the test. The spread of flame across the fuel surface is not considered in this work, since this stage is relatively short.

3.2.3 Description of the fuels

In the design stage of the apparatus, commercially available diesel fuel was used to produce medium scale fire whirls [Marsden, 2000].

Table 3.1. Physical properties of the fuels used

Fuel	Physical properties of the fuels						
	Density (liquid) ^a , kg/m ³	Boiling point ^a , K	Flash point, K	Net heat of combustion ^a , MJ/kg	Heat of vaporisation at boiling point ^a , kJ/kg	Mass burning rate of large spillages ^b , kg/(m ² ·s) D=0.6m	Soot efficiency, kg soot/kg fuel carbon ^c
Ethanol <i>C₂H₅OH</i>	789	352	286	26.8	837	0.015	0-0.019
Diesel ^d <i>C₁₄H₃₀</i>	825	523	385	44.1	291	0.039	0.07
Heptane <i>C₇H₁₆</i>	688	371	270	44.4	365	0.058	0.01-0.044

^a See Table C1 in SFPE Handbook of Fire Protection Engineering, 3rd Ed., NFPA, 2002.

^b See [Babrauskas, 1983] eqn 2.6

^c See [Tewarson Table 3-4.14, SFPE Handbook of Fire Protection Engineering, 3rd Ed., NFPA, 2002; Koylu and Faeth, 1991; Newman, 1994; Bard and Pagni, 1986; Bard and Pagni, 1981]

^d Data for kerosene are used

3. Experimental studies of whirling flames

Subsequently three different fuels (diesel, heptane, and ethanol) were used in these studies and the physical properties of the fuels used are summarised in Table 3.1. These fuels were selected because, as shown in Table 2.1, they exhibit significantly different burning rates and heat release rates when burnt in still air. This will allow an investigation to be conducted, concentrating on the effect of the heat release rate (“fire size”) on the formation and dynamics of whirling flames. Soot production rate and, accordingly radiative fraction, in flames originated by these fuels are also known to be considerably different. This will affect the radiative output from the flames studied and the measurement data obtained will be used to validate the CFD model used.

3.2.4. Temperature measurement

Four thermocouples (type K, 0.25 mm exposed junction) supplied by Omega Electronics were used to measure the plume temperatures. The finest tip size that can be practically used is 0.25 mm which provides a temperature measurement error in the order of $\pm 0.2\%$ as estimated in the work [Brohez et al, 2004] for similar experimental conditions. The use of this type of thermocouple will allow temperatures of up to 1140K to be recorded. The estimated time constant is of the order of 1 s [Snegirev 2004] for this type of thermocouple. An estimated time constant for a 3mm diameter sheathed type K thermocouple in a compartment fire has also been previously published [Yau 2001] being in the order of 10 seconds. The thermocouples have been assembled in the form of a thermocouple tree that is portable within the enclosure. The thermocouples were positioned at the symmetry axis of the fuel pan, at elevations of 0.57, 1.27, and 2.29 m (the latter is in cross-section of the exhaust ceiling vent) above the floor level.

3.2.5. Heat flux measurement

To record heat flux values at the enclosure wall surfaces, two thin film heat flux sensors (HFS-3, Omega Electronics) were installed at locations as shown in Fig. 3.5 and Fig. 3.6. The heat flux sensors operate as self-generating thermopile transducers

3. Experimental studies of whirling flames

and require no special wiring, reference junctions or signal conditioning. The construction of the sensors is of the thin film type which gives the advantage of being easily mounted (Fig. 3.5). The carrier is a polyimide film which is bonded using a Teflon lamination process and has an upper temperature range of 478 K. The sensors were connected to a Squirrel data recorder and the voltage readings taken were converted to W/m^2 using the conversion factor of $0.924 \mu V/(W/m^2)$.

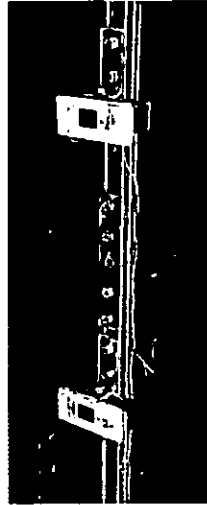


Fig. 3.5. Heat flux sensors (HFS-3, Omega Electronics) installed within the enclosure.

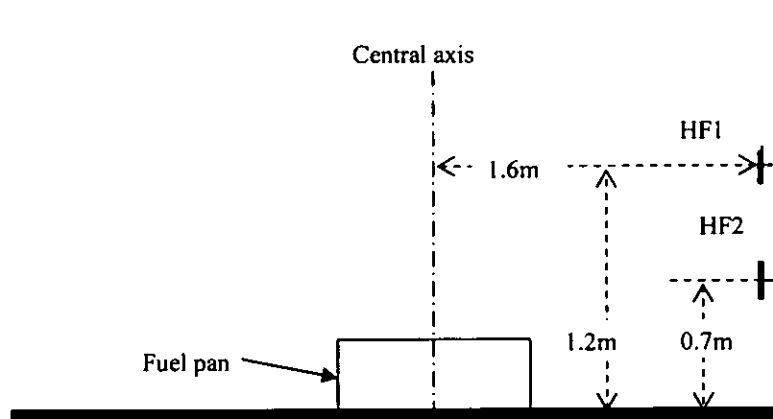


Fig. 3.6. Heat flux sensor positions (HF1, HF2) within the enclosure.

3. Experimental studies of whirling flames

According to the information supplied by the manufacturer, an estimated response time for an HFS-3 sensor is 0.6 s.

3.2.6. Data acquisition

Data from the thermocouples and heat flux sensors were recorded using a Squirrel series 1000 data recorder (Grant Instruments) which has ability to measure up to 125 digital or analogue channels and can store up to 2 million readings. The meter is portable and can be connected to a PC for downloading purposes.

3.2.7. Visualisation techniques

Photo and video recordings were taken during the experiments. A Sony TRV250E digital video camera recorded the flame behaviour in both the enclosure and in the open space. In all cases the camera was tripod mounted and positioned at a distance of about 5m away from the fuel pan.

3.2.8. Experimental arrangements for open flames

The same apparatus and procedure were employed in the case of flames in the open space and in the enclosure. Figure 3.7 illustrates the equipment set up prior to ignition in the open space.

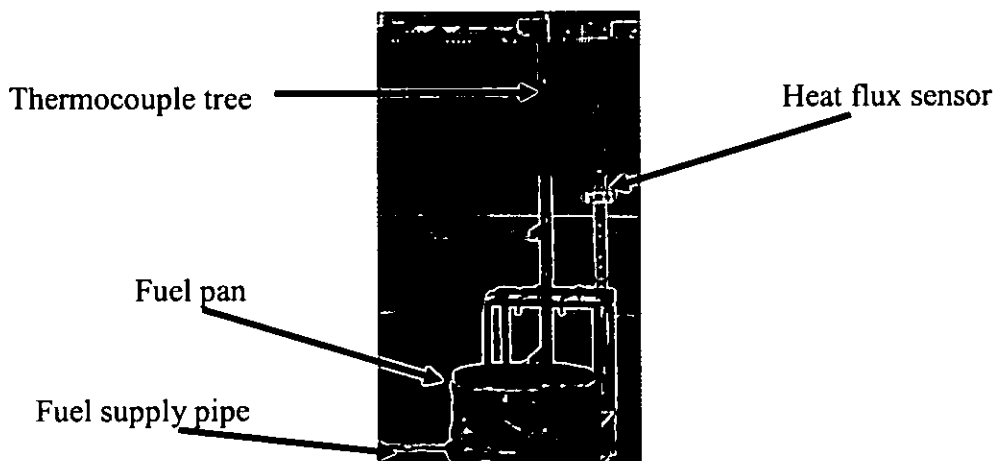


Fig. 3.7. Experimental apparatus for flame in the open space.

3.3. Experimental observations of flames in the open space

A series of initial experiments were undertaken using the apparatus and technique, just described to measure time averaged steady burning rates and flame lengths in the open space. The measurements then were compared with published data [Babrauskas 1983] thereby validating the experimental methodology adopted for this Thesis

Figures 3.8 and 3.9 illustrate flames produced by the experimental apparatus when three different fuels were burnt. It can be clearly seen that the appearance and luminosity of these flames is rather distinct. In accordance with the data in Table 3.1, the ethanol flame produces the least amount of soot. It also exhibits the lowest luminosity level of the fuels used such that the flame is transparent for visual light (Fig. 3.8a, 3.9a). The diesel flame releases the largest amount of soot (Fig. 3.8b, 3.9b), which is also in accordance with data of Table 3.1. The heptane flame is longest of these three (Fig. 3.8c, 3.9c); this is because of the highest heat release rate (see Table 2.1).

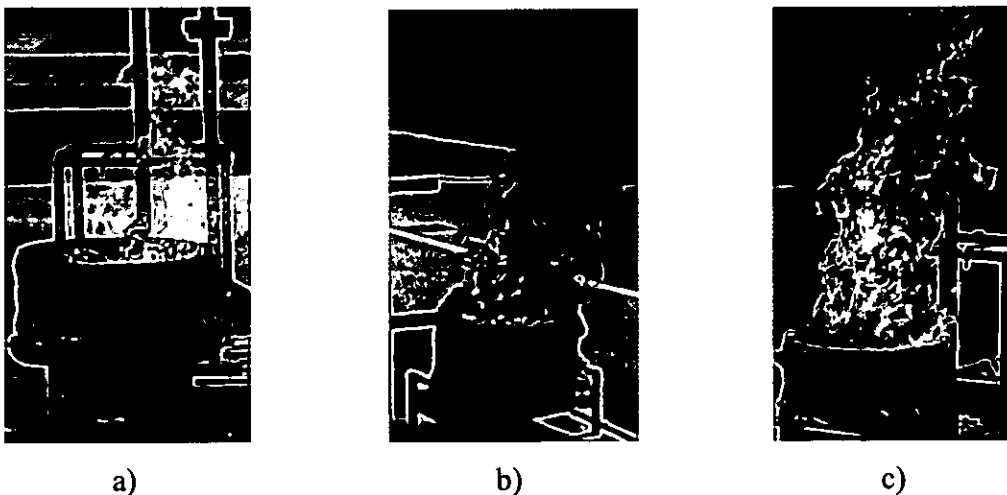


Fig. 3.8. Non-rotating flames in the open space, weak effect of cross wind.

Fuel: a) ethanol; b) diesel; c) heptane.

3. Experimental studies of whirling flames

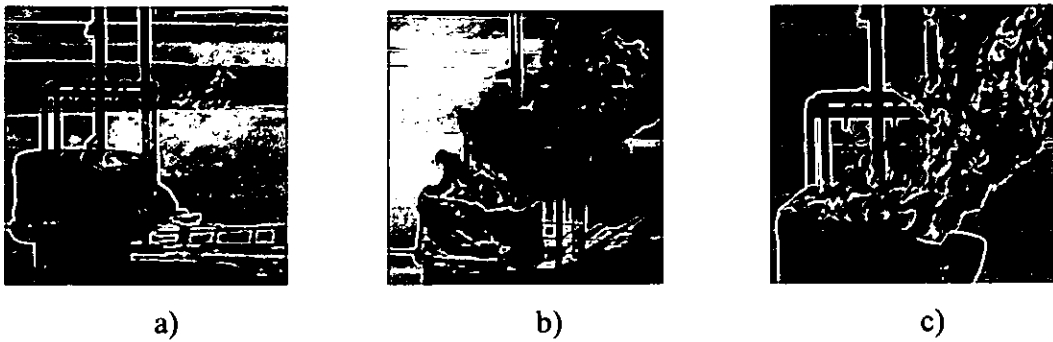


Fig. 3.9. Non-rotating flames in the open space, strong effect of cross wind.

Fuel: a) ethanol; b) diesel; c) heptane.

In the experiments, fuel mass burning rates were measured and average flame heights were determined from the photographs taken. The experimental results are shown in Tables 3.2 to 3.4.

The effects of the cross wind cannot also be overlooked, burning mass loss rates were recorded when in the open still air. However, it must be acknowledged that there will still be slight fluctuations in the circulating air which could in turn affect mass loss rates

Table 3.2. Characteristics of flames in the open space

Fuel	Burning rate, \dot{m}_{fuel} , kg/(m ² ·s)	Heat release rate, \dot{Q} , kW	\dot{Q}^* , Eq. (2.2)	Fr, Eq. (2.1)
Ethanol	0.018	136	0.43	$5.73 \cdot 10^{-6}$
Diesel	0.027	337	1.07	$1.73 \cdot 10^{-5}$
Heptane	0.040	502	1.60	$2.58 \cdot 10^{-5}$

Tables 3.3 and 3.4 present the experimental results obtained by the experimental apparatus designed and built by the author. A comparison of the fuel mass loss rate with published data (see Chapter 2) shows that there is a small discrepancy between the published and experimentally obtained values.

Table 3.3. Comparison of burning rates in the open space

Fuel	Burning rates, \dot{m}_{fuel} , kg/(m ² ·s)	
	Measured in this work	Literature data ¹
Ethanol	0.018	0.014-0.016
Diesel	0.027	0.028-0.038
Heptane	0.040	0.034-0.060

Table 3.4. Comparison of flame lengths in the open space

Fuel	Flame length, L_f , m	
	Measured in this work	Eq. (2.5) ²
Ethanol	1.0	1.1
Diesel	1.5	1.8
Heptane	2.3	2.2

Possible reasons for these small differences could be explained by different freeboard heights and the effects of crosswinds. The differences in respect to flame length show good agreement with equation 2.5. Comparison of the results obtained using this experimental apparatus to published data is of prime importance if accurate mass loss rates in respect to whirling flames are to be obtained. The results when compared to published data show good agreement with the published data in Table 3.3

¹ Data from [Babrauskas, 1983] as presented in Table 2.1.

² Heat release rate is calculated for measurement data, Table 3.2.

3.4. Experimental observations of whirling fires in the enclosure

3.4.1. Flame formation and the behaviour of smoke layer

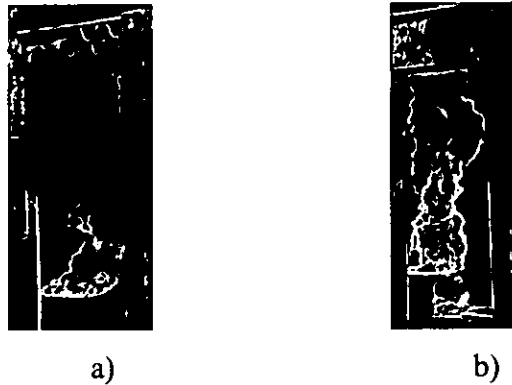


Fig 3.10. Formation of the smoke layer within the enclosure: a) smoke layer in the absence of rotation; b) the absence of the smoke layer during flame rotation in the case of all three fuels.

Shortly after ignition by the pilot burner the whole of the fuel surface became involved and a typical turbulent diffusion flame was established above the fuel pan. A smoke layer formed within the enclosure, which was approximately 1 meter deep when measured from the ceiling (Fig 3.10 a). After the diffusion flame had become established the incoming airflow through the door way began to have an effect upon the flame behaviour such that the flame began to tilt to the rear left of the enclosure (see Fig 3.11).

The flame then began to rotate around the fuel pan and a fully established rotating flame was observed within the enclosure (Fig 3.10 b), the flame lengthening was such that it was visible above the vent opening and during this phase the smoke layer was clearly absent. During this rotation phase the inflowing air through the door way had sufficient force to cause the rotating flame to collapse and a diffusion flame to re-establish above the fuel pan, the cycle then repeated itself, this action is further discussed in 3.4.2.

Rotation of the flame is caused by vorticity being induced within the compartment by means of inflowing air, the vorticity has caused a significant effect upon the flame such that the resultant vortex tube formed by the hot rising plume is stretched resulting in flame lengthening. The increasing airflow through the enclosure is such that it has sufficient force to displace the vortex tube from the buoyant rising plume and this action causes the vortex tube to collapse resulting in flame shortening and the establishment of a diffusion flame.

For the different fuels used in this work different times were recorded in respect to the length of the cycle of the formation and destruction of the rotating plume and it was observed that in the case of heptane and diesel that the cycle was significantly shorter when compared to that of ethanol. This cyclic nature exhibited is further discussed in Chapter 6 in which numerical simulations of this behaviour are compared to the experimental results.

In respect to the formation of the rotating plume within the enclosure two conditions are necessary to ensure that rotation of the flame will occur. Firstly vorticity must be generated within the enclosure and secondly the buoyancy of the hot gases in the rising plume must further amplify the vorticity generated resulting in subsequent flame lengthening.

3.4.2. Periodicity of flame rotation.

When the flame and plume began to rotate, the flame was significantly lengthened, such that it was visible through the ceiling vent. After a short while the rotating flame became unsteady and then collapsed; and then it behaved as an ordinary free-standing pool fire tilted by incoming airflow. This cycle then repeated itself and a rotating flame was again established. Consequent stages of this oscillating process extracted from video recordings are presented in Fig. 3.11.

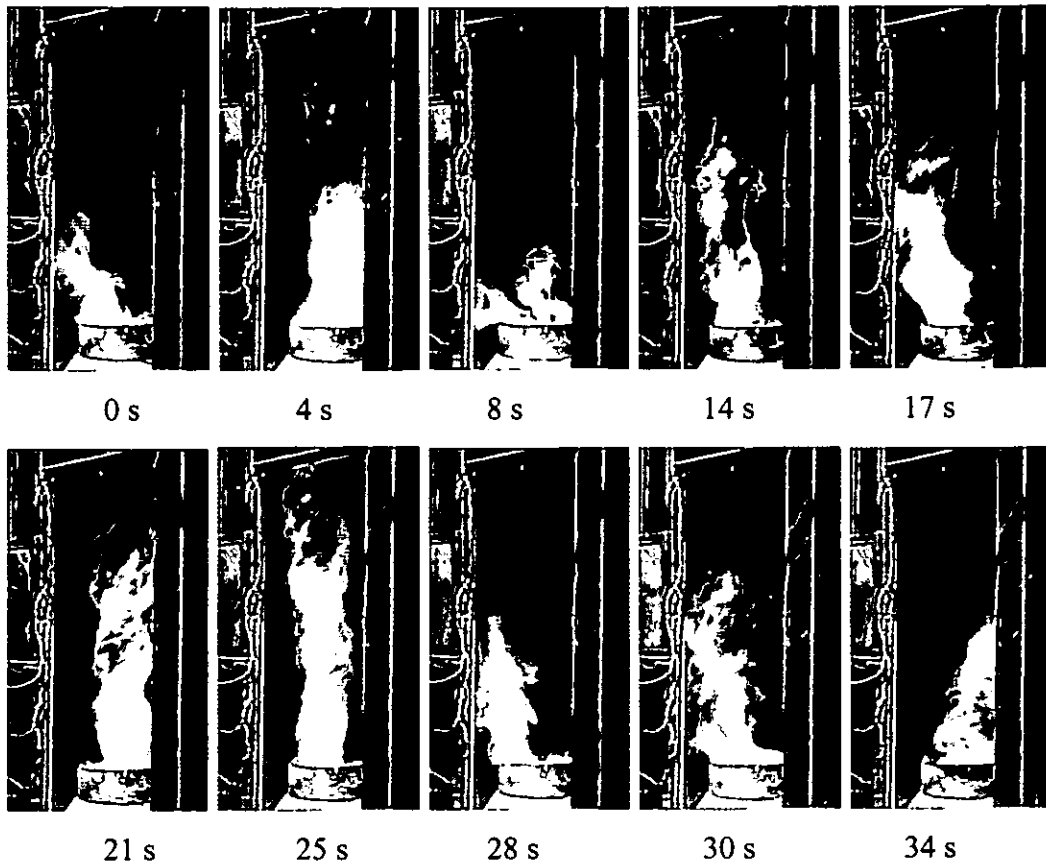


Fig. 3.11. Experimentally observed temporal evolution of whirling flame (fuel is diesel). Conventional time is set to zero for the first frame. Fully developed whirling flames occur at time moments of 4, 14, 24 and 34 s.

It can be seen that along with the rotation of flame around its vertical axis (clearly visible at time instants 4, 14, 25 sec), the flame axis itself travels around the enclosure keeping its base at the fuel source (for example, the axis is tilted towards left wall at time instants 0, 8, 17, 28 sec and towards the right wall at 34 sec). It is therefore concluded that *flame precession*, with some degree of periodicity in the formation and destruction of the whirling column, occurs. This instability and quasi-periodicity was found to be inherent to the enclosed whirling flame.

The flame behaviour was observed to be sensitive to the effects of external winds and as such repeatability was only achieved in still conditions. The experiments were conducted over a period of three days in which the wind conditions were negligible

when measured with an anemometer. Despite this, it is possible to estimate from video frames the characteristic period as 20-30s, 10-15s, and 5-7 seconds for ethanol, diesel, and heptane respectively in no wind conditions.

3.4.3. Fuel mass burning rates and flame length

Table 3.5 presents the experimental data obtained for the range of fuels used in this work. A significant increase in burning rates (110% for ethanol, 44% for diesel, and 80% for heptane) has been observed for whirling flames in the enclosure, when compared to those in the open space. A qualitatively similar observation was earlier reported in smaller size whirling flames over combustible liquids (e.g., mass burning rate of liquid acetone was reported to increase by a factor of 5 when the whirling flame was induced by rotating screen in [Emmons and Ying, 1966]).

The reason for enhanced burning rates has to be fully explained. A possible explanation is that the flow rotation enhances air entrainment into the fuel rich region near the fuel surface, which intensifies mixing of the reactants in this area, thus providing greater reaction rates, temperature, radiation emission, and consequently the increased evaporation rate.

In an enclosure, it can also be suggested that re-radiation from the hot smoke layer and the heated enclosure walls may result in additional heating of the fuel, thereby increasing the evaporation rate from the fuel surface. However, this might not be so in the case of rotating flames where firstly the absence of the smoke layer will reduce radiative effects and second, the effect of wall re-radiation can be estimated. Second, the effect of wall re-radiation can be estimated from additional trials carried out, in which air flow incoming through the doorway was directed such that rotation did not occur. The measured burning rate was found to be similar to that in open space, which indicates that wall re-radiation did not significantly affect the fuel mass burning rate. Therefore, the primary mechanism for the fuel burning rate to increase is most likely to be related to the intensification of fuel vapour/air mixing near the fuel surface, as discussed above.

Table 3.5. Measurements results: open non-whirling and enclosed whirling flames

Fuel	ΔH_C , MJ/kg	Regime							
		Open non-whirling			Enclosed whirling				
		\dot{m}_{fuel} , kg/(m ² ·s)	L_{flame} m	\dot{Q} , kW	\dot{m}_{fuel} , kg/(m ² ·s)	L_{flame} m	\dot{Q} , kW	Increase, Burning rate %	Characteristic period, s
Ethanol	26.8	0.018	1.0	136	0.038	2.2	288	110	20-30
Diesel	44.1	0.027	1.5	337	0.039	2.7	486	44	10-15
Heptane	44.4	0.040	2.3	502	0.072	3.0	904	80	5-7

Table 3.5 presents some of the measurements obtained from the experimental results. It can be seen that although the mass burning rates were found to be similar for ethanol and diesel whirling flames, this being due to the significant difference in heat of combustion, ΔH_C , the heat release rates are still different and correlate with considerably different characteristic periods. Similar effect will be demonstrated by the numerical simulations undertaken as discussed in Chapter 5¹.

The fire size \dot{Q} has an affect upon the characteristic period, at a larger fire size (such as measured in heptane fuel) the cycle appears to be very short when compared to the smaller fire size for the same diameter burner in the case of ethanol. For all the fuels, much *longer* whirling flames have been observed compared to non-whirling ones that were seen in the open space (see Fig. 3.12 and compare to Fig. 3.8 and flame length data in Table 3.4). Several reasons contributed to this. First, fuel mass burning rates and therefore total heat release rates increase in whirling flames (flame length is known to correlate with \dot{Q} , see Eq. (2.5)).

Second as discussed in the literature review (Section 2.4.2.2), flow rotation is known to decrease turbulence within the rising core, thus reducing turbulent mixing at the core boundary and the air entrainment through it. That requires a greater flame surface to develop for the same degree of combustion resulting in a longer flame. This phenomenon was demonstrated in the experiments of [Chigier et al, 1970], [Beer et al, 1971] and [Beer and Chigier, 1972], in which jet flames with a controlled fuel supply rate (burner fires) were studied. These jet flames were subject to external circulation being imparted by the action of rotating screens. Third, the buoyancy induced stretching of the vortex tube in the rotating flow also makes the whirling flame narrower and therefore (to maintain the flame surface area) longer.

¹ In fact, correlation of the characteristic period and total heat release rate was established in numerical simulations *before* the experiments with different fuels were carried out. The increase in process frequency with the fuel supply rate (computations were performed assuming the same type of fuel) first predicted numerically has been later qualitatively confirmed by the experiments, thereby indicating credibility of the model.

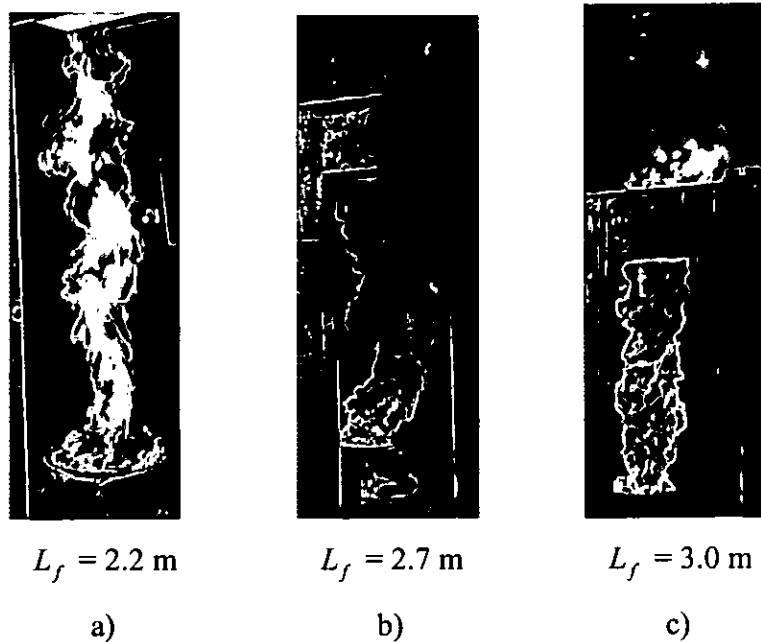


Fig 3.12. Whirling flames within the enclosure and the estimated flame lengths. Fuel: a) ethanol, b) diesel, c) heptane.

As a result of greater mass burning rates and flame lengths, higher plume temperatures and wall heat fluxes were recorded as shown in the next Section.

3.4.4. Temperature and heat flux measurements

Temperature variations with time, as recorded by a thermocouple located on the vertical symmetry axis of the fuel pan, at an elevation of 0.57 m above the floor, are presented in Figs 3.13 and 3.14 for ethanol and heptane respectively. It can be seen that temperature evolution measured in the enclosure differs from that in the open space in that it is generally lower and exhibits a much greater magnitude of variation. The latter can be explained by the fact that in the enclosure, dissimilar to that in the open space, the entire flame is unsteady (as described in Section 3.4.1). The whirling core develops and destroys in a quasi-periodic manner, and the flame oscillates, travelling around the enclosure. Therefore, thermocouple junctions are not always positioned inside the high-temperature flame zone, as it occurs in free-standing flame in still air. Large oscillations of the entire flame result in large fluctuations of a similar frequency to the period formation and destruction (Fig. 3.13b and 3.14b).

3. Experimental studies of whirling flames

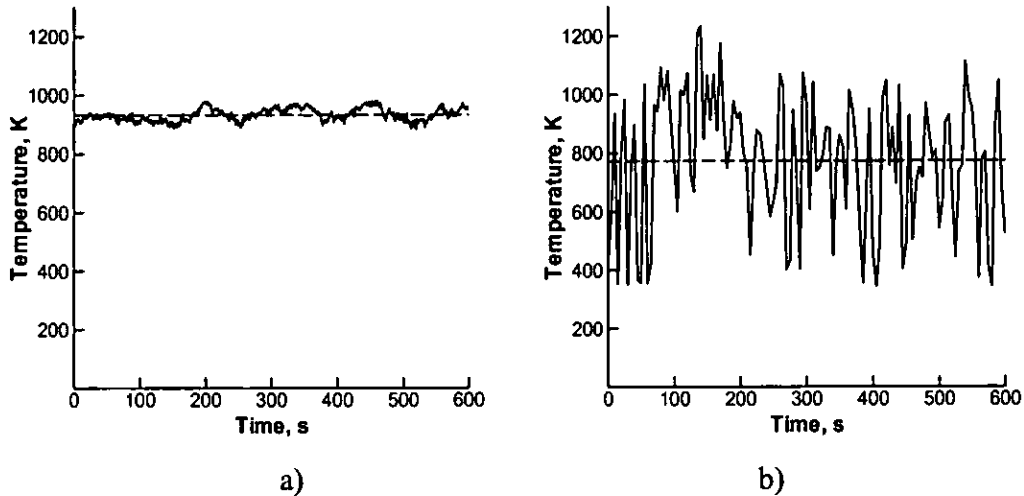


Fig 3.13. Temperature evolution in time for an ethanol flame (thermocouple at the elevation of 0.57 m above the floor level: a) free-standing flame in the open space; b) whirling flame in the enclosure. Dashed line – time-averaged value.

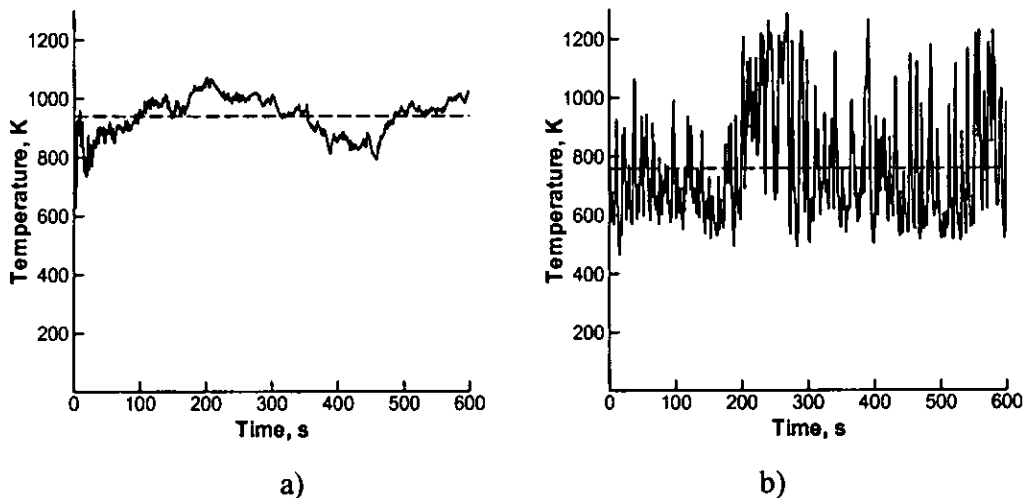


Fig 3.14. Temperature evolution in time for a heptane flame (thermocouple at the elevation of 0.57 m above the floor level: a) free-standing flame in the open space; b) whirling flame in the enclosure. Dashed line – time-averaged value.

It can also be seen that the frequency of the oscillations is greater for the heptane flame when compared to that of the ethanol flame. This is consistent with the above observations in that the characteristic period of the process decreases with the heat release rate. Time-averaged temperatures measured at different locations within the vertical symmetric axis of the fuel pan are presented in Table 3.6.

**Table 3.6. Time-averaged temperatures at different locations
(vertical symmetry axis of the fuel pan)**

Fuel	Elevation of thermocouple above the floor level					
	2.35 m		1.1 m		0.57 m	
	Open	Enclosed	Open	Enclosed	Open	Enclosed
Ethanol	349	683	401	766	921	790
Diesel	326	547	598	715	1027	973
Heptane	321	379	368	521	935	770

Although the time-averaged temperature measured in the enclosure may be less than that in the open space (for example, see Fig. 3.13 and 3.14), maximum temperatures in an enclosed flame can be greater, with greater radiant emission from whirling flames and, accordingly, greater radiative impact onto surrounding structures.

Radiant heat fluxes were measured in the enclosure, as described in Section 3.2.5. and the measurements for ethanol and heptane flames are shown in Fig. 3.15a and 3.15b respectively.

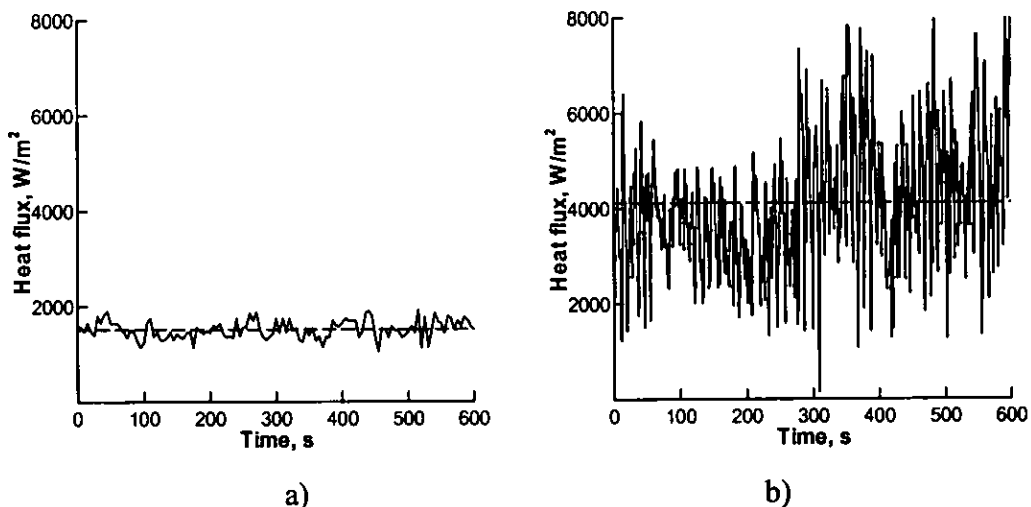


**Fig. 3.15. Dependence of radiative heat flux on time recorded by heat flux sensor HF1:
a) ethanol flame; b) heptane flame.**

Clearly, (despite the time-average temperatures for the two fuels being similar, see Fig. 3.14b and 3.15b) the heptane flame produces a considerably higher heat flux, fluctuating with much greater magnitude. The reasons are: (i) greater fuel mass burning rate and, therefore, total heat release rate, and (ii) greater amount of soot produced, which is an important contributor to the radiant emission from flame. Table 3.7 presents the time-averaged heat flux measurements by two heat flux sensors for the three fuels studied.

Table 3.7. Time-averaged heat fluxes at the enclosure wall

Fuel	HF1, kW/m ²	HF2, kW/m ²
Ethanol	1.7	1.8
Diesel	2.6	3.1
Heptane	4.1	5.0

These data will be used in Chapter 5 for validation of the numerical studies undertaken with CFD model used.

3.5. Conclusions

A medium-scale (according to Table 1.1) experimental apparatus has been constructed to produce fire whirls that are generated when an asymmetrically incoming airflow imposes circulation onto a flame above the fuel pan (located in the centre of the enclosure beneath the ceiling vent). Circulation appeared to be necessary for the whirling flame to develop. Arrangement of the openings within the enclosure provide the conditions necessary for a rotating flame to occur. These openings included an asymmetrically located vertical doorway at the front wall, and centrally located ceiling vent.

3. Experimental studies of whirling flames

Although the aim of this work is to study whirling flames, free-standing non-whirling flames were also produced above the same fuel source, and corresponding fuel mass burning rates, as well as temperatures at three points of the flame axis have been recorded. Measured burning rates and flame heights have been compared to the data published in literature. Fair agreement with the previously published data has been obtained, which demonstrates suitability of the experimental methodology in measurements of the required parameters for whirling flames.

Observations of whirling flames in the experimental enclosure have then been made, for three liquid fuels (with considerably different mass burning rates, when burned in the open). Key characteristics (burning rates, temperatures and heat fluxes) have been compared to those in non-whirling flames produced with the same fuel source.

The observations revealed remarkable and distinctive features of whirling flames as summarised below.

1. Whirling flames exhibited much greater burning rates (40 to 110%, depending on fuel type) than their non-whirling counterparts.
2. Whirling flames were always unstable due to the precessing nature and susceptibility to wind. Whirling flames were part of a quasi-periodic process of flame precession accompanied with formation and destruction of a whirling column. Whirling flames produced large temperature fluctuations.
3. The characteristic period of the process depends on the fuel burnt. It has been found that the period decreases as the total heat release rate increases.
4. Whirling flames were thinner and much longer than non-whirling ones.
5. Whirling flames in the enclosure produced greater radiative heat fluxes than non-whirling ones in the open space (although the fuel source was the same).
6. During the existence of a whirling flame, the upper smoke layer was completely expelled through the ceiling vent.

Clearly, the understanding of this phenomenon requires theoretical analysis and numerical simulations, which are provided in the next sections of this work.

CHAPTER 4.

BASIC THEORETICAL CONCEPTS OF ROTATING FLOWS

4.1. Introduction

This Chapter presents the major characteristics of differing classes of rotating flows, it also outlines basic concepts of the existing theory. As a result, the necessary conditions for buoyant rotating flow to develop are formulated and discussed.

4.2. Characteristics of rotating flows

A fluid flow rotating about the symmetric axis can be considered in cylindrical polar coordinates (r, θ, z) with corresponding radial, angular (azimuthal, swirl) and axial velocity components (v_r, v_θ, v_z) . The flow rotation is characterised by the following kinematic quantities [Batchelor, 1967]: being the vorticity vector,

$$\vec{\omega} = \nabla \times \vec{V} = \left(\frac{1}{r} \frac{\partial v_z}{\partial \theta} - \frac{\partial v_\theta}{\partial z}, \frac{\partial v_r}{\partial z} - \frac{\partial v_z}{\partial r}, \frac{1}{r} \left(\frac{\partial r v_\theta}{\partial r} - \frac{\partial v_r}{\partial \theta} \right) \right), \quad (4.1)$$

the angular frequency of rotation of a fluid particle about the axis,

$$\Omega = \frac{v_\theta}{r}, \quad (4.2)$$

and the circulation along a concentric path l ,

$$\Gamma = \oint_l \vec{V} d\vec{l}, \quad (4.3)$$

where $d\vec{l}$ is the infinitesimal directed segment along the path l .

4.3. Classification of simple rotating flows

To classify different types of rotating flows, consider an axisymmetric flow with no radial and axial velocity components. Within such a flow, the angular velocity, v_θ , is the only non-zero velocity component, and it depends on radius r . The vorticity vector also has only one non-zero (axial) component, ω_z ,

$$\omega_z = \frac{1}{r} \frac{\partial}{\partial r} r v_\theta. \quad (4.4)$$

In the idealised (axisymmetric, steady-state, laminar) flow, the momentum equation,

$$\frac{dp}{dr} = \rho \frac{v_\theta^2}{r}, \quad (4.5)$$

represents balance between the centrifugal force and the pressure force.

Depending on the variation of the angular velocity with radius, three types of axisymmetric rotating flows (Fig. 4.1) are identified [Gupta et al, 1984].

1. Angular velocity linearly increases with radius (Fig. 4.1a),

$$v_\theta = C_1 r, \quad C_1 = \text{const.} \quad (4.6)$$

This type of flow is termed as the *solid body* or *forced vortex*, for which the vorticity, the angular frequency, and the circulation are equal to

$$\omega_z = 2C_1, \quad \Omega = C_1, \quad \Gamma = 2\pi C_1 r^2, \quad (4.7)$$

respectively.

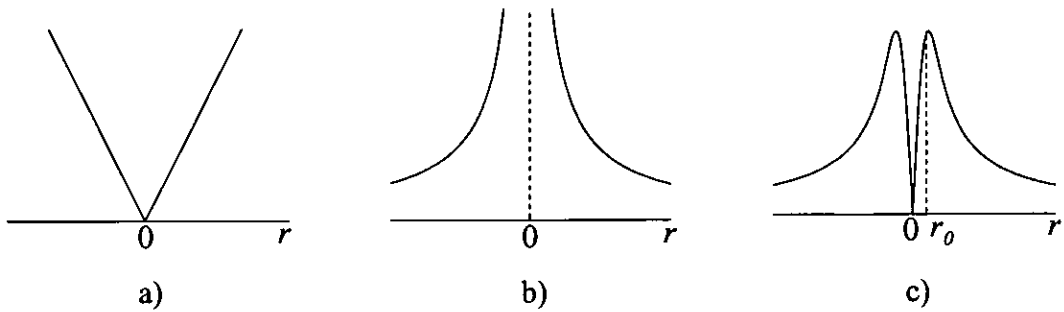


Fig. 4.1. Radial profiles of angular velocity, $v_\theta(r)$: a) forced (solid body) vortex; b) free (potential) vortex; c) combined (Rankine) vortex.

2. Angular velocity decreases with radius (Fig. 4.1b),

$$v_\theta = \frac{C_2}{r}, \quad C_2 = \text{const.} \quad (4.8)$$

This type of flow (called *potential* or *free vortex*) has the following vorticity, angular frequency, and circulation:

$$\omega_z = 0, \quad \Omega = \frac{C_2}{r^2}, \quad \Gamma = 2\pi C_2. \quad (4.9)$$

The *forced vortex* has non-zero constant vorticity and angular frequency, its circulation increases with radius. Alternatively, the vorticity in the *free vortex* is zero (fluid particles follow a circular streamline without rotation about its own axis), its angular velocity and frequency both tends to zero away from the axis, and its circulation is of constant value. It can be shown (see [Batchelor, 1967, p. 203]) that

forced vortex velocity profile (4.6) represents the constant properties fluid flow *inside* a rotating cylinder, while free vortex (4.8) corresponds to the unconfined flow *outside* the cylinder.

These two types of flow are also different in terms of their stability. The fluid particle displacement radially outwards, which is forced by the centrifugal acceleration, is resisted by the pressure gradient (4.5) increasing with radius in the forced vortex and is not compensated by the decreasing pressure gradient in the free vortex. Therefore, fluctuations are stabilised in a forced vortex and destabilised in a free vortex [Sloan et al, 1986].

3. The vortex that combines all these properties is the Rankine vortex, in which the angular velocity increases with radius inside the vortex core and decreases outside it (Fig. 4.1c)¹:

$$v_{\theta} = \frac{C_3}{r} \left(1 - \exp\left(-\frac{r^2}{r_0^2}\right) \right), \quad (4.10)$$

where r_0 is the effective radius of the vortex. The corresponding vorticity, angular frequency, and circulation are

$$\begin{aligned} \omega_z &= \frac{2C_3}{r_0^2} \exp\left(-\frac{r^2}{r_0^2}\right), \\ \Omega &= \frac{C_3}{r^2} \left(1 - \exp\left(-\frac{r^2}{r_0^2}\right) \right), \\ \Gamma &= 2\pi C_3 \left(1 - \exp\left(-\frac{r^2}{r_0^2}\right) \right). \end{aligned} \quad (4.11)$$

For small distances, $r/r_0 \ll 1$, relationships (4.6), (4.7) for solid body rotation recover with $C_1 = C_3/r_0^2$. In the opposite limit, $r/r_0 \gg 1$, the flow parameters coincide with those of a free vortex (4.8), (4.9) with $C_2 = C_3$.

¹ In [Hopfinger and Van Heijst, 1993] the Rankine vortex is defined as combination of (4.6) and (4.8).

Vortexes in rotating fluids are often of the Rankine type. For example, the velocity distribution (4.10) appears as a transient solution of vorticity diffusion away from an initial concentration on a vortex line [Batchelor, 1967, p. 204]. In that case, which is also called Lamb vortex [Hopfinger and Van Heijst, 1993], the radius of the vortex core increases in time as $r_0 = \sqrt{4\nu t}$, where ν is the kinematic viscosity. Another example is cyclonic (sink) vortex [Sanson, 2001]. Also, a Rankine vortex forms in a rising rotating flow which is considered below.

Due to a different response on fluid particle radial displacements, turbulent fluctuations are reduced (stabilised) in the internal (forced) part of the Rankine vortex and they are increased (destabilised) in its external (free vortex) part. This results in the inhibited turbulent mixing and air entrainment into rotating flames, which facilitates flame elongation.

4.4. The vorticity equation & Sources of vorticity

Consider now a general flow with the momentum equation

$$\frac{\partial \bar{\mathbf{V}}}{\partial t} + (\bar{\mathbf{V}} \cdot \nabla) \bar{\mathbf{V}} = -\frac{1}{\rho} \nabla p + \frac{1}{\rho} \nabla \hat{\boldsymbol{\sigma}} + \frac{\rho - \rho_0}{\rho} \bar{\mathbf{g}}, \quad (4.12)$$

Where $\hat{\boldsymbol{\sigma}}$ is the stress tensor which may include turbulent components if time averaged (mean) flow is considered. The evolution of vorticity in the flow is governed by the vorticity equation, which can be derived by taking curl of the momentum equation (4.12)

$$\frac{\partial \bar{\boldsymbol{\omega}}}{\partial t} + (\bar{\mathbf{V}} \cdot \nabla) \bar{\boldsymbol{\omega}} = -\nabla \frac{1}{\rho} \times \nabla p + \nabla \times \left(\frac{1}{\rho} \nabla \hat{\boldsymbol{\sigma}} \right) - \nabla \frac{\rho_0}{\rho} \times \bar{\mathbf{g}} - \bar{\boldsymbol{\omega}} (\nabla \cdot \bar{\mathbf{V}}) + (\bar{\boldsymbol{\omega}} \cdot \nabla) \bar{\mathbf{V}}. \quad (4.13)$$

Analysis of this equation allows the vorticity sources in the flow to be identified. In particular, in the special case of an inviscid fluid of uniform density acted on by a

potential body force, the vorticity of a given fluid particle is conserved. It is however, not the case in buoyant turbulent flames (which are considered in this work). In such a flow the vorticity of a given fluid particle is changed due to the following reasons, each of which corresponds to a particular term in right hand side of Eq. (4.13).

1. Non-buoyant baroclinic vorticity generation caused by misalignment of pressure and density gradients. Note that the corresponding term (also called baroclinic torque), $-\nabla \frac{1}{\rho} \times \nabla p$, vanishes for barotropic fluids, i.e. if $p = p(\rho)$.

2. Viscous (turbulent) dissipation, represented in the vorticity equation (4.13) by $\nabla \times \left(\frac{1}{\rho} \nabla \hat{\sigma} \right)$. This term converts to $\nu \Delta \bar{\omega}$ for constant density, constant viscosity flows.

3. Buoyancy, $-\nabla \frac{\rho_0}{\rho} \times \bar{\mathbf{g}}$. If the acceleration of gravity, $\bar{\mathbf{g}}$, is directed along the axis of rotation z , then it can be shown that the buoyancy term in Eq. (4.13) does not contribute into the axial component of the vorticity vector, i.e. buoyancy has no effect on rotation about vertical axis.

4. Dilatation, $-\bar{\omega}(\nabla \cdot \bar{\mathbf{V}})$, which vanishes in incompressible fluids but affects the vorticity in non-isothermal, variable density flows.

5. Stretching of the vortex tubes. The corresponding stretching term, $(\bar{\omega} \cdot \nabla) \bar{\mathbf{V}}$, in Eq. (4.13) is the most important source of vorticity, which is discussed below in more detail.

The most important term is the last term in which the flows examined within this work concern rotation about the vertical z -axis, (i.e. in horizontal $x-y$ plane), takes place. The stretching term is governed by the induced buoyancy of the hot rising plume from the fuel pan. Therefore in this particular case the analysis can be restricted by consideration of the evolution of z -component of the vorticity vector only. Written in cylindrical coordinates, the corresponding equation takes the form

$$\begin{aligned}
 & \frac{\partial \omega_z}{\partial t} + v_r \frac{\partial \omega_z}{\partial r} + v_\theta \frac{1}{r} \frac{\partial \omega_z}{\partial \theta} + v_z \frac{\partial \omega_z}{\partial z} = \\
 & \quad + \underbrace{\frac{1}{r} \frac{\partial p}{\partial \theta} \frac{\partial}{\partial r} \frac{1}{\rho} - \frac{\partial p}{\partial r} \frac{1}{r} \frac{\partial}{\partial \theta} \frac{1}{\rho}}_{\text{baroclinic torque}} \\
 & \quad + \underbrace{v \left(\frac{1}{r} \frac{\partial}{\partial r} r \frac{\partial \omega_z}{\partial r} + \frac{1}{r^2} \frac{\partial^2 \omega_z}{\partial \theta^2} + \frac{\partial^2 \omega_z}{\partial z^2} \right)}_{\text{viscous dissipation}} \\
 & \quad + 0 \\
 & \quad \underbrace{\hspace{1.5cm}}_{\text{buoyancy}} \\
 & \quad - \underbrace{\omega_z \left(\frac{1}{r} \frac{\partial v_r}{\partial r} + \frac{1}{r} \frac{\partial v_\theta}{\partial \theta} + \frac{\partial v_z}{\partial z} \right)}_{\text{dilatation}} \\
 & \quad + \underbrace{\omega_r \frac{\partial v_z}{\partial r} + \omega_\theta \frac{1}{r} \frac{\partial v_z}{\partial \theta} + \omega_z \frac{\partial v_z}{\partial z}}_{\text{stretching}}, \tag{4.14}
 \end{aligned}$$

where the viscous dissipation term is written for a constant viscosity flow, and ν is the kinematic viscosity. The very last (underlined) summand in the stretching term causes the amplification of non-zero vorticity, ω_z , in a vertically accelerating flow in which $\partial v_z / \partial z > 0$. In a buoyant flame and a plume the buoyancy force causes the vertical acceleration of the flow inside the flame zone. That results in increase of ω_z provided that non-zero background vorticity is introduced. This is the explanation of development of a rotating core within a rising buoyant flow.

The term $\omega_z \partial w / \partial z$ becomes negative in the upper plume where axial velocity decreases with height. In this region the vortex tubes are not stretched but expanded, due to which the vorticity is decreased. Viscous and turbulent dissipation also results in decrease of vorticity, while the baroclinic torque and dilatation may change their sign in the flow.

4.5. Vorticity concentration in axisymmetric flow

A useful example of a simple flow, in which the vorticity is intensified due to stretching of vortex tubes and balanced due to lateral spreading by viscous dissipation, is given in [Batchelor, 1967, p. 272]. The axisymmetric, constant properties flow is considered in which the transport equation (4.14) for ω_z takes the form

$$\begin{aligned} \frac{\partial \omega_z}{\partial t} + v_r \frac{\partial \omega_z}{\partial r} + v_\theta \frac{1}{r} \frac{\partial \omega_z}{\partial \theta} + v_z \frac{\partial \omega_z}{\partial z} = & \\ \underbrace{v \left(\frac{1}{r} \frac{\partial}{\partial r} r \frac{\partial \omega_z}{\partial r} + \frac{1}{r^2} \frac{\partial^2 \omega_z}{\partial \theta^2} + \frac{\partial^2 \omega_z}{\partial z^2} \right)}_{\text{viscous dissipation}} & \\ + \underbrace{\omega_r \frac{\partial v_z}{\partial r} + \omega_\theta \frac{1}{r} \frac{\partial v_z}{\partial \theta} + \omega_z \frac{\partial v_z}{\partial z}}_{\text{stretching}}, & \quad (4.15) \end{aligned}$$

In the region $z \geq 0$, $r \geq 0$, $0 \leq \theta < 2\pi$ a solenoidal velocity field is assumed,

$$v_r = -\frac{C}{2}r, \quad v_\theta = v_\theta(r), \quad v_z = Cz, \quad C = \text{const} > 0, \quad (4.16)$$

representing vertically accelerating rotating flow, which may be considered as a rough approximation of a rising whirling plume. Then Eq. (4.15) has a steady-state solution ω_z , which does not depend on θ and z :

$$\omega_z = \omega_{z \max} \exp\left(-\frac{r^2}{r_0^2}\right), \quad (4.17)$$

where

$$r_0 = \sqrt{\frac{4\nu}{C}}. \quad (4.18)$$

The angular velocity corresponding to (4.17) can be derived from (4.4):

$$v_\theta = \frac{\omega_{z \max} r_0^2}{2r} \left(1 - \exp\left(-\frac{r^2}{r_0^2}\right)\right). \quad (4.19)$$

It can be seen that the flow is in fact the Rankine vortex, Eq. (4.10). In this flow the concentration of vorticity into the vortex core is balanced by viscous dissipation, which results in three-dimensional flow known as the Burgers vortex [Hopfinger and Van Heijst, 1993]. Typical streamlines of the flow are shown in Fig. 4.2.

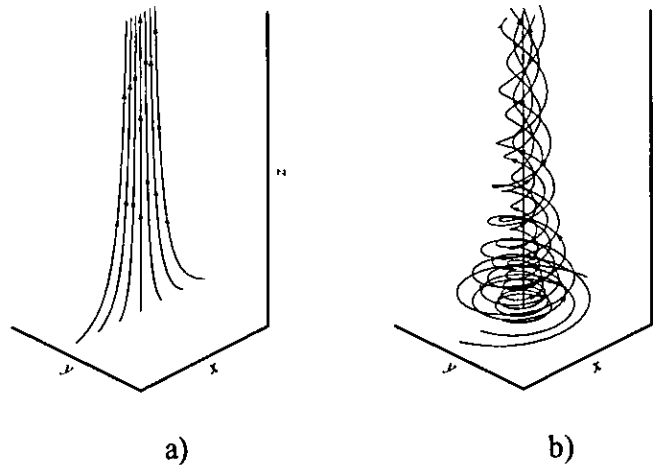


Fig. 4.2. Streamlines of the flow (4.16), (4.19): a) $\omega_{z \max} = 0$, b) $\omega_{z \max} > 0$.

The steady vorticity field (4.17) is the distribution to which transient vorticity, $\omega_z(r, t)$, tends, as $t \rightarrow \infty$, if its initial distribution, $\omega_z(r, 0)$, satisfies the condition

$$0 < \int_0^{\infty} \omega_z(r, 0) 2\pi r dr < \infty. \quad (4.20)$$

It can be shown using Eq. (4.15), that for the considered flow the integral of the vorticity over a horizontal plane is invariant:

$$\frac{d}{dt} \int_0^{\infty} \omega_z(r, t) 2\pi r dr = 0. \quad (4.21)$$

As follows from (4.3) and (4.4), the integral in (4.21) is the circulation,

$$\Gamma_0 = \lim_{r \rightarrow \infty} 2\pi r v_{\theta}(r), \quad (4.22)$$

of the external flow. Therefore, the initial non-zero vorticity (and external circulation Γ_0) must be introduced for a steady rotating flow to develop; a spatial distribution of the initial vorticity may be arbitrary. Due to (4.21), the maximum vorticity $\omega_{z \max}$ in the steady vortex (4.17) is coupled with the external circulation:

$$\omega_{z \max} = \frac{\Gamma_0}{\pi r_0^2}. \quad (4.23)$$

As follows from (4.16) and (4.18), the radius of the vortex core is

$$r_0 = \sqrt{\frac{4\nu}{\partial v_z / \partial z}}, \quad (4.24)$$

and therefore the maximum vorticity and angular velocity are

$$\omega_{z \max} = \frac{\Gamma_0}{\pi} \frac{\partial v_z / \partial z}{4\nu} . \quad (4.25)$$

$$v_{\theta \max} = 0.638 \frac{\Gamma_0}{\pi} \sqrt{\frac{\partial v_z / \partial z}{4\nu}} . \quad (4.26)$$

Thus, the greater is the vertical flow acceleration or the smaller is the viscous dissipation, then the thinner and more intensive is the vortex core. Note, vortex radius (4.24) does not depend on the external circulation Γ_0 .

The overall degree of whirling can be characterised by the swirl number [Gupta et al, 1984],

$$S = \frac{\int_0^\infty v_z v_\theta r^2 dr}{\frac{D}{2} \int_0^\infty v_z^2 r dr} , \quad (4.27)$$

where (for the problem considered) D is the pool/burner diameter. The swirl number presents the ratio of axial fluxes of angular and axial momentum (turbulent components and pressure term are neglected in Eq. (4.27)). It can be demonstrated for the flow considered, that the swirl number is

$$S = \frac{\omega_{z \max} R^2}{4\nu_z R} = \frac{1}{4\pi R \nu_z} \Gamma_0 , \quad (4.28)$$

being proportional to the external circulation: $S \propto \Gamma_0$.

4.6. Dimensionless criteria governing buoyant rotating flow

Dimensional analysis of the vorticity, momentum, and energy equations for a general flow (See Chapter 5) shows the governing role of several dimensionless criteria. These can be formulated based on characteristic length L^* , velocity V^* , density ρ^* , density drop $\Delta\rho^*$, and vorticity ω^* . The Rossby number,

$$Ro = \frac{V^*}{L^* \omega^*}, \quad (4.29)$$

presents the ratio of inertial to centrifugal forces. The Reynolds number

$$Re = \frac{V^* L^*}{\nu}, \quad (4.30)$$

shows the ratio of inertial forces to viscous stresses. The Froude number,

$$Fr = \frac{\rho^* V^{*2}}{\Delta\rho^* g L^*}, \quad (4.31)$$

gives the ratio of fuel flow kinetic energy to buoyancy. Prandtl number, Pr , is equal to the ratio of kinematic viscosity to thermal diffusivity.

$$Pr = \frac{\nu}{\alpha} \quad (4.32)$$

where α is the thermal diffusivity

In buoyant whirling flows, additional dimensionless criteria, which are derived from those given above, are justified. Firstly, since the velocity scale V^* is not given in input data, it therefore is taken as

$$V^* = \sqrt{g L^* \Delta\rho^* / \rho^*}, \quad (4.33)$$

thereby setting the Froude number to unity (i.e. a balance between the deceleration produced by the entrained air flux and acceleration produced by the buoyancy. Thus the velocity more or less remains constant with respect to height). Secondly, instead of the Reynolds number, the Rayleigh number,

$$\text{Ra} = \frac{\text{Re}^2}{\text{Fr}} \text{Pr} = \frac{gL^3}{\nu^2} \frac{\Delta\rho}{\rho} \text{Pr}, \quad (4.34)$$

which does not include the velocity scale, is used to quantify buoyant convection. To take the heat release into account, the modified (flux) Rayleigh number is introduced,

$$\text{Ra}_{flux} = \text{Ra} \frac{\dot{Q}/A_{fuel}}{\rho^* V^* C_p \Delta T^*}, \quad (4.35)$$

where $\dot{Q} = \Delta H_C \dot{m}_f A_{fuel}$ is the total heat release rate (ΔH_C is the heat of combustion, \dot{m}_{fuel} is the fuel mass burning rate, and A_{fuel} is the burning area), C_{p0} is the constant pressure specific heat of the ambient air at temperature T_0 , and $\Delta T^* = T^* - T_0$ is the characteristic temperature drop.

Finally, in rotating flows the Ekman number, Ek , and the Taylor number, Ta , represent the mutual significance of viscous stresses and centrifugal forces:

$$\text{Ek} = 1/\text{ReRo}, \quad \text{Ta} = 1/\text{Ek}^2. \quad (4.36)$$

Among the above dimensionless criteria, the Rossby number is the primary one that determines the whirling of a buoyant flame. The overall degree of whirling can be characterised by the swirl number, Eq. (4.27). The swirl number presents the ratio of axial fluxes of angular and axial momentum (turbulent components are omitted in Eq. (4.27)). In an axisymmetric flow, the swirl number is a function of the above dimensionless parameters and, possibly, of the axial position:

$$\text{S} = \text{S}\left(\text{Ro}, \text{Ra}_{flux}, \text{Ek}, \frac{z}{L^*}\right). \quad (4.37)$$

For example, considering Eq. (4.28) and taking into account relationship (4.23), $\omega_{z\max} = \Gamma_0 / \pi r_0^2$, the swirl number (4.27) can be shown to be inversely proportional to the Rossby number:

$$S = \frac{1}{2\text{Ro}} \frac{L^*}{z}, \quad (4.38)$$

where in definition (4.29) of Rossby number the characteristic value $\omega^* = \Gamma_0 / \pi R^2$ is used for vorticity and vertical velocity is $v_z = Cz = (V^* / L^*) z$.

Note, the characteristic length, L^* , should approximate the distance at which the buoyancy force determines the flow acceleration. The appropriate length scale,

$$L^* = \left(\frac{\dot{Q}}{C_{p0} \rho_0 T_0 \sqrt{g}} \right)^{2/5}, \quad (4.39)$$

is introduced in [Zukoski, 1995].

4.7. Conclusions

The theory of rotating flows reveals two necessary conditions for buoyant rotating flow to develop:

1. non-zero background vorticity (and external circulation) and
2. vertical acceleration of the flow.

The primary mechanism of vorticity concentration in the vortex core is the stretching of the vortex tube in this case by the hot rising plume; the latter is balanced by viscous (and possibly turbulent) dissipation. When the above conditions are satisfied, the steady rotating flow has a radial velocity distribution similar to that of the Rankine vortex; the swirl number of the flow is proportional to the external circulation. The above mechanism is known to work in buoyancy driven flows of a

wide range of spatial scales, from small-scale laboratory flows to very large circulating patterns in oceans and in the atmosphere.

In the internal part of a Rankine-type vortex the turbulent fluctuations associated with a non rotating diffusion flame are reduced by the stretching of the vortex tube, this stretching reduces the turbulent intensity resulting in a reduction of the mixing of the fuel and oxidiser. This reduction of intensity increases the combustion zone and the flame is lengthened by the stretched vortex tube imposed on the buoyant plume.

These results are reproduced by (and used in the interpretation of) the experimental observations (Chapter 3) and numerical simulations (Chapter 6) presented in this work, where the development of whirling buoyant turbulent diffusion flames are studied in the enclosure. The CFD model and code *Fire3D* [Snegirev et al, 2001; Snegirev et al, 2003; Snegirev, 2004; Snegirev et al, 2004] was used. In the model, the above mentioned inhibiting of turbulent mixing intensity has been explicitly taken into account to obtain predictions reproducing elongated rotating flames. The model, the code, and the results of the simulations are discussed below (Chapters 5 and 6).

CHAPTER 5.

MATHEMATICAL MODEL AND CFD CODE

5.1. Introduction

This Chapter describes the mathematical model and the CFD code that has been applied in the numerical simulations of whirling flames. The model used is the modified version of that which was developed in the Centre for Research in Fire and Explosion Studies at the University of Central Lancashire (*Fire3D*) to simulate essentially sub-sonic turbulent multi-component reacting and radiating flows in an open space and in enclosures. The governing equations (expressing conservation of mass, momentum, and energy) and the sub-models for turbulence, combustion, soot formation, and thermal radiation are presented within this chapter. As a part of this work, particular attention is paid to the modification of the turbulence model which is required to allow for the inhibiting effect of centrifugal forces in a rotating flow on turbulent fluctuations. The remaining sub-models are standard in the code *Fire3D* and are discussed within this chapter. A brief description of the numerical implementation and overview of the validation studies undertaken is also provided.

5.2. Governing equations

A RANS (Reynolds Averaged Navier Stokes)-type CFD model is used, in which the continuity, specie conservation, momentum and energy equations are

$$\frac{\partial \rho}{\partial t} + \frac{\partial \rho u_j}{\partial x_j} = 0, \quad (5.1)$$

$$\frac{\partial \rho Y_\alpha}{\partial t} + \frac{\partial \rho u_j Y_\alpha}{\partial x_j} = \frac{\partial}{\partial x_j} \left(\frac{\mu}{Sc} + \frac{\mu_t}{Sc_t} \right) \frac{\partial Y_\alpha}{\partial x_j} + \rho \dot{r}_\alpha, \quad (5.2)$$

$$\frac{\partial \rho u_i}{\partial t} + \frac{\partial \rho u_j u_i}{\partial x_j} = - \frac{\partial p}{\partial x_i} + \frac{\partial \sigma_{ij}}{\partial x_j} + (\rho - \rho_0) g_i, \quad i = 1, 2, 3, \quad (5.3)$$

$$\frac{\partial \rho h}{\partial t} + \frac{\partial \rho u_j h}{\partial x_j} = \frac{\partial}{\partial x_j} \left(\frac{\mu}{Pr} + \frac{\mu_t}{Pr_t} \right) \frac{\partial h}{\partial x_j} + \frac{\partial q_{ij}}{\partial x_j}, \quad (5.4)$$

where \dot{r}_α is the production rate of the α -component of the mixture, p is the dynamic pressure (equal to difference between the total pressure P and the hydrostatic pressure in still air with density ρ_0), σ_{ij} is the stress tensor,

$$\sigma_{ij} = (\mu + \mu_t) \left(\frac{\partial u_i}{\partial x_j} + \frac{\partial u_j}{\partial x_i} \right) - \frac{2}{3} \delta_{ij} \left(\rho k + (\mu + \mu_t) \frac{\partial u_k}{\partial x_k} \right), \quad (5.5)$$

h is the enthalpy of the mixture,

$$h = \sum_\alpha Y_\alpha \left(\Delta h_{f\alpha}^0 + \int_{T^0}^T C_{p\alpha}(T) dT \right), \quad (5.6)$$

and $\alpha = fuel, O_2, CO_2, H_2O, N_2, CO, C$. Low Mach number flow at constant atmospheric pressure, P , is assumed. Density is obtained from the state equation,

$$P = R \rho T \sum_{\alpha=C} \frac{Y_\alpha}{W_\alpha}, \quad (5.7)$$

for the ideal gas mixture. In the above turbulent flow equations, Favre-averaged mean values of parameters are assumed, wherever appropriate (with no overbars shown).

5.3. Turbulence modelling & the effect of flow rotation

The buoyancy-modified $k - \varepsilon$ turbulence model is used in this CFD model. In transport equations for turbulent kinetic energy k and its dissipation rate ε ,

$$\frac{\partial \rho k}{\partial t} + \frac{\partial \rho u_j k}{\partial x_j} = \frac{\partial}{\partial x_j} \left(\mu + \frac{\mu_t}{\sigma_k} \right) \frac{\partial k}{\partial x_j} + \rho(G + G_B) - \rho\varepsilon, \quad (5.8)$$

$$\frac{\partial \rho \varepsilon}{\partial t} + \frac{\partial \rho u_j \varepsilon}{\partial x_j} = \frac{\partial}{\partial x_j} \left(\mu + \frac{\mu_t}{\sigma_\varepsilon} \right) \frac{\partial \varepsilon}{\partial x_j} + \rho(C_{\varepsilon 1}(G + C_{\varepsilon B} G_B) - C_{\varepsilon 2} \varepsilon) \frac{\varepsilon}{k}, \quad (5.9)$$

turbulence production by shear stresses and buoyancy are as follows

$$G = \frac{\mu_t}{\rho} \frac{\partial u_j}{\partial x_i} \left(\frac{\partial u_i}{\partial x_j} + \frac{\partial u_j}{\partial x_i} \right) - \frac{2}{3} \frac{\partial u_k}{\partial x_k} \left(k + \frac{\mu_t}{\rho} \frac{\partial u_k}{\partial x_k} \right), \quad (5.10)$$

$$G_B = -\frac{\mu_t}{\rho} \frac{1}{Pr_t} \frac{g_j}{\rho} \frac{\partial \rho}{\partial x_j}. \quad (5.11)$$

The eddy viscosity is calculated from Kolmogorov-Prandtl formulae,

$$\mu_t = C_\mu \rho \frac{k^2}{\varepsilon}. \quad (5.12)$$

The constants used are $C_\mu = 0.09$, $C_{\varepsilon 1} = 1.44$, $C_{\varepsilon 2} = 1.92$, $C_{\varepsilon B} = 1.0$, $\sigma_k = 1.0$, $\sigma_\varepsilon = 1.3$, $Pr_t = 0.7$, $Sc_t = 0.7$ as suggested by [Launder and Spalding 1972]. This standard model is known to have a number of limitations. For example, this model

fails to adequately predict the correct lateral spreading rate of axisymmetric jets and plumes which results in overestimated axial temperature and velocity, and a poor prediction of flame width and length. A number of approaches have been suggested to resolve the problem, including axisymmetric corrections in the ε -equation, adjustment of constants, and use of the algebraic stress models. In this work, when axisymmetric flames were simulated, the equation (5.9) for turbulence dissipation rate was modified by axisymmetric correction $-C_{\varepsilon 3}k \partial w / \partial z$ to the turbulence production term (according to [Hanjalic, Launder, 1980]), with $C_{\varepsilon 3} = 0.5$. As shown in [Snegirev, 2004], the experimentally observed spreading rates for the axisymmetric plumes in still air [Gengembre *et al*, 1984] are reasonably reproduced when this modification to the ε -equation is used.

What is particularly important for the framework of this study is that the above version of the turbulence model does not take into account the specifics of rotating flows. Indeed, in modelling of *jet* swirling flows, conventional isotropic eddy viscosity turbulence models, such as $k-\varepsilon$, have proved to fail in correct representation of rotating flows. For this kind of flow, several modifications were proposed and explored for the eddy viscosity turbulence models [Leschziner and Rodi, 1981; Sloan *et al*, 1986; Jones and Pascau, 1989; Chang and Cheng, 1993; Yuan and So, 1998, among others]. These modifications were through corrections in the source terms within the dissipation equation (5.9) or correction to the eddy viscosity, Eq. (5.12), by expressing the C_{μ} as a function of rotation.

As shown in the literature review (Chapter 2), there is little experience of numerical modelling of *buoyant* turbulent whirling flames. Indeed, in simulations by [Sato and Yang, 1997] constant viscosity was assumed, and the performance of turbulence model was not addressed. In the work [Battaglia *et al.*, 2000], in which the experimental results reported by Emmons and Ying [Emmons and Ying, 1966] were modelled numerically, the predicted flame lengthening due to imposed rotation was much less pronounced than that observed in the experiments, although a large eddy simulation (LES) technique was applied. In this work, where a $k-\varepsilon$ eddy viscosity model is employed, the approach previously used to improve the model performance in *jet* swirling flows (namely rotation dependent correction of C_{μ}) is applied in the

modelling of *buoyant* whirling flames. It will be shown that the conventional two-equation eddy viscosity turbulence model, after the *ad hoc* modification, allows the experimentally observed lengthening of rotating flames. The discussion below is the justification of such a modification.

As an approximation for realistic vortex behaviour, consider the Rankine-type vortex with angular velocity distribution (4.10) which combines features of solid-body (4.6) and free vortex (4.8) profiles. As mentioned earlier, the central forced vortex region $r < r_0$ (vortex core) exhibits flow field and turbulent characteristics, which are significantly different from those in the surrounding irrotational vortex flow field, $r \gg r_0$. The traditional viewpoint [Sloan et al, 1986] is that the turbulence is stabilised by solid body rotation (i.e. inside the forced vortex core, where the turbulent fluctuations caused by centrifugal acceleration are resisted by the increasing pressure gradient) and destabilised by a free vortex profile. To take this behaviour into account, the Richardson number, Ri , is introduced, that expresses the ratio of centrifugal force of the mean flow to a representative turbulent quantity. The conventional form of the Richardson number is given by [Sloan et al, 1986]:

$$Ri = \frac{v_\theta}{R_c^2} \frac{\partial}{\partial R_c} R_c v_\theta}{\varepsilon^2/k^2}, \quad (5.13)$$

where R_c is the local radius of curvature of the streamline. The numerator in Eq. (5.13) is equal to $2\Omega^2$ in the forced vortex core (4.6), and it tends to zero in the free vortex (4.8). Thus inside the core, the Richardson number (5.13) is inversely proportional to the ratio squared of the period of rotation (of the mean flow) to the turbulent time scale, k/ε . There is however another way to define the Richardson number, expressing the role of centrifugal acceleration of the mean flow explicitly:

$$Ri = \frac{(v_\theta^2/R_c)^2}{\varepsilon^2/k}. \quad (5.14)$$

The latter relationship (where the Richardson number is set to the ratio squared of the centrifugal acceleration, v_θ^2/R_c , (of the mean flow) to the corresponding turbulent quantity, $\varepsilon/k^{1/2}$) was used in this work. The coefficient in the turbulent viscosity formula (5.12) was modified as follows:

$$C_\mu^* = (C_\mu - C_\mu^{\min}) \exp(-C_\omega Ri^2) + C_\mu^{\min}, \quad (5.15)$$

where C_μ^{\min} and C_ω are the adjustable model constants. Note that the Richardson number corrections (either to the source terms in the dissipation equation or to the turbulent viscosity) have not been optimised for general rotating flows, and they can be case-dependent [Sloan et al, 1986; Wilcox, 1998]. Also, the systematic experimental data on buoyant whirling flames, which might be used to determine a suitable constant adjustment, are not yet available. Here, the conclusion made in [Emmons and Ying, 1966] was used, namely that turbulent plume mixing is reduced by an order of magnitude due to flow rotation. We therefore assumed that $C_\mu^{\min}/C_\mu = 0.1$, (whereas $C_\mu = 0.09$ is the conventional value). Reasonable predictions and a relatively weak dependence of the simulation results on the numerical value of C_ω were obtained when C_ω was varied about the value of 10^{-3} . In the simulations performed C_ω was set equal to 0.0012.

Note, other than (5.15) other modifications for C_μ were also proposed for swirling flows, for example one similar to that by [Leschziner and Rodi, 1981]:

$$C_\mu^* = \frac{C_\mu}{1 + C_\omega Ri}. \quad (5.16)$$

Here we prefer to use Eq. (5.15) because, in contrast to Eq. (5.16), the dependence given by Eq. (5.15) has an inflection point, $Ri^* = 1/\sqrt{2C_\omega}$, which separates regimes with negligible ($Ri < Ri^*$) and strong ($Ri > Ri^*$) effect of rotation on turbulence. For $C_\omega = 0.0012$ used in the simulations, $Ri^* = 20.4$.

To calculate the Richardson number the local radius of curvature and the angular velocity are required. In the problems addressed in this work, the radius of curvature should only account for flow rotation about the z axis. It was therefore calculated as [Korn and Korn, 1968]

$$R_c = 1/\sqrt{x''^2 + y''^2},$$

where $x'' = \partial^2 x/\partial s^2$, $y'' = \partial^2 y/\partial s^2$ are the derivatives of the fluid particle and Eulerian coordinates taken in the streamwise direction, and s is the coordinate parallel to the streamline. Differentiation along the streamline yields

$$x'' = \frac{\partial}{\partial s} \left(\frac{\partial x}{\partial s} \right) = \frac{\partial}{\partial s} \left(\frac{\partial x}{\partial t} \frac{dt}{ds} \right) = \frac{\partial}{\partial s} \left(\frac{u}{q} \right) = \frac{1}{q^2} \left(\frac{\partial u}{\partial s} q - u \frac{\partial q}{\partial s} \right), \quad (5.17)$$

$$y'' = \frac{\partial}{\partial s} \left(\frac{\partial y}{\partial s} \right) = \frac{\partial}{\partial s} \left(\frac{\partial y}{\partial t} \frac{dt}{ds} \right) = \frac{\partial}{\partial s} \left(\frac{v}{q} \right) = \frac{1}{q^2} \left(\frac{\partial v}{\partial s} q - v \frac{\partial q}{\partial s} \right), \quad (5.18)$$

where $q = ds/dt = \sqrt{u^2 + v^2}$, since only rotation in $x-y$ plane, i.e. about the z axis, is considered. In the above equations,

$$\begin{aligned} \frac{\partial q}{\partial s} &= \left(\frac{\bar{\mathbf{q}}}{q} \cdot \nabla \right) q = \frac{1}{q} \left(u \frac{\partial q}{\partial x} + v \frac{\partial q}{\partial y} \right), \\ \frac{\partial u}{\partial s} &= \left(\frac{\bar{\mathbf{q}}}{q} \cdot \nabla \right) u = \frac{1}{q} \left(u \frac{\partial u}{\partial x} + v \frac{\partial u}{\partial y} \right), \\ \frac{\partial v}{\partial s} &= \left(\frac{\bar{\mathbf{q}}}{q} \cdot \nabla \right) v = \frac{1}{q} \left(u \frac{\partial v}{\partial x} + v \frac{\partial v}{\partial y} \right), \end{aligned} \quad (5.19)$$

where $\bar{\mathbf{q}} = u\bar{\mathbf{i}} + v\bar{\mathbf{j}}$. For a fluid particle that has coordinates (x, y, z) , the centre of rotation in horizontal plane were found as

$$x_c = x + x''R_c^2, \quad y_c = y + y''R_c^2. \quad (5.20)$$

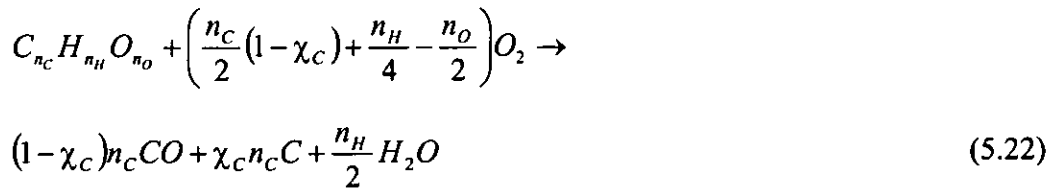
Radial and angular components of the velocity vector were then obtained from

$$v_r = u \frac{x-x_c}{R_c} + v \frac{y-y_c}{R_c}, \quad v_\theta = -u \frac{y-y_c}{R_c} + v \frac{x-x_c}{R_c}. \quad (5.21)$$

The use of the modified coefficient C_μ^* (5.15) for the turbulent viscosity calculation provided significant improvement in the model capability to predict elongation of whirling flames.

5.4. Modelling of combustion and soot formation

A *three-reaction model* for fuel oxidation including two sequential semi-global steps was used in this model. In the first reaction step, fuel decomposition produces carbon monoxide, soot and water vapour:



In the second step, carbon monoxide and soot oxidise to produce carbon dioxide:



The reaction rates for all three reactions (5.22), (5.23) and (5.24) were determined by the eddy break-up model:

$$\dot{R}_{fuel} = C_R^{(1)} \frac{\varepsilon}{k} \min \left(Y_{fuel}, \frac{Y_{O_2}}{s_{O_2}^{(1)}} \frac{Y_{fuel} s_{O_2}^{(1)}}{Y_{fuel} s_{O_2}^{(1)} + Y_{CO} s_{O_2}^{(2)} + Y_C s_{O_2}^{(3)}} \right), \quad (5.25)$$

$$\dot{R}_{CO} = C_R^{(2)} \frac{\varepsilon}{k} \min \left(Y_{CO}, \frac{Y_{O_2}}{s_{O_2}^{(2)}} \frac{Y_{CO} s_{O_2}^{(2)}}{Y_{fuel} s_{O_2}^{(1)} + Y_{CO} s_{O_2}^{(2)} + Y_C s_{O_2}^{(3)}} \right), \quad (5.26)$$

$$\dot{R}_C = C_R^{(3)} \frac{\varepsilon}{k} \min \left(Y_C, \frac{Y_{O_2}}{s_{O_2}^{(3)}} \frac{Y_C s_{O_2}^{(3)}}{Y_{fuel} s_{O_2}^{(1)} + Y_{CO} s_{O_2}^{(2)} + Y_C s_{O_2}^{(3)}} \right). \quad (5.27)$$

where $s_{O_2}^{(1)}$, $s_{O_2}^{(2)}$, and $s_{O_2}^{(3)}$ are the oxygen mass stoichiometric coefficients for reactions (5.22), (5.23), and (5.24), respectively. The standard value, $C_R^{(1,2,3)} = 4.0$ [Magnussen and Hjertager, 1977], was used here similar to other works implementing this model. Soot oxidation was neglected for mean temperatures below $T_{SOx \min} = 640$ K.

Soot formation was modelled using the empirical relationship from [Khan and Greeves, 1974],

$$\rho \dot{R}_{SF} = C_{SF} P_{fuel} \phi^n \exp(-E_{SF}/RT), \quad (5.28)$$

which couples the soot formation rate with the partial fuel pressure, P_{fuel} , the equivalence ratio, $\phi = (Y_{fuel} s_{O_2}^{(1)})/Y_{O_2}$, and the temperature, T . The numerical values of $n = 3$ and $E_{SF}/R = 20\,000$ K were used as in previous studies [Khan and Greeves, 1974; Abbas and Lockwood 1985; Coelho and Carvalho, 1995].

In averaging the soot formation rate, Eq. (5.28), it was assumed that the major effect of turbulence is due to temperature fluctuations. An approximate relationship has been obtained in [Snegirev, 2004] that couples the averaged soot formation rate, $\overline{\dot{R}_{SF}}$, with the mean temperature, \overline{T} , and its variance, $\Delta T = \sqrt{\overline{T'^2}}$ (the latter is calculated from separate transport equation for $\overline{T'^2}$, Eq. (5.42)). Approximating

probability density function for temperature fluctuations by two delta functions, the temperature dependent term of the average soot formation rate (5.28) can be shown (see [Snegirev, 2004]) to be equal to $A \cdot \exp(-E_{SF}/RT)$; the factor $A = \exp(E_{SF}\Delta T/RT^2)$ approximately accounts for the effect of temperature fluctuations¹.

The soot production efficiency, χ_C , appearing in Eq. (5.22) is then obtained as $\chi_C = \min\left(1, \left(W_{fuel} \overline{\dot{R}_{SF}} / n_C W_C \overline{\dot{R}_{fuel}}\right)\right)$, where $\overline{\dot{R}_{fuel}}$ is the reaction rate of fuel oxidation. The model parameter, C_{SF} , was taken to be $C_{SF} = 6.0 \text{ kg}/(\text{N}\cdot\text{m}\cdot\text{s})$.

Table 5.1. Mass stoichiometric coefficients (three reaction scheme)

α		$s_\alpha^{(1)}$	$s_\alpha^{(2)}$	$s_\alpha^{(3)}$
Fuel	$C_{n_C} H_{n_H} O_{n_O} N_{n_N}$	1		
Oxidiser	O_2	$\left(\frac{n_C}{2}(1-\chi_C) + \frac{n_H}{4} - \frac{n_O}{2}\right) \frac{W_{O_2}}{W_{fuel}}$	$\frac{1}{2} \frac{W_{O_2}}{W_{CO}}$	$\frac{W_{O_2}}{W_C}$
Products	C	$\frac{\chi_C n_C W_C}{W_{fuel}}$		1
	CO	$\frac{(1-\chi_C) n_C W_{CO}}{W_{fuel}}$	1	
	CO_2	0	$\frac{W_{CO_2}}{W_{CO}}$	$\frac{W_{CO_2}}{W_C}$
	H_2O	$\frac{n_H}{2} \frac{W_{H_2O}}{W_{fuel}}$		
	N_2	$\frac{n_N}{2} \frac{W_{N_2}}{W_{fuel}}$		

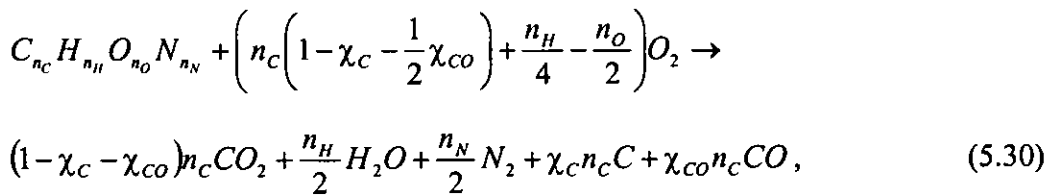
¹ In Eqs (5.1)-(5.7), the overbar is omitted for the mean quantities.

The source terms, \dot{r}_α , in specie conservation equations (5.2) take the form:

$$\begin{aligned}
 \dot{r}_{fuel} &= -\dot{R}_{fuel}, & (5.29) \\
 \dot{r}_{CO} &= s_{CO}^{(1)}\dot{R}_{fuel} - \dot{R}_{CO}, \\
 \dot{r}_C &= s_C^{(1)}\dot{R}_{fuel} - \dot{R}_C, \\
 \dot{r}_{CO_2} &= s_{CO_2}^{(2)}\dot{R}_{CO} + s_{CO_2}^{(3)}\dot{R}_C, \\
 \dot{r}_{H_2O} &= s_{H_2O}^{(1)}\dot{R}_{fuel}, \\
 \dot{r}_{O_2} &= -s_{O_2}^{(1)}\dot{R}_{fuel} - s_{O_2}^{(2)}\dot{R}_{CO} - s_{O_2}^{(3)}\dot{R}_C,
 \end{aligned}$$

where the indices ⁽¹⁾, ⁽²⁾, ⁽³⁾ correspond to reactions (5.22), (5.23), and (5.24) respectively, $s_\alpha^{(i)}$ are the (positive) mass stoichiometric coefficients of α -th component in i -th reaction given in Table 5.1.

Justification of this combustion model is discussed in [Snegirev, 2004]. Despite its simplicity, the model provides predictions, which are mainly in agreement with the experimental data and with the more advanced combustion models. A one-step reaction,



with constant prescribed values of χ_C and χ_{CO} taken from published measurements (0.07 and 0.01 for diesel, 0.04 and 0.007 for heptane, 0.01 and 0.0 for ethanol) was also used in the simulations; the choice of soot formation model did not significantly affect the structure and behaviour of the whirling flames studied. Note, the phenomenon of flame whirling, being mainly of hydrodynamic nature (see the explanation based in the analysis of vorticity equation in Section 4.4), appeared to be

not too sensitive to the choice of combustion model. Therefore, the use of simple and robust model described above is justified for the purpose of this work.

5.5. Modelling of thermal radiation

In this model, a non-scattering media is considered, spectral properties of which were approximated by the effective absorption coefficient (gray media assumption). Scattering of thermal radiation by soot is neglected since the diameter of primary particles composing soot aggregates formed in flames is significantly less than the characteristic radiation wavelength [Viskanta, Menguc, 1987]. The gray media assumption is justified by the appropriate choice of the effective absorption coefficient as discussed later.

The radiative transfer equation (RTE) integrated over the entire spectrum is employed [Viskanta and Menguc, 1987; Modest, 1993; Lallemand et al, 1996]:

$$\frac{dI}{ds} = \kappa_p I_b - \kappa I, \quad (5.31)$$

where

$$I = \int_0^\infty I_\lambda d\lambda$$

is the total intensity,

$$I_b = \int_0^\infty I_{b\lambda} d\lambda = \sigma T^4 / \pi$$

is the black body intensity,

$$\kappa_p = \int_0^\infty \kappa_\lambda I_{b\lambda} d\lambda / \int_0^\infty I_{b\lambda} d\lambda \quad (5.32)$$

is the Planck mean absorption coefficient, and

$$\kappa = \int_0^{\infty} \kappa_{\lambda} I_{\lambda} d\lambda / \int_0^{\infty} I_{\lambda} d\lambda \quad (5.33)$$

is the incident mean absorption coefficient. Generally $\kappa_p \neq \kappa$ since the spectrum of incident radiation, I_{λ} , differs from that of black body, $I_{b\lambda}$. However, for a gray media $\kappa_p = \kappa$, and the RTE, Eq. (5.31), simplifies to

$$\frac{dI}{ds} = \kappa(I_b - I). \quad (5.34)$$

To solve the energy conservation equation, the divergence of radiative heat flux must be calculated,

$$\nabla q_r = \kappa(4\sigma T^4 - G), \quad (5.35)$$

where $G = \int_{4\pi} I d\omega$ is incident radiation; this being the total radiation intensity impinging on a point from all directions.

The effective emission/absorption coefficient, κ , is calculated to provide a correct value for the total emissivity of the mixture occupying a given control volume of the computational grid. Although such an approach suffers from lack of a theoretical justification, previously reported predictions of the total radiative heat flux (as discussed e.g. in [Lallemant *et al*, 1996] and demonstrated in [Snegirev, 2004]) were found to be in reasonable agreement with the measured radiative fluxes. Further validation studies against the measurements made in this work are shown later in Section 5.8.

5.5.1. Radiative properties of combustion products

The participating media comprises CO_2 , H_2O , soot, CO , and unburnt hydrocarbons.

For CO_2 and H_2O mixtures, the gray absorption coefficient, $\kappa_{CO_2+H_2O}$, is defined for each grid cell, such that it yields the same total emissivity, $\varepsilon_{CO_2+H_2O} = 1 - \exp(-\kappa_{CO_2+H_2O}L)$, as that obtained from the exponential wide-band model (which is often used to provide benchmark data, for example see [Lallemant et al, 1996; Smith et al, 1982]) in a homogeneous media. The total emissivity is calculated using the relationship,

$$\varepsilon_{CO_2+H_2O} = \sum_{i_g=0}^3 a_{g,i_g}(T) \left(1 - \exp(\kappa_{g,i_g}(P_{CO_2} + P_{H_2O})L) \right), \quad (5.36)$$

in which the gas mixture is represented by one transparent and three gray gases with absorption coefficients κ_{g,i_g} . The weighting factors, $a_{g,i_g}(T)$, are dependent on temperature,

$$a_{g,i_g}(T) = \sum_{j=0}^3 b_{g,i_g,j} T^j, \quad i_g = 0, 1, 2, 3. \quad (5.37)$$

The numerical values of polynomial coefficients $b_{g,i_g,j}$ and absorption coefficients κ_{g,i_g} were taken from [Smith et al, 1982]. For a grid cell with sides Δx , Δy , Δz , volume $\Delta V = \Delta x \Delta y \Delta z$, and surface area $\Delta A = 2(\Delta x \Delta y + \Delta x \Delta z + \Delta y \Delta z)$, the mean path-length is calculated as $L = 3.6 \Delta V / \Delta A$. The mean absorption coefficient is then derived as

$$\kappa_{CO_2+H_2O} = \frac{1}{L} \ln \left(\frac{1}{1 - \varepsilon_{CO_2+H_2O}} \right). \quad (5.38)$$

The soot absorption coefficient is calculated as in [Smith et al, 1987],

$$\kappa_{soot} = f_V \sum_{i_s=1}^2 a_{s,i_s}(T) \kappa_{s,i_s}, \quad (5.39)$$

where the soot is represented by two gray “gases”, $i_s = 1, 2$, with the absorption coefficients κ_{s,i_s} .

The contribution of carbon monoxide and unburnt hydrocarbons is also approximately accounted for in the proposed model. Because of lack of experimental data on radiative properties of hydrocarbons, the fuel absorption coefficient, $\kappa_{fuel}(T)$, is equated here to that of methane. In view of the low fuel partial pressure in the flame zone, the error introduced by this assumption is not expected to be significant, with the exception of very large pool fires. Mean absorption coefficients for methane and carbon monoxide, $\kappa_{CH_4}(T)$ and $\kappa_{CO}(T)$, were calculated using data from [Marracini and Lentini, 1997], both in the optically thin limit. The total mean absorption coefficient for the gas-soot mixture is then calculated as the sum,

$$\kappa = \kappa_{CO_2+H_2O}(T, P_{CO_2}, P_{H_2O}, L) + \kappa_{soot}(T, f_V) + \kappa_{CO}(T, P_{CO}) + \kappa_{fuel}(T, P_{fuel}), \quad (5.40)$$

of the all the contributing components.

5.5.2. Turbulence-radiation interaction

Turbulence-radiation interaction might be particularly important in buoyant flames with high magnitude of turbulent fluctuations. Indeed, root mean square of the velocity and temperature fluctuations were found to be up to 50% of its average values, see [Cox and Chitty, 1982; Gengembre et al, 1984]. In this work, the effect of turbulent fluctuations is approximately taken into account through its influence on the radiation emission [Snegirev, 2004]:

$$\overline{\sigma\kappa T^4} = \overline{\sigma\kappa} \cdot \overline{T^4} \left(1 + C_{TRI1} 6 \frac{\overline{T'^2}}{\overline{T}^2} + C_{TRI2} 4 \frac{\overline{T'^2}}{\overline{\kappa} \cdot \overline{T}} \frac{\partial \overline{\kappa}}{\partial \overline{T}} \right), \quad (5.41)$$

where the absorption coefficient $\overline{\kappa}$ is calculated from Eq. (5.40), and the mean square temperature fluctuation $\overline{T'^2}$ is obtained from separate transport equation, Eq. (5.42). The constants used are $C_{TRI1} = 2.5$ and $C_{TRI2} = 1.0$ [Snegirev, 2004].

The temperature variance, $\overline{T'^2}$, (which is needed to calculate time averaged radiation emission rate (5.41) and soot formation rate (5.28)) is obtained by solving corresponding transport equation [Kuo, 1986; Poinsoot and Veynante, 2001]:

$$\frac{\partial \rho \overline{T'^2}}{\partial t} + \frac{\partial \rho u_j \overline{T'^2}}{\partial x_j} = \frac{\partial}{\partial x_j} \left(\mu + \frac{\mu_t}{Pr_t} \right) \frac{\partial \overline{T'^2}}{\partial x_j} + 2 \frac{\mu_t}{Pr_t} \frac{\partial \overline{T}}{\partial x_j} \frac{\partial \overline{T}}{\partial x_j} - C_T \rho \overline{T'^2} \frac{\varepsilon}{k}, \quad (5.42)$$

where $C_T = 2.0$ is the model constant.

5.5.3. Statistical modelling of thermal radiation transfer

The statistical (Monte Carlo) method (for example, see [Modest, 1993]) is used to model thermal radiation transfer. This is the advanced methodology that circumvents the ray effect which is inherent in more conventional (discrete transfer, discrete ordinate, multi-flux) methods currently used in CFD fire models. Such an improvement is extremely important in quantitative predictions of thermal impact of fire onto surrounding structures.

In modelling the interaction of the radiation emitted from the plume with solid boundaries we assume the solid surfaces to be gray diffuse emitters and reflectors that are maintained at a constant temperature. The method is applied to radiation emitted by both gases and particles in any internal control volume and by boundary surface elements. In both cases the method is applied in each time step and it consists of the following two stages [Snegirev, 2004]:

When the radiation emission by *internal control volumes* is calculated:

1. Every control volume (grid cell) launches a sufficiently large amount (discussed below) of energy bundles (“photons”), the total energy of which is equal to $4\sigma\kappa T^4 \Delta V \Delta t$, where ΔV is the cell volume, Δt is the time step. The locations of the emission points inside the grid cell and the photon travelling directions are randomly chosen with probability uniformly distributed over the solid angle (emission is isotropic). The photon then travels along straight lines. As a photon is launched, the energy contained in the grid cell is reduced by the energy of the photon.

2. The history of a travelling photon is then tracked. A photon may be absorbed into the grid cell, which results in an increase of the energy of the grid cell by the energy of the absorbed photon, or may penetrate into the adjacent grid cell where its history is tracked in a similar manner. A photon may also approach a boundary of the computational domain (solid wall or open boundary) and in this case a decision is made to either absorb the photon or to reflect it away from the boundary. The probability of absorption is proportional to the wall absorptivity, which is assumed here to be equal to the wall emissivity, ϵ_w , and if absorbed, a photon contributes its energy to the radiative heat flux received by the boundary.

When the radiation emission by the boundary *surface elements* is calculated:

1. Every boundary surface element (boundary face of a grid cell) launches a sufficiently large amount of photons in which the total energy is equal to $\epsilon_w \sigma T^4 \Delta A \Delta t$, where ΔA is the area of the surface element. The locations of emission points inside the surface element and the photon travelling directions are randomly chosen with their probability uniformly distributed over the hemisphere above the element (the boundary is assumed to be a diffuse emitter). As above, the photon then travels along straight lines and as a photon is launched, the energy received by the surface element at a given time step is reduced by the energy of the photon.

2. The history of a travelling photon is then tracked, similar to that for the photons launched by internal grid cells.

The value of the divergence of radiative heat flux, ∇q_r , which is the sink term the enthalpy equation is equated to the difference between emitted and absorbed energy divided by $\Delta V \Delta t$.

The photon tracking procedure is as follows. Let r_x , r_y , r_z , r_θ , r_ϕ , and r_{abs} are the random variables uniformly distributed between 0 and 1. Coordinates of the launching point, x_0 , y_0 , z_0 , of the photon are then calculated as

$$\begin{aligned}x_0 &= x_{i-1} + r_x(x_i - x_{i-1}), \\y_0 &= y_{j-1} + r_y(y_j - y_{j-1}), \\z_0 &= z_{k-1} + r_z(z_k - z_{k-1}),\end{aligned}$$

where x_i , y_j , z_k are the coordinates corresponding to grid faces (the grid is composed by rectangular cells). The direction of the travelling direction is represented by vector $\vec{\omega} = \omega_x \vec{i} + \omega_y \vec{j} + \omega_z \vec{k}$, in which the direction cosines are related to polar and azimuthal angles θ and ϕ :

$$\begin{aligned}\omega_x &= \sin \theta \cos \phi, \\ \omega_y &= \sin \theta \sin \phi, \\ \omega_z &= \cos \theta.\end{aligned}$$

Angles θ and ϕ are derived from the following relationships:

$$\begin{aligned}\cos \theta &= 2r_\theta - 1, \\ \phi &= 2\pi r_\phi,\end{aligned}$$

to provide isotropic emission over the entire solid angle.

As the direction of the photon travelling is specified, the photon trajectory in 3D space and therefore the coordinates, x , y , z , of the photon entrance into the next adjacent grid cell are obtained from

$$\frac{x - x_0}{\omega_x} = \frac{y - y_0}{\omega_y} = \frac{z - z_0}{\omega_z},$$

where x_0 , y_0 , z_0 are the coordinates of either the point of photon emission or the point of first appearance of the photon in the grid cell. The path length to the photon absorption, L_{abs} , inside a given grid cell with absorption coefficient, κ , is calculated as

$$L_{abs} = \frac{1}{\kappa} \ln \left(\frac{1}{1 - r_{abs}} \right).$$

If L_{abs} turns out to be less than the distance to the adjacent grid cell along the photon trajectory, then the photon is considered to be absorbed by the media.

The number of photons launched by each grid cell and surface element was taken to be proportional to the difference between the radiation emission at grid cell temperature and the radiation emission at minimum (background ambient) temperature:

$$N_{vol\ i,j,k} = N_{vol\ max} \frac{\kappa(T^4 - T_0^4)\Delta V}{\sum_{vol\ i,j,k} \kappa(T^4 - T_0^4)\Delta V},$$

$$N_{surf\ i,j,k} = N_{surf\ max} \frac{\epsilon_w(T^4 - T_0^4)\Delta A}{\sum_{surf\ i,j,k} \epsilon_w(T^4 - T_0^4)\Delta A}.$$

With this approach, photons cannot be launched by the cold media, thereby avoiding temperature undershoots which may appear in this case because of finite photon energy and finite number of photons. The total number of photons, $N_{total} = N_{vol\ max}$

+ $N_{surf \max}$, was taken in the range from 10^5 to $2 \cdot 10^6$. The energy of each photon was obtained as the ratio of the radiation emission by the grid cell ($4\sigma\kappa T^4 \Delta V \Delta t$) divided by the number of photons launched by the cell.

5.6. Boundary and initial conditions

Two types of flames, unconfined and enclosed have been modelled in this work. Similar to the experimental setup described in Chapter Three the round shape fuel burner was located centrally at floor level. The domain size had dimensions of $2.4 \times 2.4 \times 3.29$ m for unconfined flames and for enclosed flames the enclosure measured $2.4 \times 2.77 \times 3.29$ and the computational domain was further expanded beyond this enclosure to a size of $3.4 \times 2.77 \times 3.29$ m, (further extension of the boundary did not significantly affect the numerical solutions) and at the open boundaries the dynamic pressure p was set to zero. Initial values were assigned for all transported quantities in the inlet part of the open boundaries and zero normal gradients were imposed for all the quantities leaving the computational domain. In solving equation (5.42) for temperature variance, zero initial and boundary conditions were used. On the solid wall surfaces, conventional wall functions were used to specify boundary conditions for turbulent quantities, tangential velocity and enthalpy whilst a zero pressure gradient was imposed on pressure. The temperature of the solid wall was equal to the initial temperature, T_0 .

Boundary conditions, particularly for turbulent quantities, k and ε , at the burner exit or fuel surface significantly affect the flame shape and structure. The usual approach is to relate k_{fuel} and ε_{fuel} to the fuel velocity, $k_{fuel} = C_k V_{fuel}^2$, $\varepsilon_{fuel} = C_\varepsilon k_{fuel}^{3/2} / l_{t,fuel}$, where the turbulent length scale, $l_{t,fuel}$, is expressed via the burner size (e.g. equal to the burner radius [Adiga *et al*, 1989]), and C_k and C_ε , are the adjustable parameters. However, optimum values for these parameters were found to be case dependent and this is because the fuel velocity at the burner exit, V_{fuel} , is not a characteristic value for the entire flow, which is (dissimilar to high-momentum jet flames) driven by buoyancy rather than by the fuel momentum. This

is reflected in very small values, of the Froude number, $Fr = V_{fuel}^2 / (gD)$ being in the order of (10^{-6} to 10^{-4} see Table 3.2), A similar approach (used in [Blundson, 1996]) is to preassign numerical values for k_{fuel} and $l_{t,fuel}$ at the burner exit and to also introduce two adjustable parameters. However, in the case of buoyant flames, which is also applicable to evaporating pool fires, the burner or pool surface should be regarded as a solid one rather than as an inlet flow through a jet nozzle, thereby avoiding use of extra adjustable parameters (C_k and C_ϵ , or k_{fuel} and $l_{t,fuel}$) in the model. This assumption is used here neglecting, the very low velocity of emanating fuel vapour from the surface and the effect of mass transfer. As flow near to the burner exit or fuel surface might not be fully turbulent, it is important to allow for this possibility by a near-surface control volume, either in the viscous sub layer or in the turbulent part of flow.

A wall function approach was used to specify boundary conditions (fuel, floor, walls and ceiling surfaces) for turbulent quantities, tangential velocity, and enthalpy. The central points of near-wall control volumes (designated here by index P) were specially considered. Depending on the numerical value of $\eta_p = C_\mu^{1/4} \rho \sqrt{k_p} \Delta x_p / \mu$, point P was regarded as situated within the viscous sublayer ($\eta_p \leq \eta_0 = 11.5$) or in the turbulent region ($\eta_p > \eta_0$). Shear stress and heat flux at the surface were calculated from $\tau_w = \mu^* V_p / \Delta x_p$ and $q_w = -D^* (h_p - h(T_w)) / \Delta x_p$, respectively, where V_p is tangential velocity, Δx_p is normal distance from the surface to point P . Linear profiles were assumed for tangential velocity and enthalpy inside the viscous sublayer, (i.e. $\mu^* = \mu_p$ and $D^* = \mu_p / Pr$, if $\eta_p \leq \eta_0$). The log-law was applied within the turbulent region (i.e. $\mu^* = \rho_p C_\mu^{1/4} \sqrt{k_p} \kappa \Delta x_p / \ln(E_v \eta_p)$ and $D^* = \rho_p C_\mu^{1/4} \sqrt{k_p} \kappa \Delta x_p / Pr_t \ln(E_h \eta_p)$, if $\eta_p > \eta_0$; constants $E_v = \exp(\eta_0 \kappa) / \eta_0 = 9.71$ and $E_h = \exp(Pr \eta_0 \kappa / Pr_t) / \eta_0 = 10.4$ were obtained by matching linear and logarithmic profiles at $\eta_p = \eta_0$ with $\kappa = 0.41$, $Pr = 0.72$, $Pr_t = 0.7$. In solving the transport equation for k , the diffusion of k to the surface was neglected and in the near-wall control volumes the dissipation rate was prescribed as $\epsilon_p = 2\mu_p k_p / \rho_p \Delta x_p^2$ [Wilcox, 1998] if $\eta_p \leq \eta_0$ and $\epsilon_p = C_\mu^{3/4} k_p^{3/2} / \kappa \Delta x_p$ otherwise. Turbulence generation rate was equated to ϵ_p , and the

turbulent viscosity was set as in [Zaichik, 1997]:

$$\mu_{t,p} = \mu_p \left(\sqrt{1 + 4[\kappa\eta_p(1 - \exp(-\eta_p/A))]^2} - 1 \right) / 2$$
, where $A = 26$ this being the Van Driest constant. The latter relationship for μ_t allows for limiting cases of both the turbulent region ($\eta_p \rightarrow \infty$, $\mu_{t,p} \rightarrow C_\mu \rho k_p^2 / \epsilon_p$) and the viscous sublayer ($\eta_p \rightarrow 0$, $\mu_{t,p} \rightarrow \rho_p l_{mix}^2 V_p / \Delta x_p$, where $l_{mix} = \kappa \Delta x (1 - \exp(-\eta_p/A))$ is the mixing length).

The temperature of the solid walls, T_w , was set equal to the ambient temperature, T_0 . Ambient values were also assigned for all the transported quantities within the inlet part of the open boundaries and zero normal gradients were imposed for all the quantities leaving the computational domain. In solving Eq. 5.42 for temperature variance, no boundary conditions were used. The ambient air characteristics were taken as follows: temperature is $T_0 = 298$ K, pressure is 1 atm, nitrogen and oxygen mass fractions are 0.77 and 0.23 respectively, and the turbulent parameters are $k_0 = 10^{-3} \text{ m}^2/\text{s}^2$ and $\epsilon_0 = 10^{-3} \text{ m}^2/\text{s}^3$, which corresponds to a turbulent length scale of $k_0^{3/2} / \epsilon_0 = 0.032$ m.

In radiation modelling, the wall surface emissivity was taken as $\epsilon_w = 0.7$ and the emissivity of the liquid fuel surface was set to 0.4. The photons that approached an open boundary were considered to have left the computational domain.

In modelling the burning liquid pool fire, two approaches to describe the fuel supply rate are used. The first one implies a constant prescribed fuel evaporation rate, \dot{m}_{fuel} (mass burning rate) and in this work the numerical value for this parameter was taken from the experimentally measured range of mass burning rates obtained in Chapter Three. Within the second approach, the thermal feedback between the gas flame and the fuel surface is taken into account and it was assumed, that the evaporation rate is limited mainly by the incident heat flux. This assumption is valid, if the temperature of a liquid surface is close to its boiling point (which is typical for a fully developed fire). In the experiments, the subsurface temperature of the fuels used was indeed close to the boiling point (measured by thermocouple shown in Fig.

3.4); and therefore the boiling temperature was used as a boundary value at the fuel surface in the simulations. The burning rate was then calculated from the heat balance at the fuel surface given by,

$$\dot{m}_{fuel}(x, y) = \frac{q_{fuel}(x, y)}{\Delta H_{vap}(T_0)}, \quad (5.43)$$

where

$$q_{fuel}(x, y) = q_r + q_c - q_0 \quad (5.44)$$

is the total (net radiative and convective minus heat loss rate) heat flux received by a given point of the fuel surface; and $\Delta H_{vap}(T_0)$ is the enthalpy of vaporisation at initial conditions and the fuel temperature taken equal to T_0 .

In Eq. (5.43) the net radiative heat flux, q_r , is calculated by the statistical method as a balance of the incident and reflected radiant fluxes and less fuel surface radiation emission. The convective heat flux, q_c , is calculated using a wall function approach as discussed above; and the heat loss rate is assumed to be proportional to the difference between fuel surface temperature and the ambient temperature is given by.

$$q_0 = h_{fuel}(T_{fuel} - T_0). \quad (5.45)$$

The origin of the heat losses from the fuel is the heat flux from the fuel surface to the base of the fuel pan and floor. Therefore, the heat transfer coefficient, h_{fuel} , represents the thermal resistance of: (i) the substrate, (ii) the contact layer between the substrate and the bottom of the pan (metal skirt of 0.05 m as described in Section 3.2.2), (iii) the pan bottom itself, and (iv) the fuel layer between the top of the fuel surface and the bottom of the fuel pan. Numerical values for these quantities are case dependent and are difficult to be estimated for a general situation. For the experimental arrangements made in this work, zero value of h_{fuel} was assumed.

5.7. Numerical implementation

Two types of flames, unconfined and enclosed, have been modelled in this work. Similar to the experimental studies (See Chapter 3), in both cases a circular fuel pan of 0.6 m diameter was located centrally within the enclosure at the floor level. The domain size had dimensions 2.4x2.4x3.29 m for unconfined flames. In modelling the enclosed flame dynamics, the experimental enclosure 2.4x2.4x3.29 m was reproduced and in the latter case, the computational domain was expanded beyond the enclosure, having the dimensions of 3.4x2.77x3.29 m. The flow equations were discretised by using a finite volume approach [Hirsch, 1988; Ferziger and Peric, 1999]. The non-uniform rectangular computational grid consisted of a total of 102400 cells (40x40x64 grid nodes) that were employed in the simulations of unconfined flames; 122880 cells (48x40x64 grid nodes) were used in the simulations of flames within the enclosure and the grid nodes were concentrated within the flame zone to better resolve high gradients of the parameters. The fuel surface was spanned by 264 grid nodes of which the minimum cell sizes were of 0.0375x0.0375x0.03 m. and for preliminary simulations a coarser grid was also used, being 18432 cells (24x24x32 nodes). Table 5.2 illustrates the effect of the grid sensitivity in relation to the periodic formation and destruction of the vortex core at a prescribed burning rate (in this case 0.040kg (m.s²). The use of a coarse grid predicts that the periodicity is in the order of 21 seconds, further refinement of the grid nodes results in values of 16 and 13 seconds using a medium and fine grid respectively. Further grid refinement although prohibitively expensive for computers at the time is not therefore expected to result in changes more than 20%. Similar behaviour was demonstrated by other monitored parameters i.e. the wall heat fluxes, flame height and its averaged axial temperatures. The spatial derivatives used in the diffusion terms were approximated by second order central differences. For the convective terms, first order upwind (UDS-1) and TVD schemes (with Van Albada limiter [Hirsch, 1988]) were applied. A fully implicit scheme was employed with a first order time accurate approximation of temporal derivatives.

Grid type	Nodes	Period, s
Coarse	24x24x32	21
Medium	36x32x48	16
Fine	48x40x64	13

Table. 5.2. Sensitivity of the grids used in relation to periodic formation and destruction of the vortex core for a constant prescribed burning rate.

A staggered grid arrangement was used in conjunction with a pressure correction technique, which couples the pressure and velocity fields in the low Mach number limit to satisfy the continuity equation. The Poisson equation for pressure correction, that is derived from the continuity equation, was solved numerically using the multigrid approach based on V-cycling over four nested grids with a successive line over-relaxation (SLOR) smoothing technique [Hirsch, 1988]. Discretised flow equations were also solved by the SLOR at each time step. The solution was regarded as converged when the residual heat flux scaled against a representative flux fell below 10^{-4} . To provide coupling between the variables at each time step, all the equations were included into the external iteration loop. The time step was calculated to keep the Courant number no greater than a prescribed maximum value at each grid cell. The maximum Courant number was 2.0 or 0.6 depending on whether the first order upwind or TVD scheme was used. The code was developed for transient simulations and the steady-state solutions were obtained by solving the unsteady problem until the steady state was approached.

To assess the dependence of the numerical solutions obtained on the computational grid and the discretisation scheme used, computational trials using the two above mentioned grids with significantly different cell sizes (for preliminary simulations a coarser grid was used being 18432 cells (24x24x30 nodes as opposed to the use of 122880 nodes in the simulations)). This sensitivity analysis demonstrated that the solutions reported below are *qualitatively* grid-independent, although the numerical values of the calculated quantities changed observably with grid refinement. The

period between stages of formation of a whirling flame within an enclosure is not expected to change more than by 20% due to further grid refinement, which was not possible because of severe CPU time requirements.

5.8. Conclusions

As a numerical tool for this study, the CFD model and code *Fire3D* has been adjusted to take into account the effects of rotation particularly the inhibited turbulent mixing within the whirling core. The Richardson number has been introduced as a controlling criterion and the C_{μ} coefficient is dependent upon the Richardson number thereby reducing turbulent viscosity in the whirling core. This improvement was undertaken as a part of this work.

In addition to earlier validation studies, the model and code were examined to test their capability in predicting radiant heat fluxes from the flames. Reasonable agreement has been obtained between the experimental and numerically predicted values for the heat fluxes at the enclosure wall. This observation supports the credibility of the model which is used for numerical studies of whirling. The results of such work are fully discussed within the next section.

CHAPTER 6.

NUMERICAL SIMULATIONS OF WHIRLING FLAMES

6.1. Simulations of open whirling flames

Numerical simulations were conducted on unconfined whirling flames above a fuel source being 0.6 m in diameter that is centrally located at floor level (representing that used in our experiments). The flames were modelled in a computational domain such that $0 < x < x_{\max}$, $0 < y < y_{\max}$, $0 < z < z_{\max}$ with $x_{\max} = y_{\max} = 2.4$ m, $z_{\max} = 3.29$ m. The non-uniform rectangular computational mesh consisted of a total of 102400 control volumes (40x40x64 grid nodes) and these grid nodes were concentrated within the flame zone to better resolve the higher gradients of the parameters. The fuel surface was spanned by 264 grid nodes of which the minimum cell sizes were 0.0375x0.0375x0.03 m.

Externally imposed circulation was modelled through boundary conditions imposed upon the velocity components tangential to the vertical boundaries of the computational domain. These velocity profiles were chosen to represent a free (potential) vortex and derived from Eq. (4.8) and (4.9):

$$u(x) = -\frac{\Gamma_0}{2\pi} \frac{y - y_0}{(x - x_0)^2 + (y - y_0)^2}, \quad y = 0, y_{\max}, \quad (6.1)$$

$$v(y) = \frac{\Gamma_0}{2\pi} \frac{x - x_0}{(x - x_0)^2 + (y - y_0)^2}, \quad x = 0, x_{\max},$$

where x_0 , y_0 are the coordinates of the flow symmetry axis (half of the horizontal size each), $\Gamma_0 = 2\pi x_0 u_{\max}$ is the external circulation, and u_{\max} is the maximum tangential velocity at the boundary. The effects of the external circulation upon flames that exhibited different heat release rates were numerically studied. The fuel supply rates, \dot{m}_{fuel} , were varied from 0.010 to 0.040 kg/(m²·s), which covers the time-averaged burning rates measured in the experiments. To approximate diesel properties, gas fuel representing vaporised kerosene, $C_{14}H_{30}$, was used of which the physical properties are shown in Table 3.1.

The steady state mean temperature fields and flow streamlines for a numerically simulated whirling flame within an open space having a mass loss rate value from the fuel surface of $\dot{m}_{fuel} = 0.040$ kg/(m²·s), which corresponds to a heat release rate of 516 kW (in this case diesel fuel), is shown in Fig. 6.1. Unconfined free-standing non-rotating flames ($u_{\max} = 0$ m/s, $\Gamma_0 = 0$ m²/s), and flames with a relatively weak ($u_{\max} = 0.2$ m/s, $\Gamma_0 = 1.45$ m²/s) and strong ($u_{\max} = 0.6$ m/s, $\Gamma_0 = 4.35$ m²/s) imposed external circulation are presented within this chapter.

Clearly, external circulation significantly affects the predicted flame shape and length. Similar to earlier reported measurements [Emmons and Ying, 1966; Gupta et al, 1984; Satoh and Yang, 1996] and experimental observations (presented in Chapter Three), rotation may cause significant flame lengthening (Fig. 6.1b). However, the model also predicts flame shortening if the external circulation imposed is greater than some particular value (Fig. 6.1c).

6. Numerical simulations of whirling flames

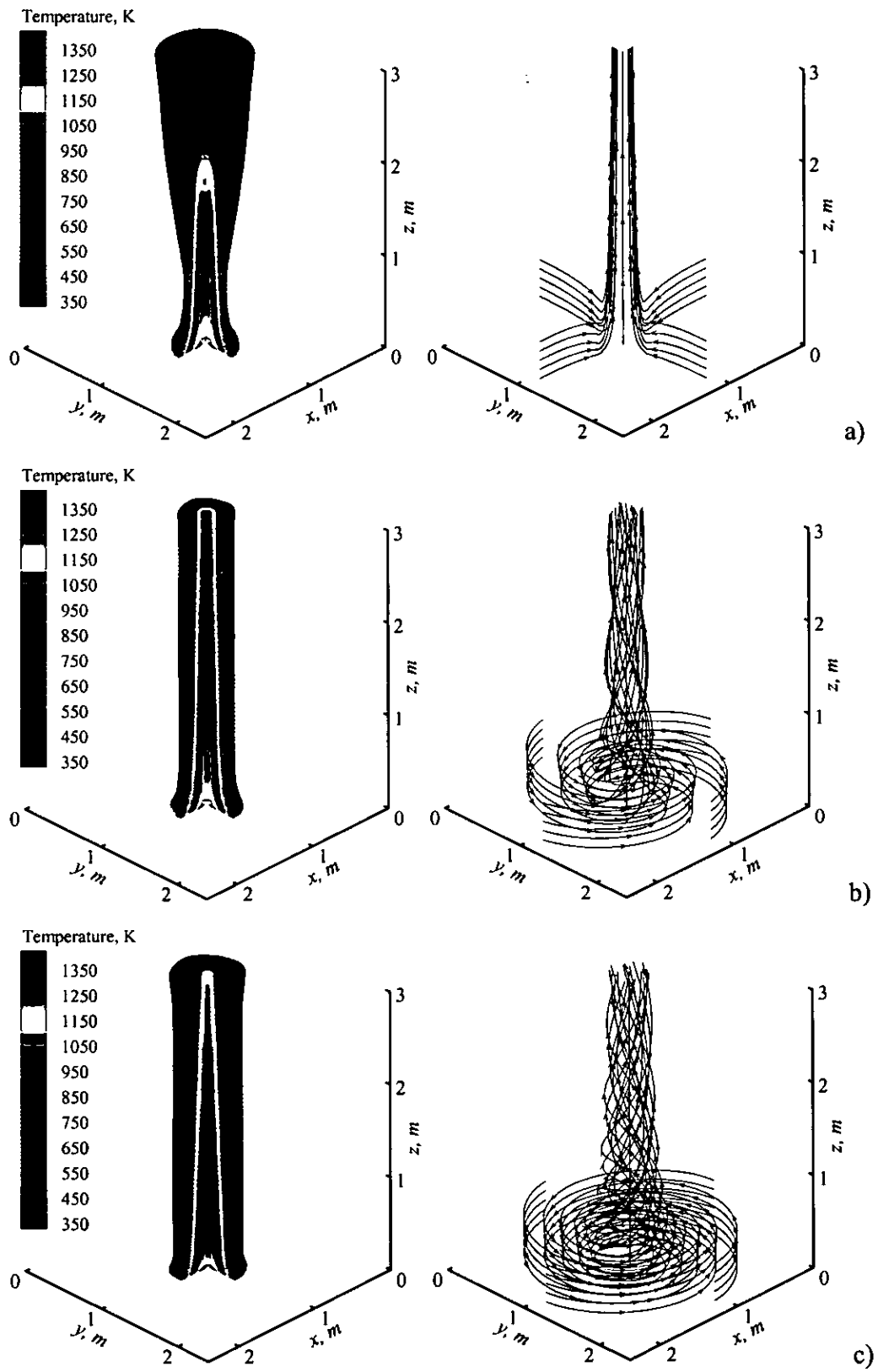


Fig. 6.1. Steady state mean temperature fields and mean-flow streamlines in a 516 kW flame: a) $\Gamma_0 = 0 \text{ m}^2/\text{s}$; b) $\Gamma_0 = 1.45 \text{ m}^2/\text{s}$; c) $\Gamma_0 = 4.35 \text{ m}^2/\text{s}$.

The turbulence model used in the calculations is of crucial importance for modelling flame lengthening due to rotation. The comparison of predictions for the axial temperature profiles given in Fig. 6.2 shows that the standard version of $k - \epsilon$ model yields only a minor increase in the flame length when compared to the non-rotating case, while the modified model predicts a much longer rotating flame (matching experimental observations).

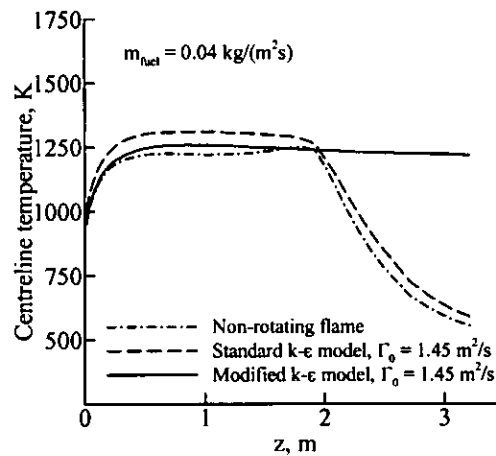


Fig. 6.2. The effect of turbulence modelling on the predicted flame centreline temperature.

Figures 6.3 and 6.4 illustrate the effects of rotation upon the flame's internal structure. When compared to the non-rotating case, Fig. 6.4 demonstrates that flame temperature predicted by the model shows a consistently higher core temperature in the upper regions of the rotating flame. The vortex developed is of Rankine-type of which the magnitude of the angular velocity is proportional to the external circulation (which is in accordance with the approximate theory, see Eq. (4.26)) and it also depends upon the flame heat release rate. In agreement with Eq. (4.25) the radius of the vortex core is not affected by the magnitude of the external circulation imposed.

6. Numerical simulations of whirling flames

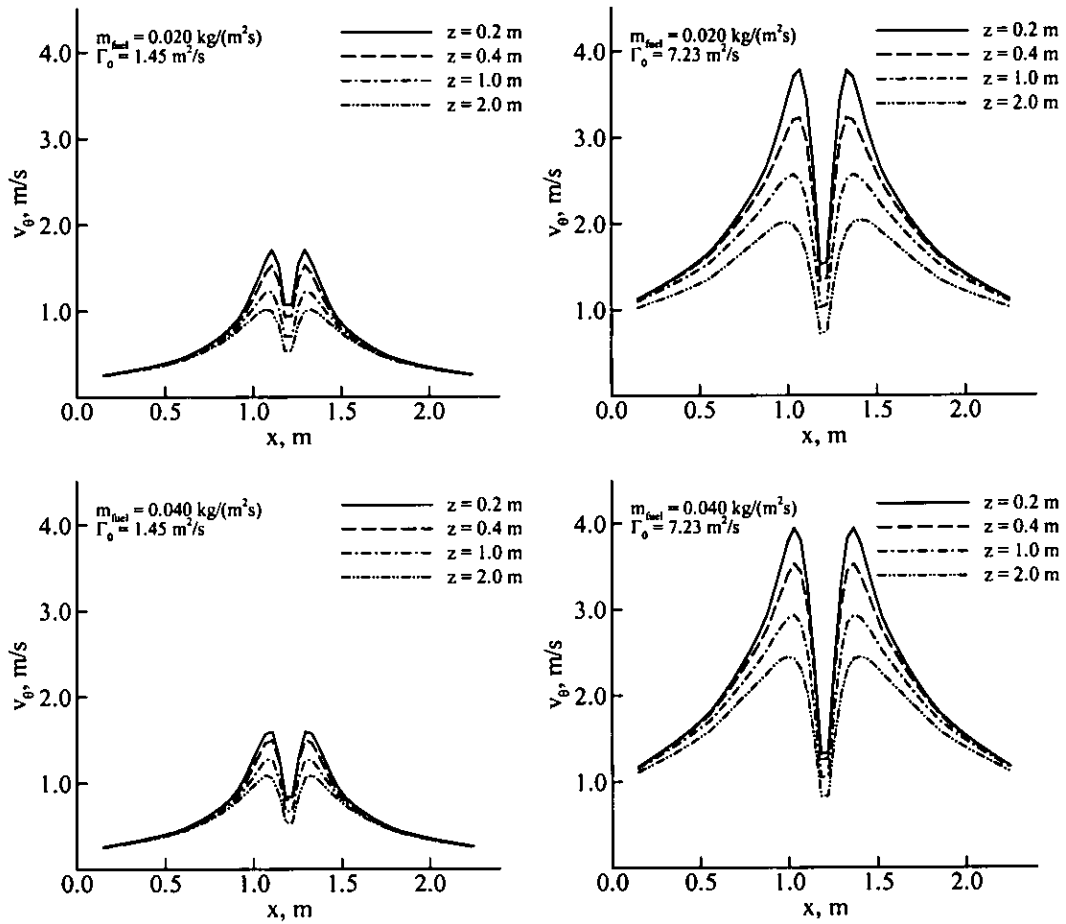


Fig. 6.3. Radial profiles of angular velocity.

Axial profiles of mean temperature and velocity are given in Fig. 6.4. It can be seen, that for flames with relatively low heat release rates (for example, $\dot{m}_{fuel} = 0.020 \text{ kg/(m}^2\text{s)}$, $\dot{Q} = 258 \text{ kW}$), external circulation may cause a decrease in the flame length. Rotating flames with a greater heat release rate (for example, $\dot{m}_{fuel} = 0.040 \text{ kg/(m}^2\text{s)}$, $\dot{Q} = 516 \text{ kW}$) create flame lengths that are significantly longer than their non-rotating counterparts and this can be explained using the results obtained in Chapter Four. Indeed, it has been demonstrated that the externally imparted vorticity is augmented by the rising *accelerating* flow; this being due to the buoyancy induced stretching of the vortex tube, while the vorticity in *decelerating* flow decays due to the expansion of the vortex tube. The accelerating part of the flow is obviously greater for flames with higher heat release rates. As the vorticity is

augmented, the increase of the speed of rotation causes a decrease of turbulent mixing¹ of the fuel with the entrained air, which is modelled using the turbulent viscosity Equation (5.12) and corrected using Eq. (5.15). Less intensive mixing of the reactants requires greater flame surface and, consequently, greater flame length and the opposite effects are obtained in the upper decelerating part of the plume.

For either fuels (or mass burning rates) the imposition of weak circulation initially lengthens the flame (comparing 0.0 m²/s with 1.45 m²/s), but additional circulation can subsequently reduce the flame length (compare 1.45 m²/s with 4.35 m²/s, with 7.23 m²/s); and for the lower heat output the reduction in the high temperature zone is such as to cause this zone to be shorter than was the case with no circulation. However, flame surface area is not dependant upon the flame height alone, but also on the plume diameter.

¹ Note, laminarisation of flame was indicated in the experiments by [Sato and Yang, 1996]

6. Numerical simulations of whirling flames

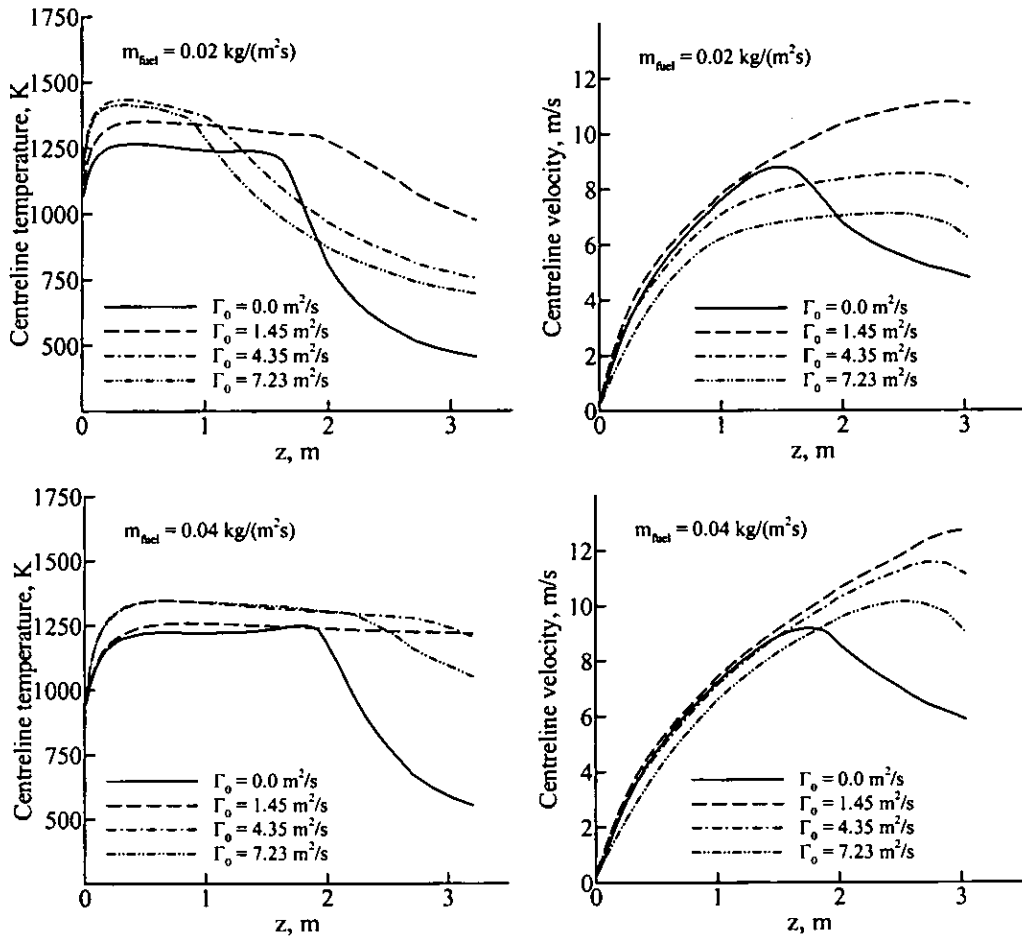


Fig. 6.4. Axial profiles of mean temperature and velocity.

Due to the vortex tube stretching in the rotating flow, the flame becomes narrower and this can be seen in Fig. 6.5, where the predicted radial profiles of mean temperature and velocity (in this case diesel fuel) are presented. The figure compares the effect of circulation upon the flame length and temperature. In the case of no circulation the effects of vorticity show little or no effect upon the predicted radial profiles; however the effects of imposed circulation upon the temperature and velocity are quite clear. The imposed circulation has reduced the turbulent intensity within the flame core resulting in a higher temperature distribution (flame lengthening) coupled with an increase of the vertical velocity of the buoyant plume when compared to a non rotating case.

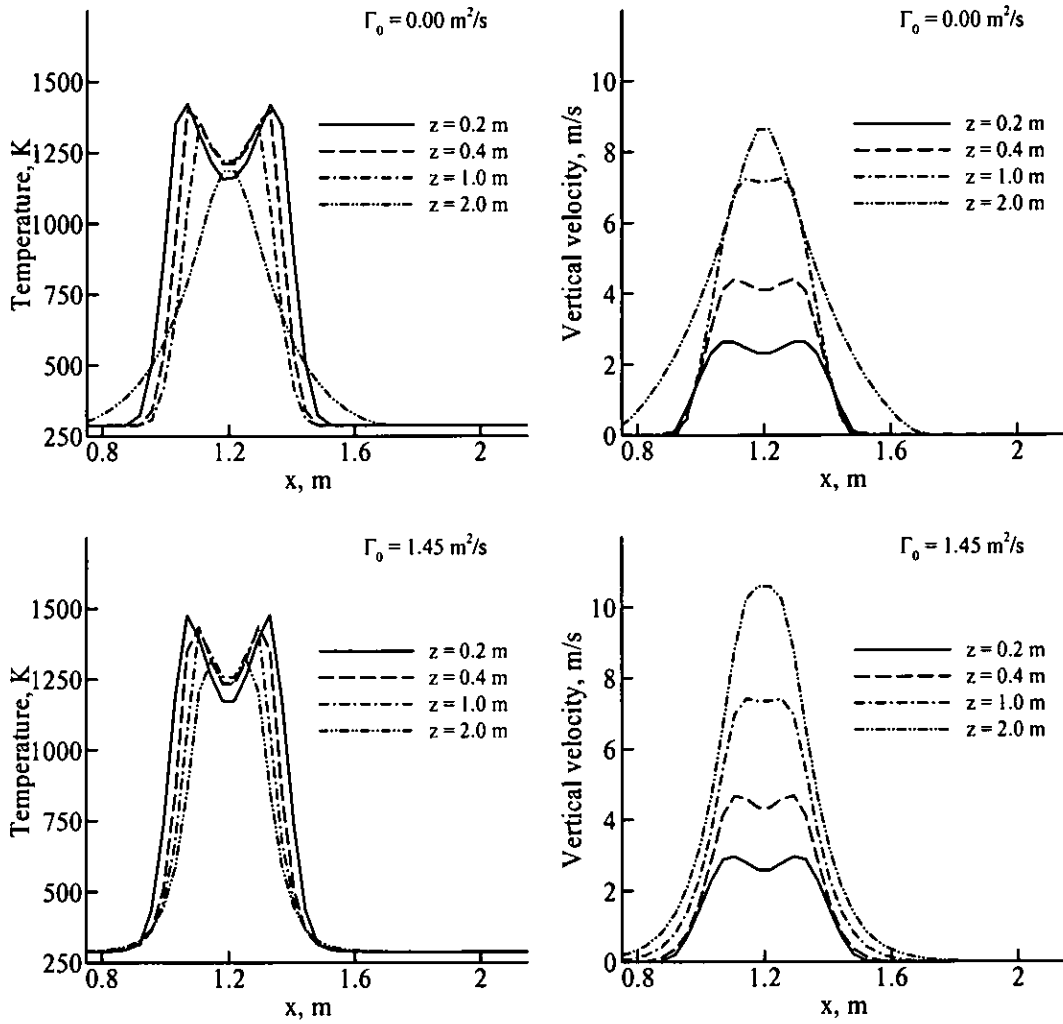


Fig. 6.5. Radial profiles of mean temperature and velocity.

As expected from consideration of a simple rotating flow (see Eq. (4.28)), the swirl number S (calculated here using Eq. (4.37)), was found to be proportional to the imposed circulation Γ_0 and this is demonstrated by Fig. 6.6.

When the swirl number exceeded a value of 0.6, flame shortening was indicated as shown in Fig. 6.1 c. Furthermore, flames with low heat release rates (such as 126 kW flame) became unstable, and steady state conditions were not reached. Note that behaviour of jet swirling flows also exhibits qualitative changes at high degrees of swirl (i.e. when $S > 0.6$ [Gupta et al., 1984]).

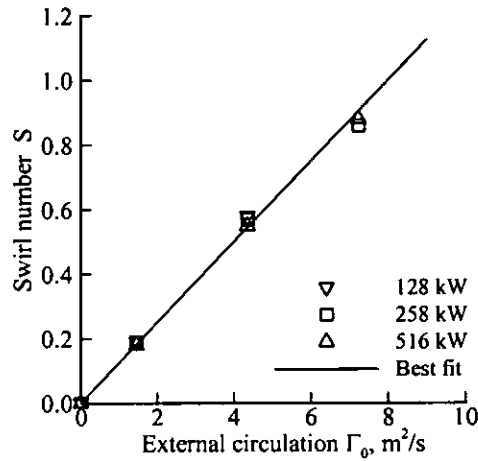


Fig. 6.6. Swirl number of rotating flows versus external circulation.

Fig. 6.7 compares the radiative heat fluxes (obtained by the Monte Carlo method) emitted by the flames and calculated along the vertical line at a distance of 1.2 m from the flame axis. Since the rotating flames are normally thinner than non-rotating counter-parts with the same heat release rate (while their maximum temperatures are approximately the same) the local radiative heat fluxes are reduced when compared to non-rotating case. The change in flame shape also results in some decrease of radiative heat flux incident to the fuel surface and it can therefore be concluded that rotation of the flow within the vortex core alone is not sufficient to provide the experimentally observed increase in burning rate in whirling flames above evaporating pools. However, this rotation may instigate a suitable mechanism not accounted for in the CFD model used here to predict whirling fires in the open space.

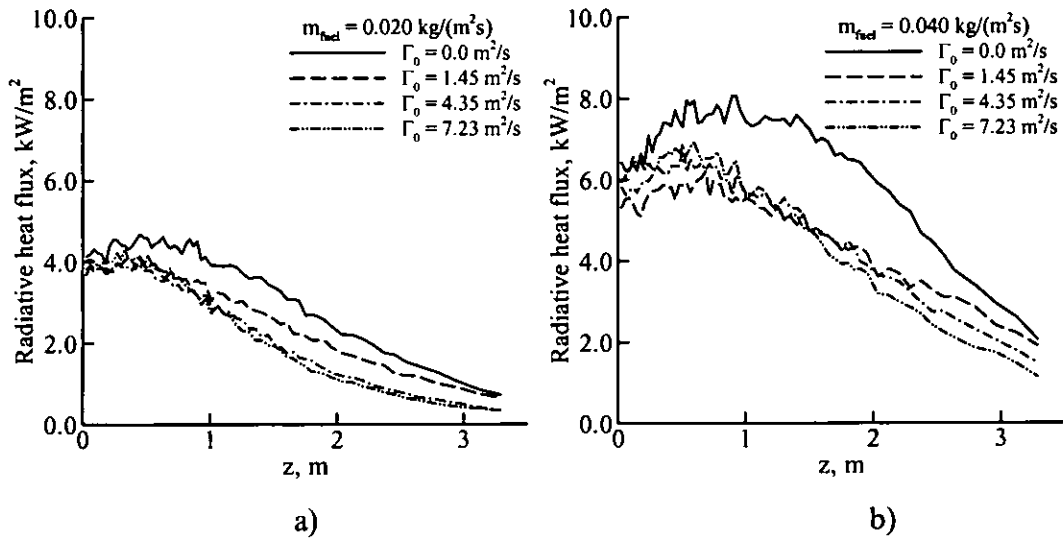


Fig. 6.7. Radiative heat fluxes at a distance of 1.2 m from the flame axis:

a) $\dot{Q} = 258 \text{ kW}$; b) $\dot{Q} = 516 \text{ kW}$.

It can be suggested that the rotation of the flow intensifies the entrainment of the air into the fuel rich region *near the fuel surface*, which may intensify the mixing of the reactants in this area, thus providing greater reaction rates, temperature, radiation emission, and evaporation rate; and possibly moving the reaction zone closer to the fuel surface and it may then reduce the radiation blockage effect at the fuel surface. This is not yet fully understood but is attributed to a participating medium of fuel vapour between the fuel surface and the reaction zone. Fuel rich vapour near the fuel surface blocks reradiated heat from reaching the fuel surface. These phenomena may be a possible mechanism that encourages the observed increase of burning rate due to rotation. It has rarely been considered in modelling studies, but the effects have previously been noted in experimental and theoretical work within the Centre for Fire and Explosion Studies UCLAN. Despite the model not accounting for the radiation blockage of vapour under the reaction zone, the numerical simulations produced results which are in agreement with basic theoretical concepts of rotating flows. The rotation modification to the turbulence model introduced in this work has been shown to be capable in predicting experimentally observed flame elongation when whirling flame develops.

After the analysis of flames in an open space, the model is then applied to simulate whirling flames within the enclosure.

6.2. Simulations of whirling flames in enclosure

6.2.1. Simulations with constant prescribed burning rate

In numerical simulations, the experimental enclosure (see Chapter 3) is reproduced. The computational domain used in the simulations was expanded beyond the enclosure, having the dimensions of 3.4x2.77x3.29 m. A non-uniform rectangular computational mesh consisted of 122880 control volumes (48x40x64 grid nodes). In this section, simulation results are presented for whirling flames modelled with a constant prescribed fuel supply rate this being between 0.010 to 0.040 kg/(m²·s). Covering the time-averaged burning rates measured in the experimental work. Fig. 6.8 demonstrates a representative temperature-velocity field with the flame zone, incoming airflow, hot layer, and the outgoing flows leaving the compartment through the ceiling vent and the doorway. A time instant is shown, when a straight rotating flame is exhausting through the ceiling vent.

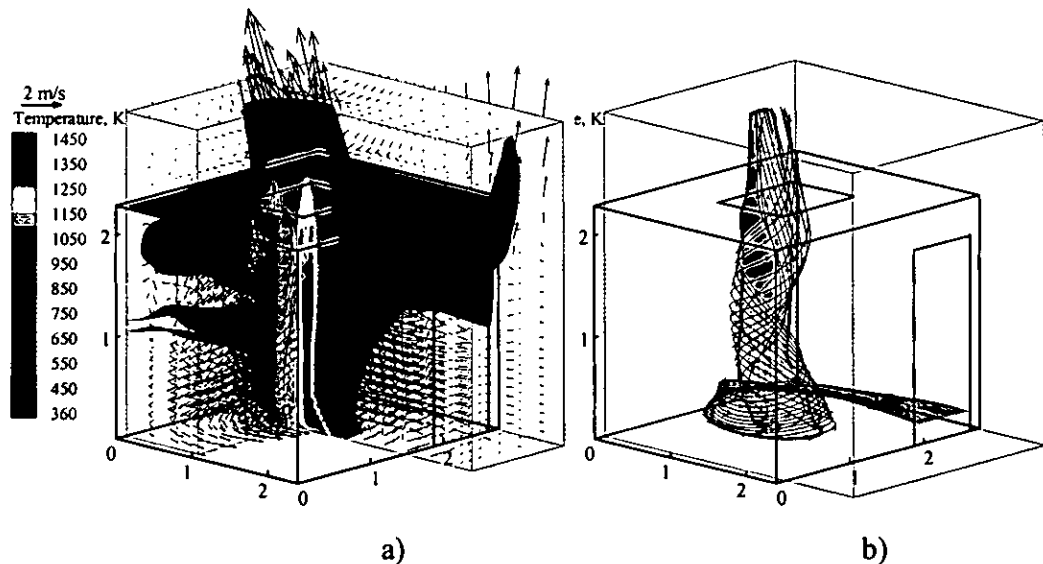


Fig. 6.8. The predicted straight rotating flame exhausting through the ceiling vent: a) mean temperature and velocity fields; b) mean-flow streamlines and 773 K temperature surface (approximates visual flame).

One of the main findings from the numerical simulations of enclosed flames was their intrinsically transient behaviour and unsteadiness. Although the predicted mean temperature, velocity and other fields are identical to that of unconfined flames of the same calorific power and required steady state, the enclosed flames appeared to be unsteady. The unsteadiness manifested itself through the precession of the flame and the periodic formation and destruction of the whirling high-temperature core. As discussed previously, this phenomenon has been also observed in the experimental enclosure. Frame by frame analysis of the predicted flame development has been performed, and different stages have been identified as shown by a sequence of frames taken from video recordings. Temperature and vorticity fields with mean flow streamlines are illustrated in Fig. 6.9 a-f.

Once the whole surface of the fuel is involved the flame is deflected towards the corner near the front wall and no organised rotation occurs (Fig. 6.9a). Later on, the flame zone is driven anti-clockwise by the circulating incoming airflow and driven towards the front wall and consequently to the doorway. The vorticity slowly concentrates around the flame zone (Fig. 6.9b) and then the subsequent vortex core forms resulting in flame lengthening and the formation of a straight, long, thin rapidly rotating flame (Fig. 6.9c, d). The flame and the vortex core coincide at this stage of which the duration of which appears to be relatively short (in the region of 5-10 seconds), depending on the fuel used.

The incoming air inflow displaces the upper part of the flame and the entire vortex core towards the rear corner (Fig. 6.9e). Since the vortex core and the flame no longer coincide, the effects of rotation no longer reduce turbulent mixing of the fuel/air mixture and the flame shortens. Further downstream displacement of the vortex core (Fig. 6.10e) leaves the plume without a source of vorticity. Also, the upper part of the vortex tube is chopped off, because the tube is no longer directed towards the ceiling vent and due to above events the vortex tube finally dissipates, and the non-rotating flame temporarily stabilises as it is deflected to the left wall (Fig. 6.9f). Then the whole cycle repeats itself in a cyclic manner.

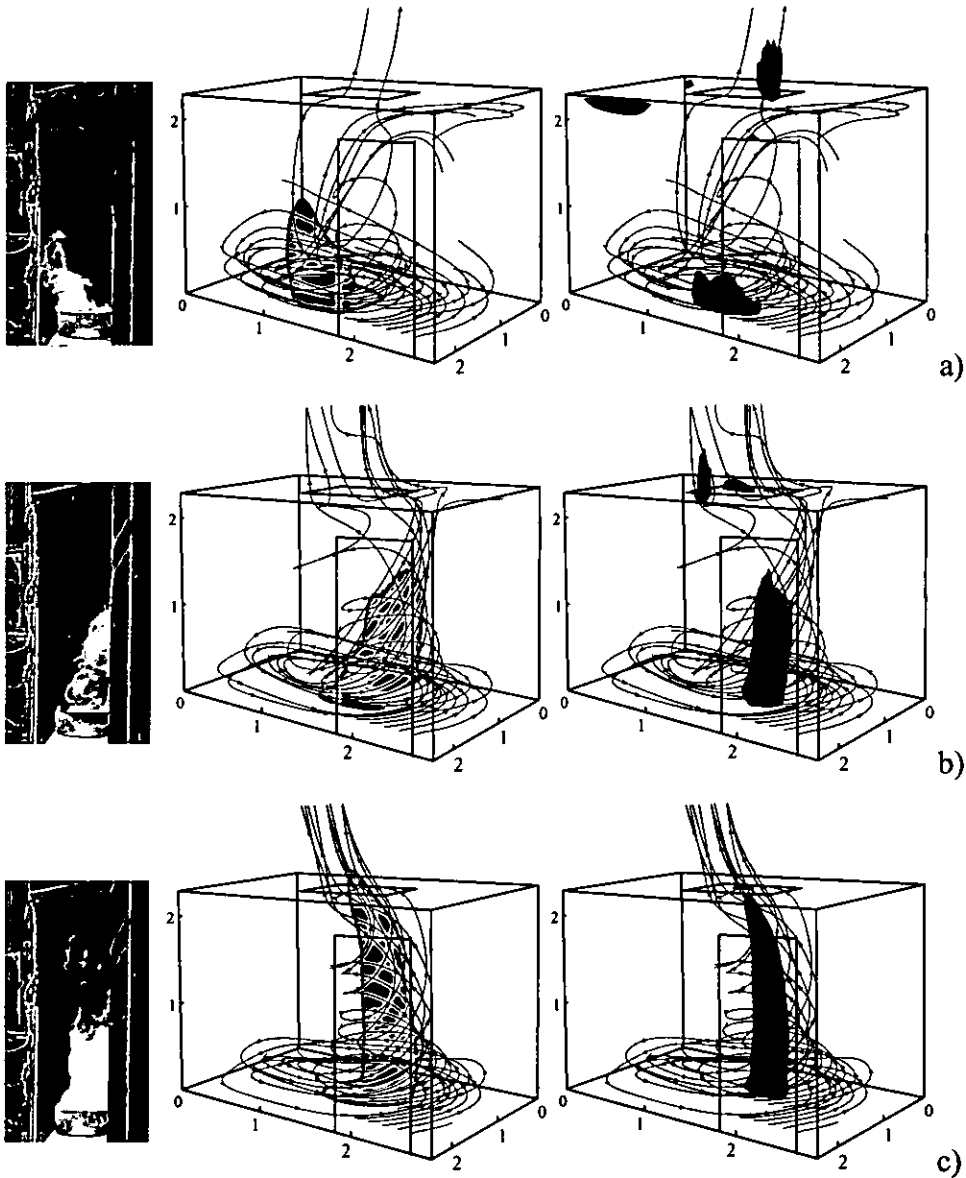


Fig. 6.9. Comparison of observed and predicted flow. From left to right: frames taken from video recordings; surface $T = 773$ K (approximates visual flame zone); surface $\omega_z = 15$ s⁻¹ (location of rotating core). Stages of flame development: a) Flame is deflected towards the rear wall, no regular rotation occur; b) Flame is deflected towards the doorway, whirling zone starts to form; c) Flame lengthens and straightens, vortex core develops.

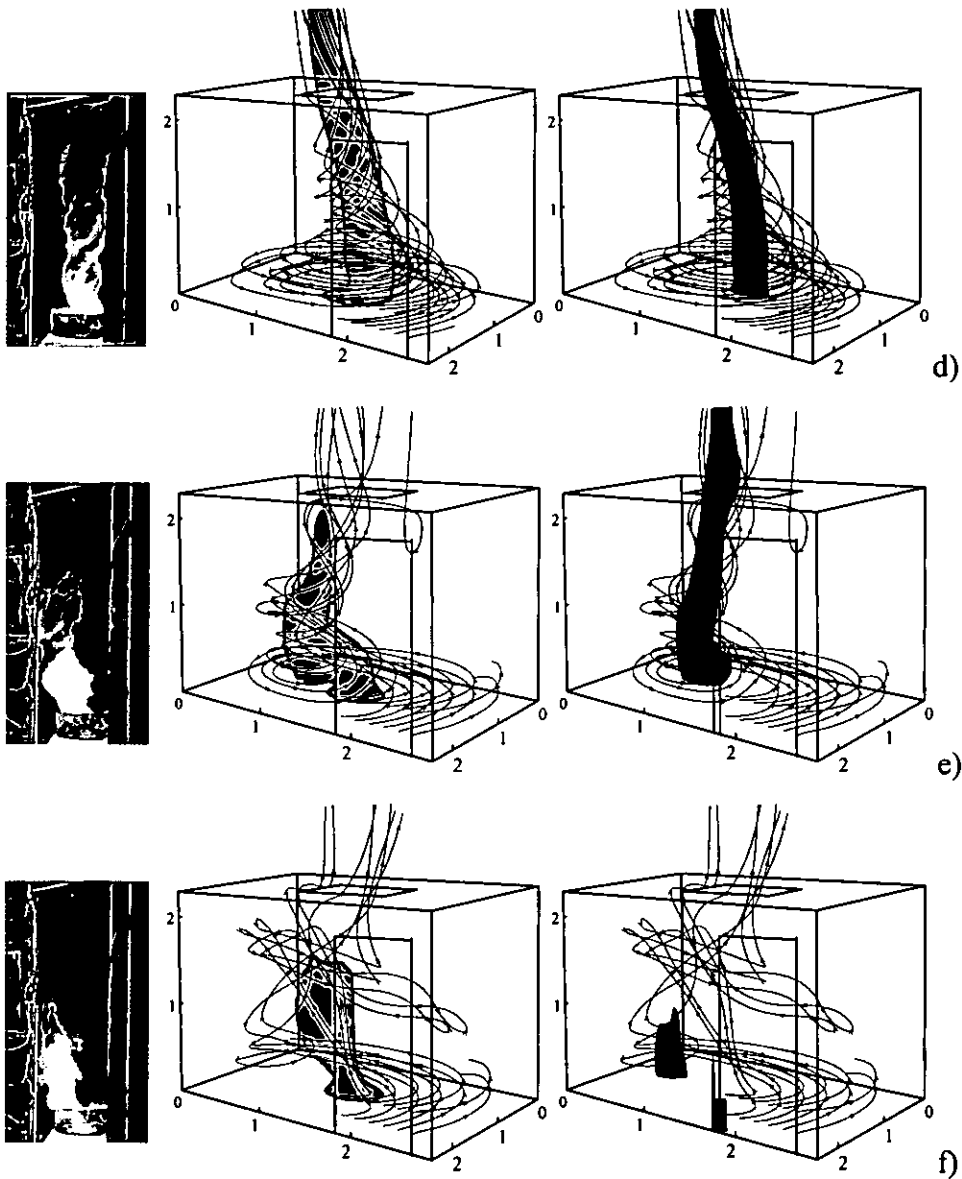


Fig. 6.9 (Continued). d) Flame is straight, it exhausts through the ceiling vent, stretched vortex core erects; e) Upper part of flame is displaced by rotating incoming airflow, the vortex core travels towards the rear wall; f) Similar to a). Streamlines run out from the points at doorway cross-section, at elevations 0.2 and 0.4 m above the floor.

6. Numerical simulations of whirling flames

Thus, the numerical simulations confirmed the reason and the **mechanism of whirling flame instability and quasi-periodic precession**: *the formation of strong whirling flames increases the air inflow into the compartment, which in turn destroys the rotating column.*

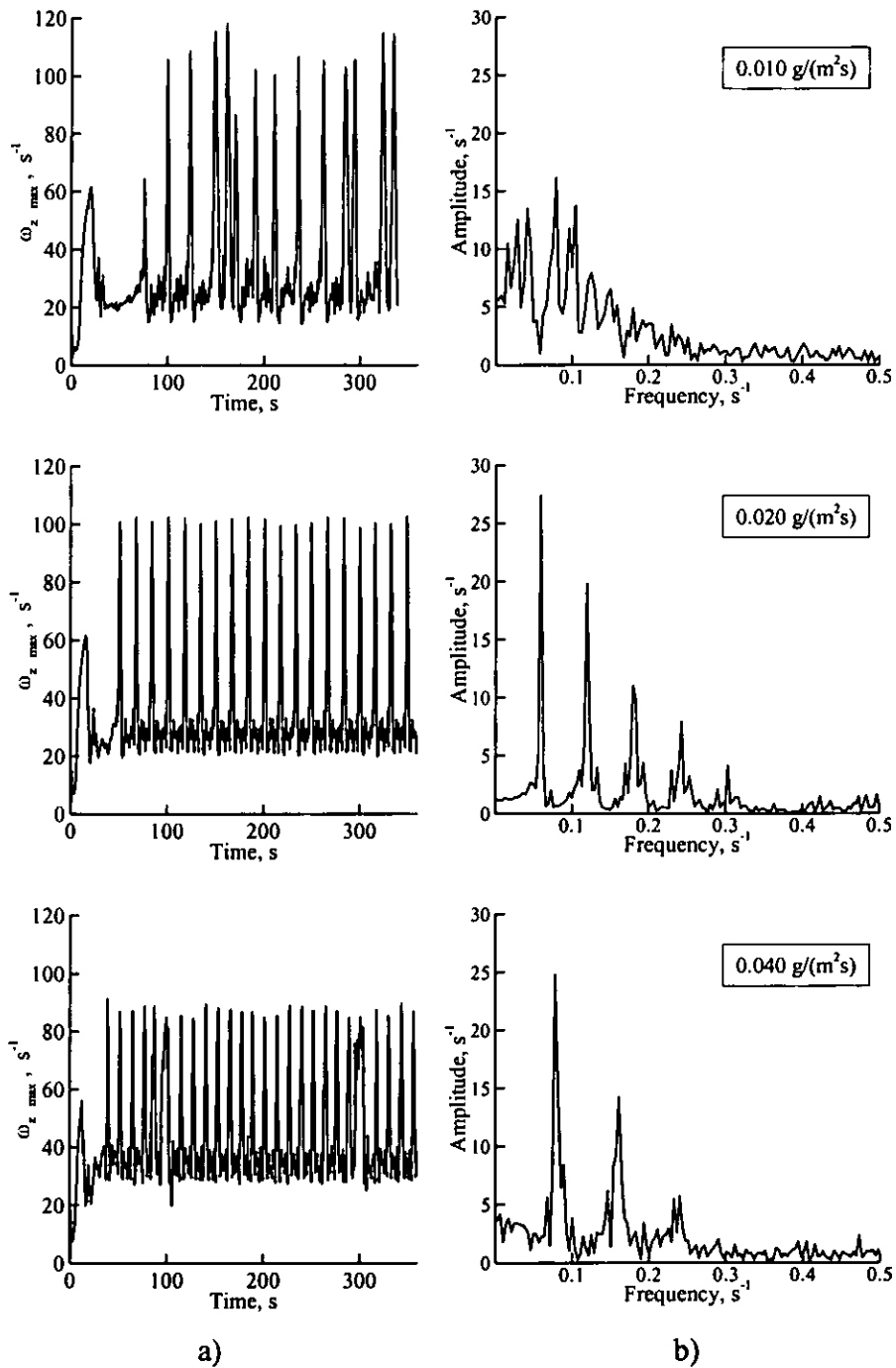


Fig 6.10. Periodic formation and destruction of the vortex core for different burning rates: a) maximum z-vorticity as a function of time; b) spectra of maximum z-vorticity.

Figure 6.10 presents the predicted periodic process by demonstrating the dependence of maximum ω_z in respect to time (Fig. 6.10a); and presents the corresponding spectra (Fig. 6.10b) obtained by Fourier transformation of this dependence. The predicted process is either aperiodic (as that for 10 g/(m²·s)), periodic (for fuel supply rate of 20 g/(m²·s)) or quasi-periodic (40 g/(m²·s)) and this is reflected in the spectra layout. It can also be seen that the dominant frequency for 40 g/(m²·s) is greater than that for 20 g/(m²·s), which is consistent with the experimental observations of flames of fuels with different burning rates. The average period between the formations of a straight whirling flame varied from between 17 s for $\dot{m}_{fuel} = 0.020$ kg/(m²·s) to 12 s for $\dot{m}_{fuel} = 0.040$ kg/(m²·s). These mass loss rates correspond to the measured experimental results obtained for ethanol and heptane fuel and these values can be validated to some extent by the temperature fluctuations recorded in Figures 3.13 and 3.14 respectively. In these figures it is clear that the thermocouple does not remain within the flame core, approximation of the time that the thermocouple remains within the core corresponds to the predicted value numerically simulated.

It is worthy of note that the conclusion about the decrease of the characteristic period as the fuel supply rate increases (i.e. more volatile combustibles are expected to produce a higher frequency of the process) was initially made purely on the basis of computational results (see [Snegirev 2004]). This conclusion is derived from the numerical predictions and later experimentally confirmed when the series of experimental tests had been undertaken as described in Chapter 3 of this work.

6.2.2. Simulations with burning rate coupled with incident heat flux

In this series of simulations, the fuel supply rate was coupled with the heat release rate through the boundary conditions as in equation (5.42). Incident heat flux to the fuel surface is dominated by radiative heat flux in this case being in the order of 65 to 85% in the numerical simulations undertaken. The effects of the cyclic nature of the rotating flame affected the stability of the system in respect to consistent heat flux values. Indeed, once the flame is deflected and tilted, a significant fraction of the radiated heat flux can no longer reach the fuel surface, and is distributed outside

the fuel pan area [Snegirev, 2004]). In this case the fuel evaporation rate from the fuel surface results in a reduced heat release rate in the flame zone. Alternatively, if the flame forms a straight high-temperature rotating column just above the pool, the fraction of radiated heat that reaches the flame surface attains its maximum value. More fuel is evaporated from the surface causing greater heat release and an increase of the distance along which the flow accelerates and the vorticity increases.

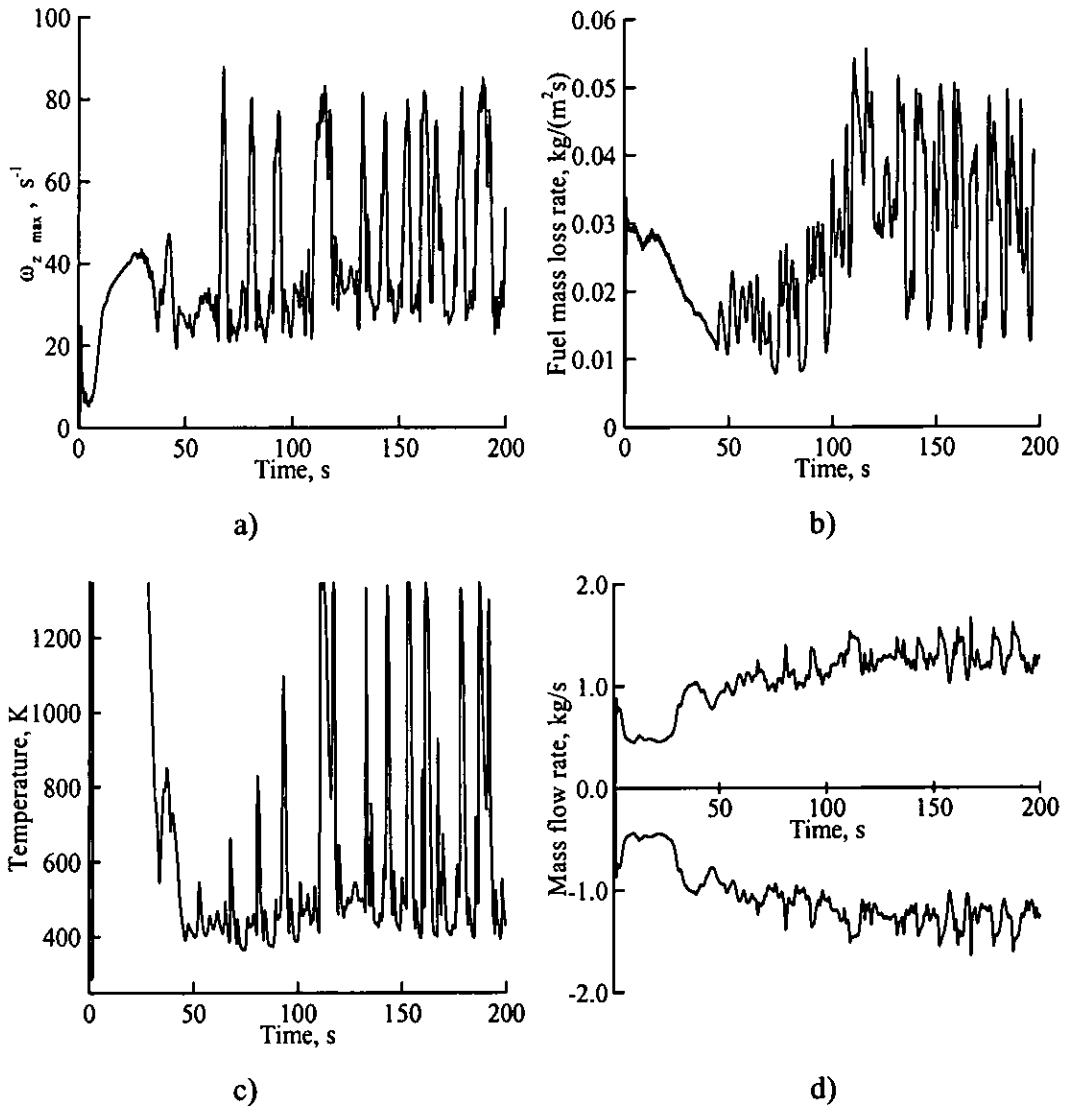


Fig. 6.11. Oscillating flow and combustion in enclosure. Simulations with burning rate coupled with incident heat flux: a) - maximum z-vorticity; b) - fuel mass burning rate; c) - temperature at the centre of the ceiling vent; d) - incoming flow rate through the doorway (lower curve) and outgoing flow rate through the ceiling vent (upper curve).

Computer simulations show that this mechanism leads to an increase in the frequency of the oscillations when compared to a constant fuel supply rate model. Furthermore, similar to experimental observations, the predicted oscillations are now disordered and aperiodic.

This can be seen in Fig. 6.11, where the maximum vorticity, fuel mass burning rate, the temperature at the centre of the ceiling vent, and the incoming (through the doorway) and outgoing (through the ceiling vent) mass flow rates are presented as a function of time. After a transient period of about 100 s (which is longer than that for constant fuel supply rate, see Fig. 6.10), an oscillating regime is established with the period between formations of rotating flames (correspond to spikes in $\omega_{z, \max}(t)$) dependence this being in the order of about 10 to 20 sec. Note the magnitude of variations of the burning rate is rather high: minimum and maximum values are approximately 15 and 50 g/(m²·s) respectively, i.e. a difference of a factor of more than three. The measured average value of the mass burning rate for diesel (see Chapter 3) is 39 g/(m²·s), which indicates reasonable agreement of the measured and predicted values. Unfortunately, the experimental arrangements did not allow the measurements to be made of instant fuel evaporation rate and its variation in time.

6.2.3. The effect of doorway location

As identified in Chapter 4, two necessary conditions namely externally imposed circulation and vertically accelerating flow must be satisfied for flow rotation to occur. The location of the enclosure doorway and the ceiling vent position are very important to produce the conditions required to impose external circulation upon the flame. When the doorway is located asymmetrically, the inflowing air through the doorway provides external circulation for the centrally positioned rising plume and to further prove this conclusion, the simulation was carried out in which doorway was located symmetrically, in the centre of the front wall.

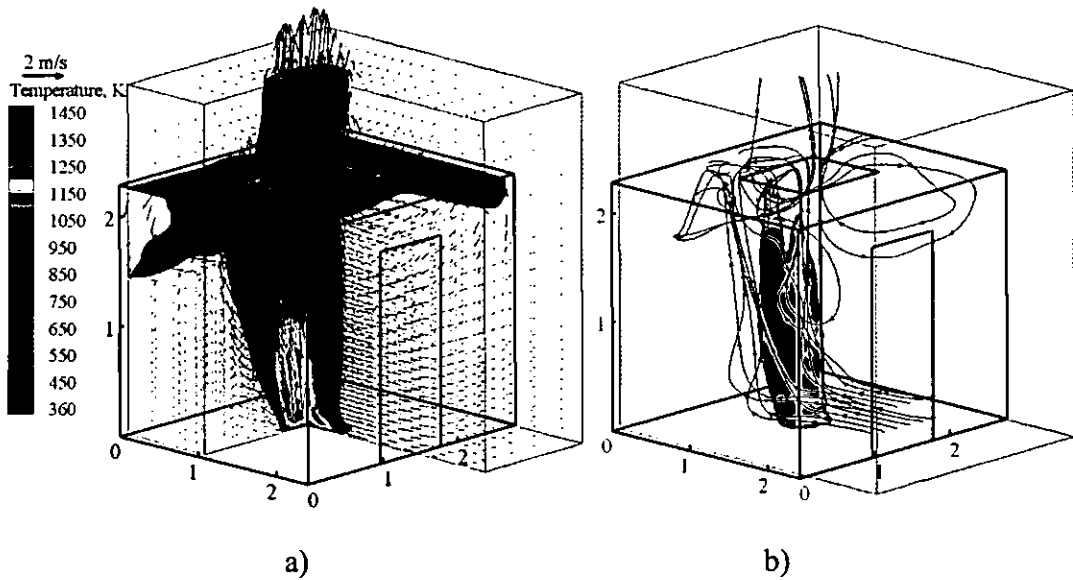


Fig. 6.12. Predicted flame within the enclosure with the symmetrically located doorway: a) mean temperature and velocity fields; b) mean-flow streamlines and 773 K temperature surface (approximates visual flame). Fuel is heptane, mass burning rate is $40 \text{ g}/(\text{m}^2 \cdot \text{s})$.

Figure 6.12 illustrates a representative temperature-velocity field obtained from relocating the doorway. Flame whirling does not develop, and the mechanisms for flame lengthening (the stretching of vortex tube and the inhibition of turbulent mixing) are not therefore activated. As a result, the “ordinary” non-whirling flame is tilted by the incoming airflow, and the flame length is similar to that expected from a ‘normal’ diffusion flame (Eq. (2.5)).

6.3. Validation of the model by experimental results

Prior to use in this work, the model and code described earlier has been exposed to extensive validation studies covering both open and enclosed flames. In particular, buoyant turbulent diffusion flames of propane in still air above a 0.3 m diameter burner were modelled in [Snegirev, 2004]. There, a favourable comparison is presented of the predictions and measurements [Gengembre et al, 1984; Souil et al, 1985] of gas species concentrations, temperature, velocity and their turbulent fluctuations, and radiative heat fluxes obtained in flames with different heat release

rates. Also, predicted the mass burning rates of a liquid fuel (acetone) were found to be in good agreement with the published experimental data [Babrauskas, 1983]. Similar to measurement results, the predicted burning rates were shown to increase with the pool diameter and to reach a constant level for large pool sizes. The examples of modelling of the enclosed flames are the works of [Snegirev et al, 2001; Snegirev et al, 2003], where a comparison is demonstrated of the predictions and experiments within a small-scale enclosure (fire box). In that case, conjugate gas-solid heat transfer at the wall surface (and transient temperature field inside the wall material) was modelled, and the simulated wall surface temperature rise was similar to that measured. In the experimental part of this work, the heat fluxes received by the enclosure walls were measured as described above (see Sections 3.2.5 and 3.4.3), which were also used here for model validation purposes.

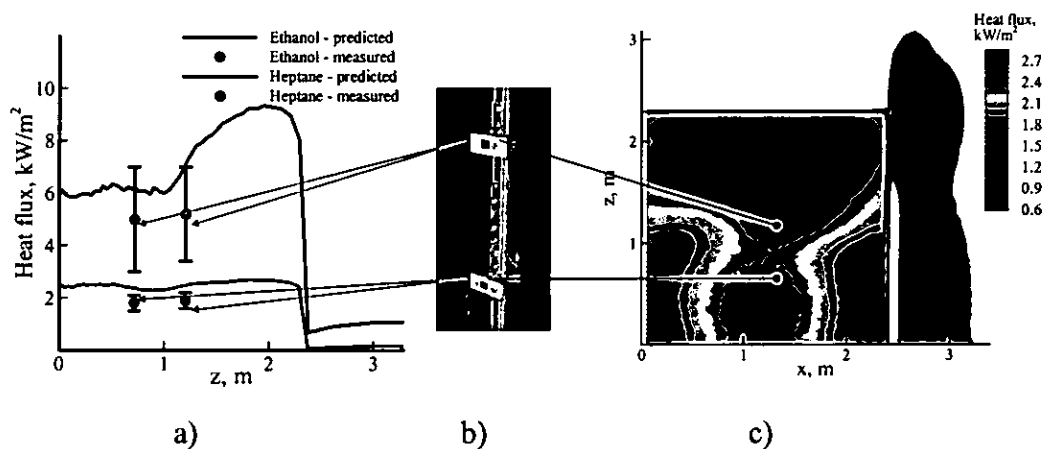


Fig. 6.13. Measurements and predictions of heat flux received by the enclosure wall: a) vertical profiles of total (net radiative and convective) heat fluxes; b) heat flux sensors HFS-3; c) predicted distribution of total heat flux received by vertical plane coinciding with the enclosure wall (fuel is ethanol).

Figure 6.13 depicts a satisfactory comparison of the predicted and measured heat fluxes obtained from the whirling fire within the enclosure. In respect to Ethanol there is reasonable agreement with the experimental and numerical predictions, however in the case of heptane there is a difference. One suggested reason for this discrepancy was the build up of soot on the heat flux sensors during the experimental work.

Good agreement was also obtained in respect to the upper temperature of the whirling plume, peak temperatures of 1200K were recorded by the thermocouple situated at a height of 2.35 meters and this compares with the temperature profiles shown in Fig 6.2 at an equivalent height. Due to periodic nature of the whirling flame the thermocouples did not remain within the flame front and therefore peak flame temperature readings are discussed.

6.4. Conclusions

The 3D CFD model and code *Fire3D* (earlier developed for predictions of buoyant turbulent diffusion flames and modified in this work as described in Chapter 5) is applied to simulate whirling fires both in an open space and within an enclosure. The numerical simulations displayed the development of unconfined rotating flames, the effect of rotation upon flame structure, temperature, and radiative heat output. The formation of a Rankine-type vortex has also been demonstrated. Similar to experimental observations, flame lengthening due to rotation has also been predicted. In accordance with the approximate theory, the flame structure and its response upon the effect of externally imposed circulation were found to depend upon the magnitude of the external circulation and the amount of heat release rate in the flame. The latter determines the length of accelerating part of the flow, where the vorticity is amplified and if the external circulation is imposed then a Rankine-type vortex develops with maximum vorticity (at the axis) and angular velocity (at certain distance away from the axis) proportional to the external circulation. The swirl number of the rotating flow is shown to be proportional to the imposed circulation and at high degrees of swirl, flame shortening and destabilisation was predicted.

Local and maximum radiative heat fluxes from the rotating flames (with constant prescribed fuel supply rate) were found to be less than those in non-rotating flames. This can be attributed to a change in the flame shape (the high temperature radiating flame zone is longer and thinner). It also indicates that additional physical mechanisms should be taken into account to explain and predict the experimentally observed increase in burning rate when the rotation of the flame occurs. A possible mechanism, namely entrainment intensification of the air into the fuel rich region near the fuel surface, has been identified.

Using *Fire3D*, whirling flame development was then simulated within the enclosure that was provided with a ceiling vent and asymmetrically located doorway. Circulating air inflow provided the externally imparted vorticity that was responsible for the formation of a buoyant whirling flame. The geometry of the enclosure represented that of the experimental compartment and similar to experimental observations, predicted whirling fires within the enclosure were found to be transient and intrinsically unstable, although of the unconfined flames of the same heat release rate produced steady-state mean flow fields. The periodic process of formation, precession and destruction of a whirling flame was predicted numerically and interpreted in terms of the conclusions from the existing theory of rotating flows. Experimental data has been used to validate the numerical model in respect to heat flux and temperature and good agreement has been obtained.

The period of oscillations was found to decrease if the fuel supply rate increases. It was therefore concluded that more volatile combustibles should cause a higher frequency process. The predicted period was similar to that observed in experiments and different stages of flame evolution observed in the experiments (Chapter 3) are now predicted numerically. The transient process in which the whirling flame forms and deteriorates is explained in the terms of two necessary conditions required (the imposed circulation and vertical acceleration of the flow) for flow rotation to occur. The flame shape and the flow pattern were compared to those obtained from the video recordings of the experimental flames. The model predictions can therefore be regarded as being in reasonable agreement with the experimental observations of the whirling flame development.

In the predictions the fuel mass loss rate was coupled with the thermal feedback from flame to the fuel surface and the oscillations are found to be more disordered and aperiodic when compared to the simulations with a constant prescribed fuel supply rate.

CHAPTER 7.

CONCLUSIONS AND FUTURE WORK

7.1. Results and conclusions

The formation and behaviour of fire whirls in enclosures has been investigated in this Thesis.

Based on the review of the previous studies of buoyant turbulent diffusion flames, it has been concluded that the behaviour and characteristics of whirling flames are remarkably different when compared to their non-whirling counterparts. Also, buoyant whirling flames were found to be qualitatively different to swirling jet flames, which (due to their intensive use in industry) are carefully studied. Here, substantial gaps in knowledge and understanding have been identified regarding the development and characteristics of medium scale whirling fires in room-size enclosures.

This work included experimental, theoretical, and computational components.

In the *experimental* programme of the research, the experimental apparatus has been designed and constructed to produce whirling flames and to measure their major characteristics. In the experimental enclosure, fire whirls above a fuel pan (located in the centre of the enclosure beneath the ceiling vent) fed with liquid fuel were generated when the airflow (incoming through the asymmetrically located doorway) imposed its circulation onto the flame above the pan. An asymmetrically located

vertical doorway at the front wall, and central ceiling vent appeared to be necessary for the whirling flame to develop.

To justify the measurements of mass burning rates, temperatures and heat fluxes in the case of enclosed whirling fires, an additional series of experiments have been carried out with free-standing non-whirling flames above the same size fuel source. Measured burning rates and flame heights have been compared to the data published in literature; the results obtained have demonstrated fair agreement thus justifying the suitability of the apparatus to undertake experimental studies of whirling fires within enclosures with sufficient accuracy.

Observations of whirling flames in the experimental enclosure have been made, for three liquid fuels namely ethanol, diesel, and heptane. These fuels when burnt within the enclosure exhibit considerably different mass burning rates, when compared to the values for non-whirling flames. Key characteristics, burning rates, temperatures and heat fluxes have been compared to their non-whirling counterparts produced with the same fuel source.

The observations revealed remarkable and distinctive features of whirling flames:

1. Whirling flames in the compartment exhibit much greater burning rates of between 40 to 110%, higher depending on fuel type when compared to their non-whirling counterparts.
2. Whirling flames in the compartment are induced by asymmetrical air flow were always unstable and existed for relatively short period of time (in the order of 10 seconds). The existence of a whirling flame was part of a quasi-periodic process of flame precession accompanied with the formation and destruction of the whirling column. Periodic whirling flames produced large temperature fluctuations.
3. The characteristic period of the process depends upon the fuel burnt. It has been found that the period decreases as the total heat release rate increases.
4. Whirling flames are thinner and much longer than non-whirling ones.
5. Whirling flames within the enclosure produce greater radiative heat fluxes than non-whirling ones in the open space (although the fuel source is the same).

6. During the existence of a whirling flame, the upper smoke layer is completely expelled through the ceiling vent.

To examine the physical mechanisms responsible for whirling flames to develop and the conditions necessary for flame rotation to occur, basic concepts of the existing theory of rotating flows have been applied. By the *theoretical analysis* of the vorticity equation, two necessary conditions have been identified for buoyant rotating flows to develop:

1. non-zero background vorticity (and external circulation) and
2. vertical acceleration of the flow.

The primary mechanism of the vorticity concentration within the vortex core is the stretching of the vortex tube and the latter is balanced by viscous (and possibly turbulent) dissipation. When the above conditions are satisfied, the steady rotating flow was shown to have a radial velocity distribution similar to that of the Rankine vortex; the swirl number of the flow was found to be proportional to the external circulation. In the internal part of Rankine-type vortex, turbulent fluctuations are stabilised by centrifugal force and this explains the reduced turbulent mixing intensity at the boundary of the rotating core.

These results were reproduced by and used in the interpretation of the numerical simulations presented in this work, where the development of a whirling buoyant turbulent diffusion flames were consequently simulated both in the open space and in the enclosure (which corresponds to that used in the experimental studies).

In the *numerical studies*, the RANS version of the CFD model and code *Fire3D* was used. The most important development introduced into the model within this work was the modification to the turbulence model to account for the effect of rotation inhibiting turbulent mixing within the whirling core. The Richardson number was introduced as a controlling criterion, and the C_μ coefficient was made dependent upon the Richardson number in such a way which reduces turbulent viscosity in the whirling core.

As a part of the validation studies, the model and code were examined in its capability to predict radiant heat fluxes and upper flame temperatures in accordance with the data obtained from the flames produced experimentally in this work. Reasonable agreement has been obtained between the experimental and numerically predicted values for the heat fluxes at the enclosure wall coupled with plume temperatures.

In the numerical simulations of unconfined rotating flames, the effect of rotation upon the flame structure, temperature, and radiative output has been demonstrated. The formation of a Rankine-type vortex has also been demonstrated and similar to experimental observations; flame lengthening due to rotation has been predicted. In accordance with the approximate theory, the flame structure and its response to the externally imposed circulation were found to depend upon the magnitude of the external circulation and on heat release rate within the flame. The latter determines the length of the accelerating part of flow, where the vorticity is amplified. If the external circulation is imposed then the Rankine-type vortex develops with maximum vorticity at the axis and maximum angular velocity at a certain distance away from the axis, both being proportional to the external circulation. The swirl number of the rotating flow is shown to be proportional to the imposed circulation; at high degrees of swirl, flame shortening and destabilisation was predicted.

Using *Fire3D*, the whirling flame development was then simulated within the enclosure with a ceiling vent and asymmetrically located doorway. The geometry of the enclosure represented that of the experimental compartment. Similar to experimental observations, predicted whirling fires produced in the enclosure were found to be transient and intrinsically unstable, although unconfined flames of the same heat release rate produced steady-state mean flow fields. The aperiodic process of formation, precession and destruction of the whirling flame was predicted numerically and interpreted in terms of the conclusions from the existing theory of rotating flows.

The predicted characteristic period of the process was similar to that observed in the experiments. The period was found to decrease if the (*constant prescribed*) fuel supply rate (given type of fuel) increases. In the predictions with fuel mass loss rate *coupled* with the thermal feedback from flame to the fuel surface, the oscillations are

found to be more disordered and aperiodic when compared to the simulations with constant prescribed fuel supply rate. Different stages of flame evolution observed in the experiments have been demonstrated by numerical simulations. The flame shape and the flow pattern were compared to those obtained from the video recordings of the experimental flames, and the model predictions were found in reasonable agreement with the experimental observations of the whirling flame development and destruction. It has been shown, that the transient process in which the whirling flame forms and deteriorates can be explained in terms of two necessary conditions (the imposed circulation and vertical acceleration of the flow) for flow rotation to occur.

Buoyant whirling flames were shown both experimentally and by numerical simulations to be considerably longer than those in ordinary free-standing or wind-blown fires, and they exhibited much greater burning rates, increased total heat release and radiative output and a qualitatively different behaviour of the smoke layer within the enclosure.

The above listed results indicate that *the overall aim and specific objectives of this work have been met.*

The *novelty* of this work includes:

1. New experimental data on the formation and dynamics of whirling flames in enclosure of medium (room-size) scale.
2. Identification of the physical mechanisms and necessary conditions for buoyant rotating flames to develop in the enclosure fires.
3. Improvements to the CFD model and code to account for the effect of flow rotation on turbulence.
4. Results and analysis of the numerical simulations, in which (i) the effect of flow rotation on turbulence, (ii) radiative transfer, and (iii) coupling of fuel burning rate with heat flux received by the fuel surface were simultaneously accounted for.

From a *practical* point of view, the new knowledge obtained in this work may potentially be used in development of efficient fire mitigation techniques that will counter the possible threat presented by fire whirls. The increased mixing and

entrainment (leading to greater burning rate) implies a possible use of deliberately created enclosure vents and suspended extinguishing media to interfere with the reaction taking place. A similar fire fighting technique is implied by the tendency of the fire whirl to exhaust the smoke layer. However, it is in the assessment of and possible modification to design calculations that this work has the most potential for practical use, bearing in mind the greater intensity of the burning when compared to commonly used non rotating design fires used in the fire engineering industry, and the consequent increase in the flame length when compared to a non rotating flame.

7.2. Future Work

Future work in this area could include improvements both in modelling and experimental performance.

In modelling studies:

- 1 Large-eddy simulation techniques may be usefully employed for turbulence modelling.
- 2 A more refined and theoretically sound combustion model, based on probability density function approach, can be incorporated.
- 3 A more robust methodology to resolve spectral properties of thermal radiation could be applied.
- 4 Higher order accuracy numerical algorithms could be used in numerical studies of the transient process.
- 5 Grid resolution could be enhanced.
- 6 In particular air entrainment and mixing with fuel vapour could be closely considered near the fuel surface to explain and to reproduce the experimentally observed increase of burning rate in case of flow rotation, taking the effects of the freeboard into account and the participating medium under the reaction zone.

Some work within these avenues is currently in progress, as demonstrated in the recent paper [Snegirev et al, 2004].

In experimental studies:

- 1 Transient measurements of the burning rates would provide more detailed quantitative information on the process.
- 2 Studies using a wider range of fuels and sizes of fuel source, as well as of different geometries of the enclosure would be helpful in further justification and refinement of the conclusions derived in this work.

However, the work conducted for this Thesis has demonstrated the advantages of the CFD code '*Fire 3D*' which could be used to further study quantifiable limits to the geometrical arrangements and fluid dynamic conditions for fire whirls to develop.

REFERENCES

1. Abbas A.S., Lockwood F.C. (1985) Note: Prediction of Soot Concentrations in Turbulent Diffusion Flames. *Journal of the Institute of Energy*, **58**, 112-115.
2. Abujelala M.T., Lilley D.G. (1984) Limitations and Empirical Extensions of the k-e Model as Applied to Turbulent Confined Swirling Flows. *Chemical Engineering Communications*, **31**, 223-236.
3. Adiga K.C., Ramaker D.E., Tatem P.A., Williams F.W. (1989) Modelling Pool-Like Gas Flames of Propane. *Fire Safety Journal*, **14**, 4, 241-250.
4. Adiga K.C., Ramaker D.E., Tatem P.A., Williams F.W. (1989) Modelling Thermal Radiation in Open Liquid Pool Fires. *Proc. of the 2nd Int. Symposium on Fire Safety Science*, IAFSS, pp. 241-250.
5. Batchelor G.K. (1967) *An Introduction to Fluid Dynamics*. Cambridge University Press.
6. Babrauskas V. (1983) Estimating Large Pool Fire Burning Rates. *Fire Technology*, **19**, 4, 251-261.
7. Babrauskas V. (1996) *Heat Release in Fires*. V. Babrauskas, S.J. Grayson (Eds), E&FN SPON, pp. 201-206.
8. Battaglia F., McGrattan K.B., Rehm R.G., Baum H.R. (2000) Simulating Fire Whirls. *Combustion Theory and Modelling*, **4**, 2, 123-138.
9. Battaglia F., Rehm R.G., Baum H.R. (2000) The Fluid Mechanics of Fire Whirls: an Inviscid Model. *Physics of Fluids*, **12**, 11, 2859-2867.
10. Beer J.M., Chigier N.A. (1972) *Combustion Aerodynamics*. Wiley.
11. Beer J.M., Chigier N.A., Davies T.W., Bassindale K. (1971) Laminarisation of Turbulent Flames in Rotating Environments. *Combustion and Flame*, **16**, 39-45.
12. Beyler C.L. (2002) Fire Hazard Calculations for Large, Open Hydrocarbon Fires. In: *SFPE Handbook of Fire Protection Engineering, 3rd Ed.*, NFPA, pp 3/268 – 3/314.
13. Blinov V.I., Khudiakov G.N. (1961) *Diffusion Burning of Liquids*. US Army Translation, NIIS No. AD2966762.

14. Blundson C.A., Beeri Z., Malalasekera W.M.G., Dent J.C. (1996) Comprehensive Modelling of Turbulent Flames with the Coherent Flame-Sheet Model 1. Buoyant Diffusion Flames. *Journal of Energy Resources Technology - Transactions of the ASME*, **118**, 1, 65-71.
15. Brohez. S., Delvosalle. C., Marlair. G. (2004) A Two-thermocouples Probe for Radiation Corrections of Measured Temperatures in Compartment Fires. *Fire Safety Journal*, **39**, 399- 411.
16. Brosmer M. A; Tien C. L. (1987) Radiative Energy Blockage in Large Pool Fires. *Combustion Science and Technology*, **51**, 21 – 37.
17. Byram G.M, Martin E. (1962) Fire Whirl Winds in the Laboratory. *Fire Control Notes*, pp 13-17.
18. Capener E.L., Alger R.S. (1972) Characterisation and Suppression of Aircraft and Fuel Fires, WSCI 72 – 76. *Western States section meeting of the Combustion Institute*, Monterey, CA.
19. Cha M.S., Lee D.S., Chung S.H. (1999) Effect of Swirl on Lifted Flame Characteristics in Non-premixed Flames. *Combustion and Flame*, **117**, 3, 636-645.
20. Chang K.-C., Chen C.-S. (1993) Development of a Hybrid k-e Turbulence Model for Swirling Re-circulating Flows under Moderate to Strong Swirl Intensities. *International Journal for Numerical Methods in Fluids*, **16**, 5, 421-443.
21. Chen C.-S., Chang K.-C. (1995) Modification of the k-e Turbulence Model for Swirling Re-circulating Flow in a Pipe Expansion. *International Journal of Computational Fluid Dynamics*, **5**, 3-4, 263-279.
22. Cheng T.S., Chao Y.-C., Wu D.-C., Hsu H.-W., Yuan T. (2001) Effects of Partial Premixing on Pollutant Emissions in Swirling Methane Jet Flames. *Combustion and Flame*, **125**, 865-878.
23. Chigier N.A., Beer J.M., Grecov D., Bassindale K. (1970) Jet Flames in Rotating Flow Fields. *Combustion and Flame*, **14**, 171-180.
24. Chitty R., Kumar S. (2004) Building Separation Calculations Revisited using advanced Fire Models. *Proc. of the 10th Int. Conference Interflam2004*, Vol. 1, pp. 447-458.
25. Chuang S.-H., Yang C.-S., Wu N.-J. (1999) Predictions of Swirling Flow in a Sudden-expansion Dump Combustor with Flame-holder Side-inlet using Two-step

References

- Combustion Model. *International Journal of Numerical Methods for Heat and Fluid Flow*, **9**, 7, 764-787.
26. Clune, D.D, Koenig L.N. (1983) The Transient Growth of an Unconfined Pool Fire. *Fire Technology*, **19**, 3, 149 – 162.
27. Coelho P.J., Carvalho M.G. (1995) Modeling of Soot Formation and Oxidation in Turbulent Diffusion Flames. *Journal of Thermophysics and Heat Transfer*, **9**, 644-652.
28. Conway S., Caraeni D., Fuchs L. (2000) Large Eddy Simulation of the Flow through the Blades of a Swirl Generator. *International Journal of Heat and Fluid Flow*, **21**, 5, 664-673.
29. Cox G. (1995) Compartment Fire Modelling. In: *Combustion fundamentals of fire*, G. Cox (Ed.), Academic Press, pp. 329-404.
30. Cox G., Kumar S. (1987) Field Modelling of Fire in Forced Ventilated Enclosures. *Combustion Science and Technology*, **52**, 7-23.
31. Cox G., Kumar S. (1989) Radiation and Surface Roughness Effects in the Numerical Modelling of Enclosure Fires. *Proc. of the 2nd Int. Symposium on Fire Safety Science*, IAFSS, pp. 851-860.
32. Cox G., Kumar. S, Markatos N.C. (1986) Some Field Model Validations Studies. *Proc. of the 1st Int. Symposium on Fire Safety Science*, IAFSS, pp. 159-171.
33. De Ris J. (1978) Fire Radiation. a Review. *Proceedings of the Combustion Institute*, **17**, 1003-1016.
34. Drysdale D. (1999). *An Introduction to Fire Dynamics*. 2nd Ed., Wiley, Chichester.
35. Emmons H.W, Ying S.J. (1966) The Fire Whirl. *Proceedings of the Combustion Institute*, **11**, 475–488.
36. Ewer J.A.C., Galea E.R., Patel M.K., Knight B. (1999) The Development and Application of Group Solvers in the SMARTFIRE Fire Field Model. *Proceedings of the Eighth International Conference INTERFLAM'99*, Vol. 2, pp. 939-950.
37. Falco R.E. (1977) The Effect of Swirl on the Turbulence Structure of Jets. Turbulence in Internal Flows. In: *Turbo-machinery and Other Engineering Applications*. S.N.B. Murthy (ed.) Hemisphere Publ. Corp., Washington, 1977, pp. 113-124.
38. Faltsi-Saravelou O., Wild P., Sazhin S.S., Michel J.E. (1997) Detailed Modelling of a Swirling Coal Flame. *Combustion Science and Technology*, **123**, 1-6, 1-22.

References

39. Farouk B., McGrattan K.B., Rehm R.G. (2001) Large Eddy Simulation of Naturally Induced Fire Whirls in a Vertical Square Channel with Corner Gaps *Proceedings of the International Mechanical Engineering Congress and Exposition (IMECE)*, 2000. Presented Paper. Modelling and Numerical Simulation of Combustion Processes Session.
40. Fernando H.J.S., Smith D.C. (2001) Vortex Structures in Geophysical Convection. *European Journal of Mechanics. B - Fluids*, **20**, 437-470.
41. Ferziger J.H., Peric M. (1999) *Computational Methods in Fluid Dynamics*, Springer-Verlag, Berlin.
42. Fleischmann C.M., McGrattan K.B. (1999) Numerical and Experimental Gravity Currents Related to Backdrafts. *Fire Safety Journal*, **33**, 1, 21-34.
43. Fu S., Huang P.G., Launder B.E., Leschziner M.A. (1988) A Comparison of Algebraic and Differential Second-Moment Closures for Axisymmetric Turbulent Shear Flows With and Without Swirl. *Journal of Fluids Engineering - Transactions of the ASME*, **110**, 216-221.
44. Galea E.R., Markatos N.C. (1989) Modelling of Aircraft Cabin Fires. *Proc. of the 2nd Int. Symposium on Fire Safety Science*, IAFSS, pp. 801-810.
45. Gengembre E., Cambray P., Karmed D., Bellet J.C. (1984) Turbulent Diffusion Flames with Large Buoyancy Effects, *Combustion Science and Technology*, **41**, 55-67.
46. Gradinger T.B., Inauen A., Bombach R., Kappeli B., Hubschmid W., Boulouchos K. (2001) Liquid-Fuel/Air Premixing in Gas Turbine Combustors: Experiment and Numerical Simulation. *Combustion and Flame*, **124**, 3, 422-443.
47. Gottuk D.T., White D.A. (2002) Liquid Pool Fires. In: *SFPE Handbook of Fire Protection Engineering*, 3rd Ed., NFPA, pp 2/297 – 2/316.
48. Gupta A.K., Lilley D.G., Syred N. (1984) *Swirl Flows*. Abacus Press.
49. Hayasaka H. (1996) Radiative Characteristics and Flame Structure of Small-Pool Flames. *Fire Technology*, **32**, 4, 308-322.
50. Heskestad G. (1986) Fire Plume Air Entrainment According to Two Competing Assumptions. *Proceedings of the Combustion Institute*, **21**, 111 – 120.
51. Hirsch C. (1988) *Numerical Computation of Internal and External Flows*, Vol. 2, Wiley.

References

52. Hogg S., Leschziner M.A. (1989) Computation of Highly Swirling Confined Flow with a Reynolds Stress Turbulence Model. *AIAA Journal*, **27**, 1, 57-63.
53. Hopfinger E.J., van Heijst G.J.F. (1993) Vortices in Rotating Fluids. *Annual Review of Fluid Mechanics*, **25**, 241-289.
54. Hottel H.C. (1958) Review – Certain Laws Governing Diffusive Burning of Liquids by V.I. Blinov and G.N. Khudiakov. *Fire Research Abstracts and Reviews*, **1**, 41 – 44.
55. Hua J., Wang J., Kumar K., Kumar S. (2004) Evaluation of The Combustion and Thermal Radiation Modelling Methods for Fuel and Ventilation-controlled Compartment Fires. *Proc. of the 10th Int. Conference Interflam2004*, Vol. 1, pp. 787-794.
56. Hurst-Clark N.M., Ewer J.A.C., Grandison A.J., Galea E.R. (2004) Group solvers: a Means of Reducing Run-times and Memory Overheads for CFD Based Fire Simulation Software, *Proc. of the 10th Int. Conference Interflam2004*. Vol. 1, pp. 659-664.
57. Imao S., Itoh M., Harada T. (1996) Turbulent Characteristics of the Flow in an Axially Rotating Pipe. *International Journal of Heat and Fluid Flow*, **17**, 5, 444-451.
58. Jia F., Galea E.R., Patel M.K. (1997) The Prediction of Fire Propagation in Enclosure Fires. *Proc. of the 5th Int. Symposium on Fire Safety Science*, IAFSS, pp. 439-450.
59. Jia F., Patel M.K., Galea E.R. (2004) CFD Fire Simulation of the Swissair Flight 111 in-Flight Fire, *Proc. of the 10th Int. Conference Interflam2004*, Vol. 2, pp. 1195-1206.
60. Jones W.P., (1984) Turbulence Modelling and Numerical Solution Methods for Variable Density and Combusting Flows. In: *Turbulent Reacting Flows*, P.A. Libby, F.A. Williams (Eds.). Academic Press, 1994.
61. Jones W.P., Pascau A. (1989) Calculation of Confined Swirling Flows with a Second Moment Closure. *Journal of Fluids Engineering - Transactions of the ASME*, **111**, 248-255.
62. Joulain P. (1998) The Behaviour of Pool Fires: State of the Art and New Insights. *Proceedings of the Combustion Institute*, **27**, 2691-2706.

63. Kerrison L., Mawhinney N., Galea E.R., Hoffmann N., Patel M.K. (1994) A Comparison of Two Fire Field Models with Experimental Room Fire Data. *Proc. of the 4th Int. Symposium on Fire Safety Science*. IAFSS, pp. 161-172.
64. Korn G.A., Korn T.M. (1968) *Mathematical Handbook*, McGraw-Hill.
65. Kumar S., Gupta A.K., Cox G. (1991) Effects of Thermal Radiation on the Fluid Dynamics of Compartment Fires. *Proc. of the 3rd Int. Symposium on Fire Safety Science*, IAFSS, pp. 345-354.
66. Kumar S., Heywood G., Liew S. (1997) Superdrop Modelling of a Sprinkler Tray in a Two-phase CFD - particle Tracking Model. *Proc. of the 5th Int. Symposium on Fire Safety Science*, IAFSS, pp. 889-900.
67. Kuo K.K. (1986) *Principles of Combustion*, Wiley.
68. Kurose R., Makino H., Suzuki A. (2004) Numerical Analysis of Pulverised Coal Combustion Characteristics using an advanced Low-Nox Burner. *Fuel*, **83**, 693-703.
69. Lai Y.G. (1996) Predictive Capabilities of Turbulence Models for a Confined Swirling Flow. *AIAA Journal*, **34**, 8, 1743-1745.
70. Launder B.E., Spalding D.B (1972) *Mathematical Models of Turbulence*. Academic Press, London.
71. Lei Y., Zhang J., Zhou L. (2000) Simulation of Swirling Turbulent Flows of Coaxial Jets in a Combustor. *Numerical Heat Transfer, Part A: Applications*, **37**, 2, 189-199.
72. Leschziner M.A., Rodi W. (1981) Calculation of Annular and Twin Parallel Jets Using Various Discretization Schemes and Turbulent-Model Variations. *Journal of Fluid Engineering – Transactions of the ASME*, **103**, pp. 353-360.
73. Lewis M.J., Moss M.B., Rubini P.A. (1997) CFD Modelling of Combustion and Heat Transfer in Compartment Fires. *Fire Safety Science - Proceedings of the Fifth International Symposium*. IAFSS, pp. 463-474.
74. Lewis M.J., Rubini P.A., Moss J.B. (2000) Field Modelling of Non-Charring Flame Spread. *Proc. of the 6th Int. Symposium on Fire Safety Science*, IAFSS, pp. 684-694.
75. Li G., Rubini P.A., Moss J.B. (1999) Performance Assessment of Numerical Simulations for Glazing Temperatures in a Compartment Fire. *Proceedings of the eighth international conference INTERFLAM'99*, Vol. 2, pp. 1195-1200.

76. Lois E., Swithenbank J. (1978) Fire Hazards in Oil Tank Arrays in a Wind. *Proceedings of the Combustion Institute*, **17**, 1087–1098.
77. Magnussen B.F., Hjertager B.H. (1977) On Mathematical Modeling of Turbulent Combustion with Special Emphasis on Soot Formation and Combustion, *Proceedings of the Combustion Institute*, **16**, 719-728.
78. Mammoser J.H.III, Battaglia F. (2004) A computational study on the use of balconies to reduce flame spread in high-rise apartment fires. *Fire Safety Journal*, **39**, 4, 277-296.
79. Markstien G.H. (1978) Radiative properties of Plastic Fires. *Proceedings of the Combustion Institute*, **17**, 1053-1062.
80. Marracino B., Lentini D. (1997) Radiation modelling in Non-Luminous Nonpremixed Turbulent Flames, *Combustion Science and Technology*, **128**, 23-48.
81. Marsden J.A. (2000) Rotating Fire Plumes. *Research Seminar No 60 of the Centre for Research in Fire and Explosion Studies*, 15 June 2000, UCLan, Preston, UK.
82. Marsden J.A. (2002) *Experimental and Numerical Studies of Buoyant Turbulent Rotating Flames*. A transfer report submitted to the University of Central Lancashire in fulfilment for the transfer from MPhil to PhD. UCLan, December 2002.
83. Marsden J.A. (2002) Experimental and Numerical Studies of Whirling Fires in Enclosure. *Research Seminar No 70 of the Centre for Research in Fire and Explosion Studies*, 19 April 2002, UCLan, UK.
84. Marsden J.A. (2002) Experimental and Numerical Studies of Whirling Fires in Enclosure. *2002 Graduate Lecture of Institution of Fire Engineers*, 2 May 2002 Manchester Metropolitan University, UK.
85. Marsden J.A. (2003) Experimental and Numerical Studies of Whirling Flames. *University of Central Lancashire Graduate School*, 3 December 2003, UCLan, Preston, UK.
86. Marsden J.A. (2004) Whirling Fires within Enclosures. *Institution of Fire Engineers International Conference*, 3-6 October 2004, Kuala Lumpur, Malaysia.
87. Marsden J.A., Francis J. (2000) The Creation of Swirling Fire Plumes in Full Scale Compartment Tests. Initial Results, *Research Event 2000 – RE2K*, 6-7 December 2000, The Fire Service College, Moreton-in-Marsh, UK.

References

88. Marsden J.A., Snegirev A. (2001) Fire Whirls within Compartments. *Research Event 2001 – RE01*, 21-22 November 2001, The Fire Service College, Moreton-in-Marsh, UK.
89. Masri A.R., Kalt P.A.M., Barlow R.S. (2004) The Compositional Structure of Swirl-Stabilised Turbulent Non-premixed Flames. *Combustion and Flame*, **137**, 1-2, 1-37.
90. McGrattan K.B., Baum H.R., Rehm R.G. (1998) Large Eddy Simulations of Smoke Movement. *Fire Safety Journal*, **30**, 2, 161-178.
91. Miles S., Kumar S. (2004) Computer Modelling to Assess the Benefits of Road Tunnel Fire Safety Measures. *Proc. of the 10th Int. Conference Interflam2004*, Vol. 1, pp. 821-826.
92. Miles S., Kumar S., Cox G. (1997) The Balcony Spill Plume-Some CFD Simulations. *Proc. of the 5th Int. Symposium on Fire Safety Science*, IAFSS, pp. 237-247.
93. Milosavljevic V.D., Taylor A.M.K.P., Whitelaw J.H. (1990) The Influence of Burner Geometry and Flow Rates on the Stability and Symmetry of Swirl-Stabilized Non-premixed Flames. *Combustion and Flame*, **80**, 2, 196-208.
94. Modest M.F. (1993) *Radiative heat transfer*, McGraw-Hill.
95. Morcos V.H., Abdel-Rahim Y.M. (1999) Parametric Study of Flame Length Characteristics in Straight and Swirl Light-fuel Oil Burners. *Fuel*, **78**, 979-985.
96. Morsi Y.S.M., Holland P.G., Clayton B.R. (1995) Prediction of Turbulent Swirling Flows in Axisymmetric Annuli. *Applied Mathematical Modelling*, **19**, 10, 613-620.
97. Morton B.R. (1970) The Physics of Fire Whirls. *Fire Research. Abstracts and reviews*, **12**, 1, 1-19.
98. Mudan K.S., Croce P.A. (1995) Fire Hazard Calculations for Large Open Hydrocarbon Fires. In: *SFPE Handbook of Fire Protection Engineering*, 2nd Ed., NFPA, pp 3/197 – 3/240.
99. Nakakuki A. (1997) Heat Transfer in Hot-Zone-Forming Pool Fires. *Combustion and Flame*, **109**, 353-369.
100. Nakakuki A. (2002) Heat Transfer in Pool Fires at a Certain Small Lip Height. *Combustion and Flame*, **131**, 259-272.

101. Nikjooy M., Mongia H.C., Samuelsen G.S., McDonell V.G. (1989) A Numerical and Experimental Study of Confined Swirling Jets. *AIAA Paper 89-2898, AIAA 27th Aerospace Meeting, pp. 1-13.*
102. Novozhilov V. (2001) Computational Fluid Dynamics Modelling of Compartment Fires. *Progress in Energy and Combustion Science, 27*, 611-666.
103. Orloff L. (1980) Simplified Radiation Modelling of Pool Fires. *Proceedings of the Combustion Institute, 18*, 549-561.
104. Pitts W.M. (1990) Wind Effects on Fires. *Progress in Energy and Combustion Science, 17*, 83 -134.
105. Planas-Cuchi E., Casal J. (1998) Flame temperature distribution in a pool fire. *Journal of Hazardous Materials, 62*, 3, 231-241.
106. Porterie B., Morvan D., Larini M., Loraud J.C. (1998) Wildfire Propagation: A Two-Dimensional Multiphase Approach. *Combustion Explosion and Shock Waves, 34*, 2, 139-150.
107. Quintiere J.G (1991). Mass fire experiment. *Proc. of the 3rd ASME/JSME Engineering Joint Conference, 50*, 5, 321-330.
108. Quintiere J.G., Rinkinen W.J., Jines W.W. (1981) The Effect of Room Openings on Fire Plume Entrainment. *Combustion Science and Technology, 26*, 193-201.
109. Repp S., Sadiki A., Schneider C., Hinz A., Landefeld T., Janicka J. (2002) Prediction of Swirling Confined Diffusion Flame with a Monte Carlo and Presumed-PDF-model. *International Journal of Heat and Mass Transfer, 45*, 6, 1271-1285.
110. Saffman P.G. (1977) Results of a Two Equation Model for Turbulent Flows and Development of a Relaxation Stress Model for Application to Straining and Rotating Flows. In: *Turbulence in Internal Flows. Turbo-machinery and Other Engineering Applications*. S.N.B. Murthy (ed.) Hemisphere Publ. Corp., Washington, 1977, pp. 191-368.
111. Sanderson V.E., Rubini P.A., Moss J.B. The effect of Vent Size on a Compartment Fire: Numerical Simulation and Validation. *Proceedings of the eighth international conference INTERFLAM'99, Vol. 2*, pp. 1189-1194.
112. Sanson L.Z. (2001) The asymmetric Ekman decay of cyclonic and anticyclonic vortices. *European Journal of Mechanics. B – Fluids, 20*, 541-556.
113. Satoh K. (1996) Numerical Study and Experiments of Fire Whirl. *Proc. of the 7th Int. Conf. Interflam'96*, pp. 393-402.

114. Satoh K., Yang K.T. (1996) Experimental Observations of Swirling Fires. *Proc. of the ASME. Heat Transfer Division*, **335**, 4, 393-400.
115. Satoh K., Yang K.T. (1997) Simulations of Swirling Fires Controlled by Channeled Self-generated Entrainment Flows. *Proc. of the 5th Int. Symp. On Fire Safety Science*, IAFSS, pp. 201-212.
116. Satoh K., Yang K.T. (1998) Experiments and Numerical Simulations of Swirling Fires due to 2x2 Flames in a Channel with Single Corner Gap. *Proc. of the ASME, Heat Transfer Division*, **361**, 2, 49-56.
117. Satoh K., Yang K.T. (1999) Measurements of Fire Whirls from a Single Flame in a Vertical Square Channel with Symmetrical Corner Gaps. *Proc. of the ASME, Heat Transfer Division*, **364**, 4, 167-173.
118. Selle L., Lartigue G., Poinso T., Koch R., Schildmacher K.-U., Krebs W., Prade B., Kaufmann P., Veynante D. (2004) Compressible Large Eddy Simulation of Turbulent Combustion in Complex Geometry on Unstructured Meshes. *Combustion and Flame*, **137**, 4, 489-505.
119. Sloan D.G., Smith P.J., Smoot L.D. (1986) Modeling of Swirl in Turbulent Flow Systems. *Progress in Energy and Combustion Science*, **12**, 1, 163-250.
120. Smith T.F., Al-Turki A.M., Byun K.-H., Kim T.K. (1987) Radiative and Conductive Transfer for a Gas/Soot Mixture Between Diffuse Parallel Plates, *Journal of Thermophysics and Heat Transfer*, **1**, 1, 50-55.
121. Smith T.F., Shen Z.F., Friedman J.N. (1982) Evaluation of Coefficients for the Weighted Sum of Gray Gases Model. *Journal of Heat Transfer - Transactions of the ASME*, **104**, 602-608.
122. Snegirev A.Yu. (2004) Statistical Modelling of Thermal Radiation Transfer in Buoyant Turbulent Diffusion Flames. *Combustion and Flame*, **136**, 1-2, 51-71.
123. Snegirev A.Yu., Makhviladze G.M., Talalov V.A. (2001) Statistical Modelling of Thermal Radiation in Compartment Fire. *Proc. of the 9th Int. Conf. Interflam 2001*, Vol. 2, pp. 1011-1024.
124. Snegirev A.Yu., Makhviladze G.M., Talalov V.A., Chamchine A.V. (2003) Turbulent Diffusion Combustion under Conditions of Limited Ventilation: Flame Projection through an Opening. *Combustion Explosion and Shock Waves*, **39**, 1, 1-10.
125. Snegirev A.Yu., Marsden J.A., Francis J., Makhviladze G.M. (2003) Numerical Studies and Experimental Observations of Whirling Flames. *4th International*

- Seminar on Fire and Explosion Hazards*, 8-12 September 2003, Ulster, UK, pp. 675 – 690.
126. Snegirev A.Yu., Marsden J.A., Francis J., Makhviladze G.M. (2004) Numerical Studies and Experimental Observations of Whirling Flames. *International Journal of Heat and Mass Transfer*, **17**, 12–13, 2523–2359.
127. Snegirev A.Yu., Marsden J.A., Makhviladze G.M. (2003) Whirling Flames. *Meeting of Consortium on Computational Combustion for Engineering Applications COCCFEA*, 19 September 2003, UMIST, Manchester, UK.
128. Snegirev A.Yu., Marsden J.A., Makhviladze G.M. (2004) Radiative Impact of Wind-Blown Fires. *Proc. of the 10th Int. Conference Interflam2004*, Vol. 1, pp. 289-300.
129. Snegirev A.Yu., Marsden J.A., Makhviladze G.M. (2005) Transient Behaviour and Stability of Whirling Flames in Enclosure. *Proceedings of the Combustion Institute*, **30** (to appear).
130. Soma S., Saito K. (1991) Reconstruction of Fire Whirls Using Scale Models. *Combustion and Flame*, **86**, 3, 269-284.
131. Souil J.M., Joulain P., Gengembre E. (1984) Experimental and Theoretical Study of Thermal Radiation from Turbulent Diffusion Flames to Vertical Target Surfaces. *Combustion Science and Technology*, **41**, 69-81.
132. Srinivasan R., Mongia H.C. (1980) Numerical Computation of Swirling Recirculating Flow. *Final Report NASA CR-165196*.
133. Steckler K.D., Quintiere J.G., Rinkinen W.J. (1982) Flow Induced by Fire in a Compartment. *Report NBSIR 82-2520*. National Bureau of Standards. Department of Commerce. Washington DC 20234, 93 P.
134. Sturgess G.J., Syed S.A. (1990) Calculation of Confined Swirling Flows. *International Journal of Turbo and Jet Engines*, **7**, 103-121.
135. Thomas P.H., Hinkley P., Theobald C., Simms D. (1963) Investigation into the Flow of Gases in Roof Venting. *Technical Paper*, No 7, HMSO, London.
136. Underwood D.S., Waitz I.A., Greitzer E.M. (2000) Confined Swirling Flows with Heat Release and Mixing. *Journal of Propulsion and Power*, **16**, 2, 169-177.
137. Viskanta R., Menguc M.P. (1987) Radiation Heat Transfer in Combustion Systems. *Progress in Energy and Combustion Science*, **13**, 97-160.

138. Wall K.M., Taulbee D.B. (1996) Application of a Nonlinear Stress-strain Model to Axisymmetric Turbulent Swirling Flows, *International Journal of Heat and Fluid Flow*, **17**, 2, 116-123.
139. Wang Z., Jia F., Galea E.R., Patel M.K., Ewer J. (2001) Simulating one of the CIB W14 Round Robin Test Cases using the SMARTFIRE Fire Field Model. *Fire Safety Journal*, **36**, 7, 661-677.
140. Weber R., Dugue J. (1992) Combustion Accelerated Swirling Flows in High Confinements. *Progress in Energy and Combustion Science*, 1992, **18**, 4, 349-367.
141. Weber R., Visser B.M., Boysan F. (1990) Assessment of Turbulence Modelling for Engineering Prediction of Swirling Vortices in the near Burner Zone. *International Journal of Heat and Fluid Flow*, **11**, 3, 225-235.
142. Wegner B., Maltsev A., Schneider C., Sadiki A., Dreizler A., Janicka J. (2004) Assessment of Unsteady RANS in Predicting Swirl Flow Instability Based on LES and Experiments. *International Journal of Heat and Fluid Flow*, 2004, **25**, 3, 528-536.
143. Wilcox D.C. (1998) *Turbulence Modelling for CFD*. DCW Industries.
144. Xia J.L., Yadigaroglu G., Liu Y.S., Schmidli J., Smith B.L. (1998) Numerical and Experimental Study of Swirling Flow in a Model Combustor. *International Journal of Heat and Mass Transfer*, **41**, 11, 1485-1497.
145. Xin Y., Gore J., McGrattan K.B., Rehm R.G., Baum H.R. (2002) Large Eddy Simulation of Buoyant Turbulent Pool Fires. *Proceedings of the Combustion Institute*, **29**, 259-266.
146. Yau T.M. (2001) Effect of Lining Thermal Inertia on Small-scale Compartment Fire. *PhD Thesis University of Central Lancashire. Preston. UK*
147. Yuan S.P., So R.M.C. (1998) Turbulent Rotating Flow Calculations: an Assessment of Two-equation Anisotropic and Reynolds Stress Models. *Proceedings of the Institution of Mechanical Engineers - Part G, Journal of Aerospace Engineering* **212**, 193-212.
148. Zaichik L.I. (1997) Wall Functions for Simulation of Turbulent Flows and Heat Transfer. *High Temperature*, **35**, 3, 385-390.
149. Zhang D., Hill P.G. (1996) Effect of Swirl on Combustion in a Short Cylindrical Chamber. *Combustion and Flame*, **106**, 3, 318-332.

References

150. Zhang J., Jia F., Galea E.R., Ewer J. (2004) A New Approach to the Simulation of Gaseous Combustion and its Application to Several Test Fire Scenarios. *Proc. of the 10th Int. Conference Interflam2004*, Vol. 2, pp. 1293-1304.
151. Zhou L.X., Wang F., Zhang J. (2003) Simulation of Swirling Combustion and NOX Formation using a USM Turbulence-chemistry Model. *Fuel*, **82**, 13, 1579-1586.
152. Zukoski E.E. (1995) Properties of Fire Plumes. In. *Combustion Fundamentals of Fire*, G. Cox (Ed.), Academic Press, pp 101-219.